STRUCTURE PROPERTY RELATIONS IN A RANGE OF MESOPHASE PITCH-BASED CARBON FIBRES

A thesis submitted in accordance with the requirements
for the degree of
Doctor of Philosophy

by
HONG GUO
under the supervision of
Prof. D.J. Johnson and Dr. M.G. Dobb

The candidate confirms that the work submitted is her own and that appropriate credit has been given where reference has been made to the work of others.

Department of Textile Industries
The University of Leeds
Leeds LS2 9JT

October 1994

To My Husband and My Son

Abstract

The purpose of this work was to study the structure and compressive behaviour of mesophase pitch (MP) -based carbon fibres, in an attempt to understand the relations between fibre structure and compressive strength. For this purpose, a range of Du Pont MP-based carbon fibres were used, including high modulus fibres (E35, E55, E75, E105, E120 and E130) and high thermal conductivity fibres (E35C, C700).

Compressive strengths of the fibres were measured using a tensile recoil testing method, and a failure mechanism was proposed on the basis of recoil-failure face observations with the scanning electron microscope. It was considered that Du Pont fibres fail due to a combination of tensile and compressive forces arising from bending.

Both macrostructure and microstructure of the fibres were investigated using X-ray diffraction, scanning and transmission electron microscopy. The macrostructure is of folded pseudo-radial layers arranged in domains which become more perfect and singular with increasing Young's modulus. Moreover, high thermal conductivity fibres have both circular and missing-sector cross sections. The microstructure ranges from turbostratic to three-dimensional graphitic order with different degrees of imperfection as observed directly in dark-field and lattice-fringe micrographs.

For the first time, image analysis techniques were applied to TEM micrographs (mainly dark-field and lattice-fringe images) in an attempt to determine quantitatively the degree of lattice imperfection as well as other structural parameters. Following the analysis of images, new parameters to measure lattice imperfection have been introduced, particularly the crystallite imperfection factor (I_c) and lattice tortuosity (S).

The influence of both macrostructure and microstructure on the fibre compressive strength has been discussed thoroughly. It was found that increases in the lattice imperfections (both in-plane imperfection and stacking imperfection) increase the fibre compressive strength significantly. In addition, the layer stacking size and crystallite orientation should be limited to a relatively lower level in order to achieve a good compressive performance of carbon fibres. With regards to the effect of macrostructure, generally fibres with folded layers and domain structures tend to have a higher compressive strength than fibres with flat layers and uniform structure.

Acknowledgments

I would like to express my sincere gratitude to Prof. D.J. Johnson and Dr. M.G. Dobb for their advice and encouragement throughout the course of this investigation.

I would like to present my thanks to Dr. R.M. Robson for her helpful suggestions, discussions and guidance in TEM operation.

My thanks are also due to Miss H.M. Dyson for her technical help, to Dr. A. Voice and Dr. I. Karacan for their help with X-ray experiments, and to many other colleagues and friends within the department and elsewhere for their kind help during this work.

I am very grateful to the British Council and the Ministry of Education of the People's Republic of China for the award of a Sino-British Friendship Scholarship Scheme providing the financial support.

I am deeply indebted to my parents for their continuous and enormous moral support, especially for looking after my son, and also to my sister, brother, and brother-in-law for their emotional support. In particular, I am indebted to my husband, Tian-Yi Liao, and our lovely son, Wang Liao, for their understanding, sacrifice and constant encouragement.

Contents

Chapter 1 Introduction

Chapter 2 Experimental Aspects

Chapter 3 Structure of MP-based Carbon Fibres

Chapter 4 Image Analysis of the Microstructure in Carbon Fibres

Chapter 5 Compressive Properties of MP-based Carbon Fibres

Chapter 6 The Relations between Structure and Compressive Strength

List of Figures

List of Tables

Identification of Micrographs

Figure 3-1.	SEM.	(E35) 1739 (E55) 1737 (E75) 1768 (E105) 1783 (E120) 1904 (E130) 1813 (E35C) 1708 1709 (C700) 1849 1883
Figure 3-5.	TEM	(E35C) 16468 (E35) 16419 (E55) 16455 (E75) 16445 (E105) 16304 (E120) 16435 (E130) 16293 (C700) 16355
Figure 3-6.	TEM	16389
Figure 3-7.	TEM	16254
Figure 3-8.	TEM	15892
Figure 3-9.	TEM	16172
Figure 3-10.	TEM	16084
Figure 3-11.	TEM	16142
Figure 3-12.	TEM	16125
Figure 3-13.	TEM	16371
Figure 3-14.	TEM	(E35C) 16529 (E35) 16527 (E55) 15940 (E75) 15952 (E105) 16102 (E120) 16029 (E130) 16123 (C700) 16358
Figure 5-4.	SEM	(a) 2296 (b) 2258 (c) 2267
Figure 5-5.	SEM	2284

Chapter 1

Introduction

1. 1. General introduction

Carbon fibres consist of at least 92 *wt%* of carbon and usually have diameters smaller than 10 μm. Due to their superior stiffness (high Young's modulus), high tensile strength, good electrical and thermal conductivity and low density, carbon fibres have been extensively used in the fabrication of so called 'advanced or high performance' composites which are widely used in the aerospace industry and sports equipment.

Carbon fibres were first prepared from viscose rayon by Union Carbide in 1960 [1], from polyacrylonitrile (PAN) in Japan in 1961 [2] and from isotropic pitch also in Japan in 1964 [3]. However, all of these procedures included an expensive and difficult high-temperature stretching process. The mechanical performance of these fibres were very modest.

Later, Watt and Johnson developed a process at the Royal Aircraft Establishment (RAE) in Farnborough, in which PAN fibres were converted into carbon fibres with much improved modulus and strength. The need to keep the PAN fibres under controlled tension during oxidation was one of the most important developments during this work, and eventually led to the RAE British patent for producing high modulus carbon fibres. In 1966, the RAE process was applied in fully commercial production lines at Morganite Ltd. and Courtaulds Ltd. [4,5].

The original pitch-based carbon fibres were produced from isotropic pitch and had very low modulus and strength [3]. However in 1970 Singer [6] discovered the mesophase during pyrolysis of pitches. In such a mesophase the polyaromatic layers are regularly arranged possessing the same coalescence behavior as nematic liquid crystals having rod-like molecules. The preferred orientation of the mesophase promotes production of carbon fibres having very high-modulus. Japanese workers [7] also produced well-oriented mesophase pitch (MP)-based carbon fibres. Since then, many different types of MP-based carbon fibres have been developed.

1. 2. Types of carbon fibres

The combination of various fibre properties, including mechanical, physical and chemical properties, depends strongly on the precursor material, therefore, usually carbon fibres are grouped into three major categories on the basis of the precursor, namely, (1) PAN-based, (2) pitch-based and (3) rayon-based fibres. As mentioned previously, PAN-based fibres are obtained from polyacrylonitrile precursor fibres and have been commercially available for over 20 years. Pitch-based fibres are generally derived from petroleum or coal-tar pitch and can be subdivided again into isotropic pitch-based and mesophase pitch-based fibres depending on whether or not the raw pitch is pyrolyzed into the mesophase. Rayon-based carbon fibres were produced from rayon precursor fibres by chemical pre-treatment and carbonization. However their mechanical properties were relatively poor and are no longer in production.

Carbon fibres can also be classified into three groups according to their mechanical properties, i.e. (1) High Modulus (HM), (2) High Strength (HT or HS), and (3) Intermediate Modulus (IM) fibres. HM fibres, also referred to as type I fibres, can be produced after heat-treatment upto $2500^0\ C$ and exhibit a Young's modulus greater than 300 GPa, but with a relatively low tensile strength (less than 3 GPa). HT fibres, also known as type II fibres, are prepared by carbonizing PAN fibres at $1000\text{-}1500^0\ C$, and have a high tensile strength above 3 GPa, but a relatively low modulus. IM fibres have a comparable value of tensile strength to HT fibres but are characterized by an improved Young's modulus.

Comparison of fibre types

The great advantage of PAN-based carbon fibres is that they are capable of developing very high tensile strength and indeed, over the last decade, a dramatic improvement in tensile strength has been achieved (from approximately 3.4 *GPa* to 6.9 *GPa*) [8]. Tensile moduli ranging from 207 *GPa* to 586 *GPa* and elongations from less than 1% to over 2% are also commercially available. Generally PAN-based fibres have a relatively higher compressive strength than pitch-based fibres. Such a balance of mechanical properties together with their good handleability, has led to PAN-based carbon fibres accounting for approximately 90% of the world wide total production of carbon fibres.

Mesophase pitch-based fibres tend to posses very high Young's modulus (reaching 900 *GPa*) and excellent electrical and thermal conductivities due to the very high molecular orientation inherent in the mesophase pitch which is reflected in the final carbon fibre. Both these properties are very critical for aerospace structural applications and MP-based fibres are being widely evaluated in these areas. However, MP-based fibres tend to have lower tensile and compressive strengths compared with PAN-based fibres, which currently limits applications. Therefore, studies aimed at understanding the relationship between microstructure and both tensile and compressive strengths, are of considerable importance.

1. 3. Production of carbon fibres

1. 3. 1. Production of PAN-based fibres

The production of carbon fibres from PAN precursor is well documented in the literature [9,10]. A typical flow diagram for the process is shown in Figure 1-1.

Spinning of PAN precursor fibres

Details of producing suitable precursor PAN fibres for carbon fibre production have been reported [9,10,11].

Stabilization of PAN precursor fibres

The molecular orientation produced as the PAN precursor is stretched must be stabilized if the mechanical properties of the carbon fibre are to be achieved. Thus the precursor fibres are heated in an oxygen-containing atmosphere at $150^0\ C$ to $300^0\ C$ while they are held under tension. This heat treatment converts the nitrile groups into closed ring structures and helps the chain to form cross-link structures so as to withstand the high temperature present in subsequent processing.

Carbonization and graphitization

Stabilized PAN fibres are then carbonized and sometimes graphitized by slowly heating them to temperatures in excess of $1000^0\ C$. Carbonization involves heat treating precursor fibres at temperatures between $1000^0\ C$ and $1700^0\ C$, whereas graphitization

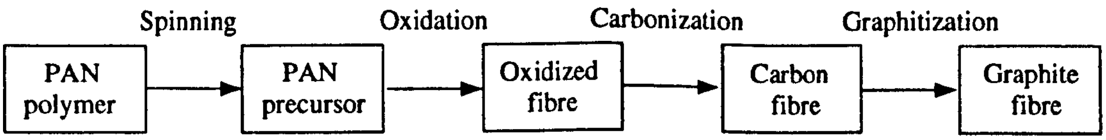

Figure 1-1. Schematic diagram of the processing steps in the preparation of PAN-based carbon fibres

refers to heat treatments carried out at temperatures ranging from 1700^0 C up to 3000^0 C (to improve the perfection and orientation of the crystallites). After the final heat treatment, almost all non-carbon impurities are lost and well-defined hexagonal networks develop.

1. 3. 2. Production of MP-based fibres

The most commonly used pitches for the manufacture of carbon fibres are those obtained from petroleum asphalt, coal tar, and PVC [12]. The composition and nature of the pitch were described by Rand [13] and Edie [14]. Essentially, pitch is the residue after removing the heavy oil or anthracene oil (boiling at 250^0 C~400^0 C) from many bituminous materials using destructive distillation.

Only the manufacturing of mesophase pitch-based carbon fibres will be considered here and the process for producing the isotropic pitch-based carbon fibres can be found elsewhere [13,14].

The fundamental requirements for the manufacture of carbon fibres from mesophase pitch have been well elucidated by Rand [13]. Generally three basic stages are involved in the processing, namely, (1) preparation of the mesophase pitch, (2) spinning of the mesophase pitch into precursor fibres, and (3) conversion of precursor fibres into carbon fibres (including both oxidation and carbonization).

Preparation of the mesophase pitch

Mesophase pitch can be prepared by the thermal or catalytic polymerization of a suitable petroleum or coal-tar pitch at temperatures between 350^0 $C$and 500^0 C until the isotropic material is transformed into the mesophase [15].

An alternative process to prepare the mesophase pitch is referred to as the solvent extraction method [16]. In this process, solvents such as benzene, heptane, and toluene are used to extract, first, a portion of the isotropic pitch. The solvent insoluble portion can be transformed immediately to mesophase pitch by heating above the glass transition temperatures (230~400^0 *C*) in less than 10 minutes. It is claimed that these mesophase pitches, composed of stacked aromatic hydrocarbon molecules, are stable to relatively high temperatures, and this enables the subsequent spinning process to be carried out without fear of decomposition of the material.

Spinning of mesophase pitch

The resulting mesophase pitch material is then spun to form precursor fibres by various modes such as melt spinning, centrifugal spinning, blow spinning or jet spinning [15]. However, melt spinning is the preferred process to obtain the continuous mesophase precursor fibres [17]. Details of the melt-spinning process have been reported by several workers [18,19].

Conversion of precursor fibres into carbon fibres

Oxidation After spinning, the precursor fibres are oxidized in a manner similar to that used in the PAN process. The as-spun mesophase fibre already possesses a high degree of crystallite orientation, therefore unlike the PAN process, applying tension during the oxidation stage is not necessary.

Carbonization and graphitization The oxidized fibres are subsequently either carbonized or graphitized in an inert atmosphere at the desired temperature to develop their final structure and properties. When mesophase fibres are carbonized the principal gases that evolve are methane and hydrogen, and most of these gases are evolved in the early stages (below 1000^0 C). Thus, normally the oxidized fibres are pre-carbonized at 900~1000^0 C for a few minutes to avoid excessive disruption of the structure or creation of flaws that would occur if the fibres were rapidly heated to the final carbonization temperature [14].

Final carbonization of the fibres is required to remove the remaining heteroatoms in the precarbonized fibres and to develop the layer structure. The crystallite size and perfection as well as the orientation of layer planes can be increased by increasing the temperature. However, the general macrostructure of the precursor fibres is retained in the carbonized form although sometimes a "missing-sector" structure is formed [20].

Graphitization is a further process which dramatically improves tensile modulus and both thermal and electrical conductivity. Studies indicated that after graphitization MP-based carbon fibres exhibit the three dimensional order of graphite [13].

1. 4. Structure of carbon fibres

1. 4. 1. General molecular structure

1. 4. 1. 1. Structure of perfect graphite

As shown in Figure 1-2, a single crystal of graphite has a layered structure. In the layers, each carbon atom is surrounded by three others in a planar trigonal arrangement so that the atoms and bonds form a hexagonal pattern. The lattice constant a_0 is 0.2462 *nm* so that the in-plane bond length is 0.142 *nm* [21]. Usually the graphite layers are stacked in an *ABAB*...... sequence and oriented with parallel to each other. The attraction between the layers is due to weak *Van der Waal* forces and the distance between the layers, referred to as the interlayer spacing d_{002}, has been reported as 0.3354 *nm* at room temperature [21].

Apart from *ABAB*...... sequence, an alternative stacking sequence *ABCABC*...... can also occur for carbon, resulting in a rhombohedral unit cell. However, the rhombohedral form of graphite always occurs together with the hexagonal one [22].

1. 4. 1. 2. Structure of turbostratic carbon

The graphite layer planes in Figure 1-2 may also be rotated individually about the c-axis to form a quasi-crystal in which the layer planes are not ordered with respect to each other. This structure is referred to as turbostratic carbon. On a larger scale, carbon can take any number of quasi-crystalline forms ranging continuously from a highly ordered 3D-graphite (Figure 1-3a) to two-dimensional turbostratic carbon (Figure 1-3b). These forms may be characterized by the magnitude of the interlayer spacing d_{002} (ranging from 0.3354 *nm* for perfect graphite to more than 0.3440 *nm* for turbostratic layering).

1. 4. 2. Structure of PAN-based carbon fibres

1. 4. 2. 1. Ruland's model

__Ribbon-like model__

A ribbon-like model for PAN-based carbon fibres, as indicated in Figure 1-4, was proposed by Ruland and his co-workers from X-ray and electron microscopy studies [24,25,26,27,28]. According to this model, the basic structural unit consists of ribbon-like layer planes packed side by side enclosing needle-shaped voids. A number of

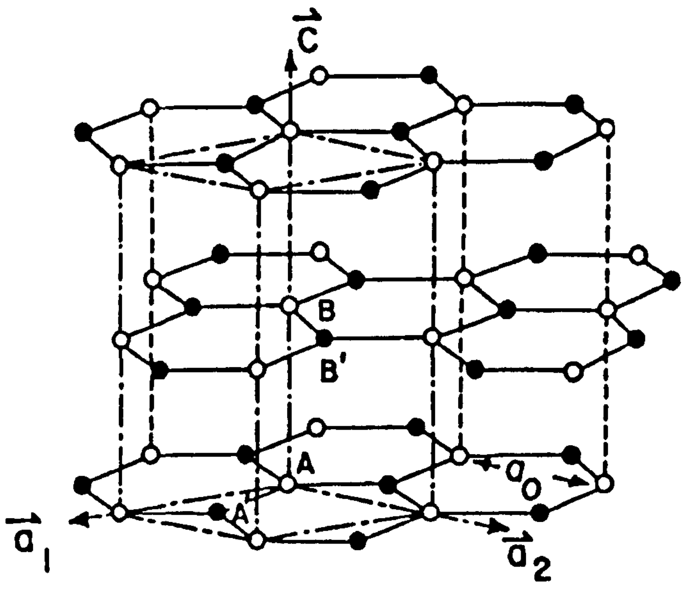

Figure 1-2. The structure of a single crystal of graphite, in which planes of carbon hexagons are stacked in an *ABAB......* sequence [21].

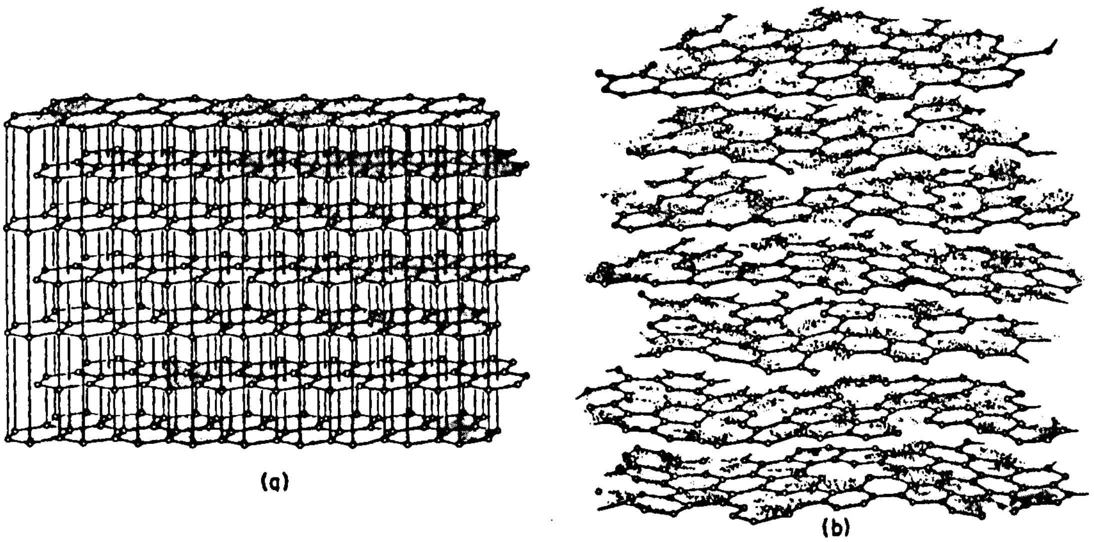
(a)

(b)

Figure 1-3. Schematic diagram comparing (a) a three-dimensional graphite lattice with (b) a turbostratic structure [23].

ribbons group together to form a wrinkled micro fibril with a high degree of preferred orientation parallel to the fibre axis. In addition, the ribbons pass smoothly from one turbostratic domain of stacking to another, resulting in a turbostratic disorder.

1. 4. 2. 2. Johnson's models

(A) Block model

Johnson and Tyson [29] initially proposed a block model for the PAN-based carbon fibre structure. They suggested that the structure was formed from arrays of cube-like crystallites which are stacked approximately end to end in a columnar form and arranged parallel to the fibre axis. The crystallites are separated by twist boundaries and sharp-edged voids, as shown in Figure 1-5. The model needed further modification in order to indicate other factors such as the linking between the crystallites.

(B) Interlinking model

Later after electron microscopy observations on both fragments and longitudinal sections of carbon fibres, Johnson and Crawford [30,31] presented a more detailed model of the structure for a type I PAN-based carbon fibre. This model contained sharp-edged voids, tilt and twist boundaries and interlinked (or overlapped) crystallite to account for the Moirè Patterns seen in TEM images. The two-dimensional and three-dimensional representations of this interlinked model are shown in Figures 1-6 and 1-7 respectively.

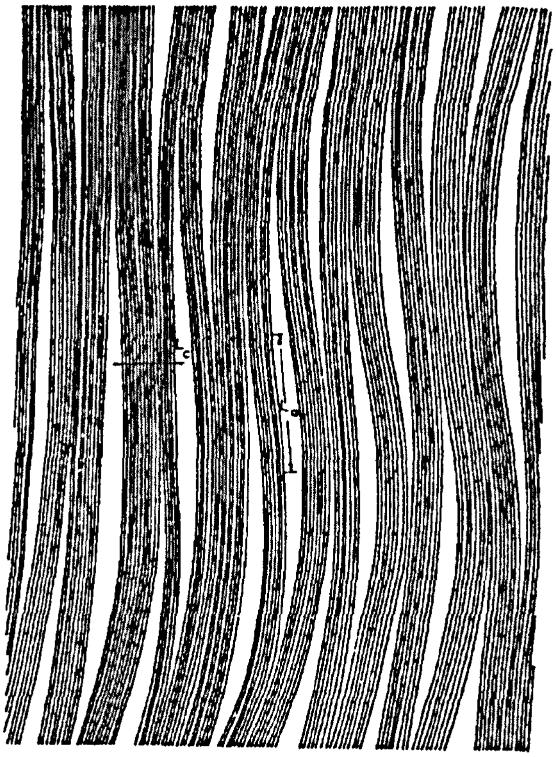

Figure 1-4. Ribbon-like model of carbon fibre structure from Ruland *et al.* [24]

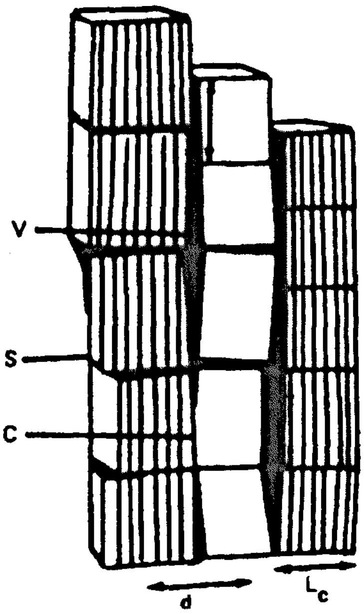

Figure 1-5. Block model of carbon fibre structure from Johnson *et al.* [29].

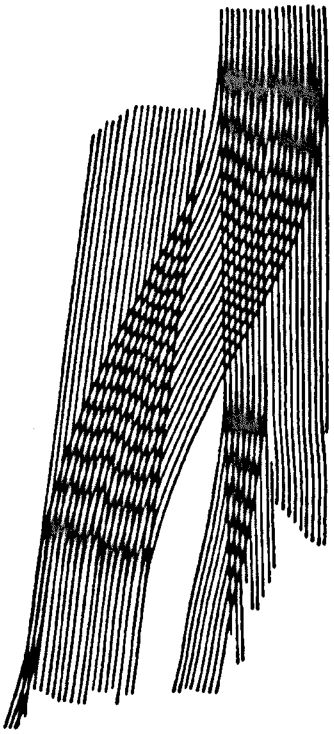

Figure 1-6. Two-dimensional representation of the interlinked model for carbon fibre structure from Johnson *et al.* [30].

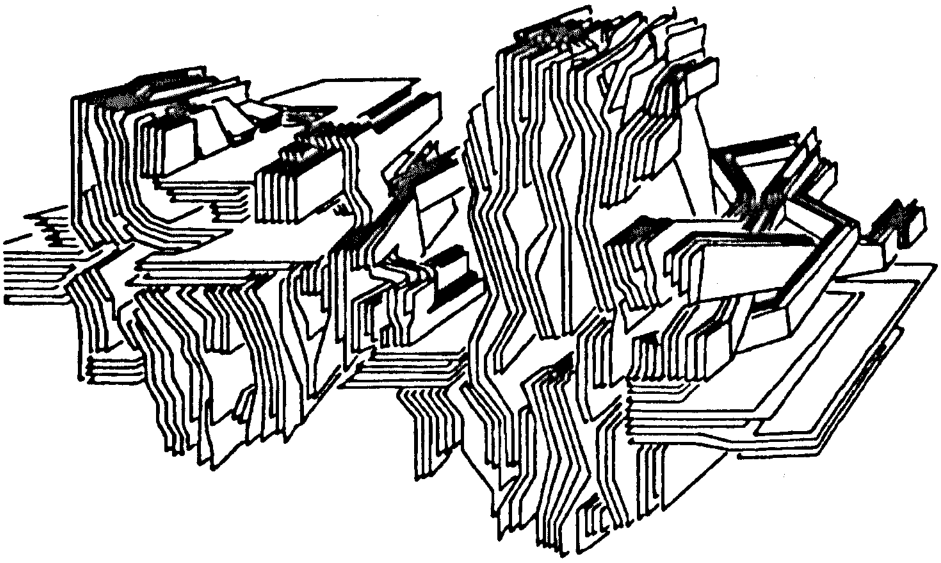

Figure 1-7. Three-dimensional representation of the interlinked model for carbon fibre structure from Johnson *et al.* [31].

(C) Three-dimensional skin-core model

By continuing his investigation on the structure of type I PAN-based carbon fibres, Johnson and his co-worker [32] found that some fibres exhibited skin-core heterogeneity. Both dark-field and lattice-fringe images as well as electron diffraction patterns of longitudinal sections showed that the skin had larger and better oriented crystallites than the core. Further studies of transverse sections revealed that in the skin region (less than 0.5 μm thick), the layer planes are essentially parallel to the surface although interlinking between crystallites and folding of layer planes through angles up to 180^0 (in a "hair pin" fashion) have been observed. In the core region, the layer plane are predominately folded. Based on these observations, Johnson *et al.* proposed a three-dimensional skin-core model of the structure as shown in Figure 1-8.

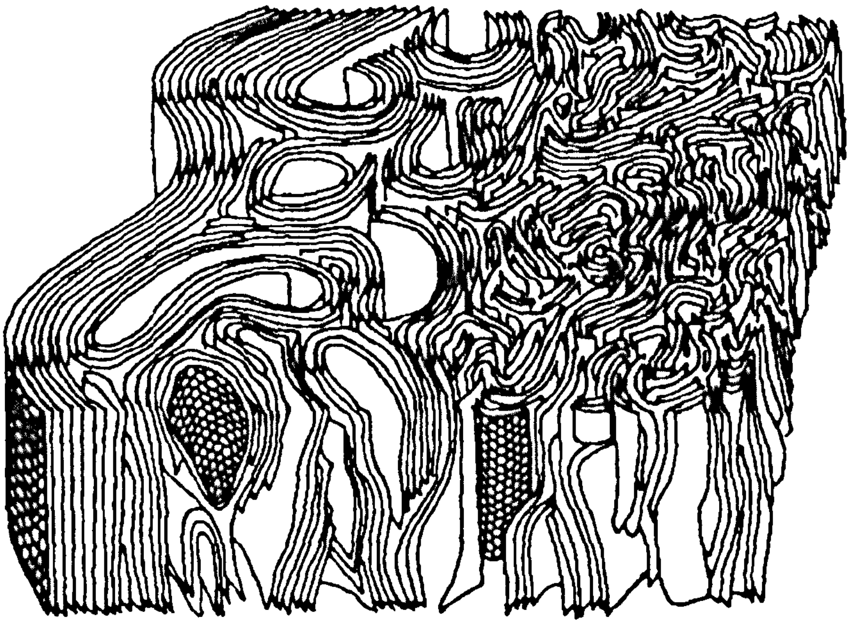

Figure 1-8. Three-dimensional skin-core model of carbon fibre structure from Johnson *et al.* [32].

1. 4. 2. 3. Oberlin's models

Oberlin *et al.*, on the basis of detailed dark-field and high-resolution TEM studies of carbon fibres, have developed two models for the microstructure of PAN-based carbon fibre; one for type I fibres (Figure 1-9a) and another for type II fibres (Figure 1-9b) [33,34].

In the model for type I fibres, the layer planes are entangled and crumpled along the fibre axis, resulting in irregular pores elongated parallel to the fibre axis. Transversely the layer planes show a variable radius of curvature that decreases continuously from the surface to the centre, thus forming an apparent skin-core effect. Furthermore it was proposed that the tensile strength of type I fibres is a function of the radius of curvature of the layer planes. The model for type II fibres essentially shows a similar structural texture to the model for type I fibres, however, the layer planes are much more wrinkled and possess very short range order.

1. 4. 3. Structure of MP-based carbon fibres

1. 4. 3. 1. Microstructure studies

It is generally accepted that MP-based carbon fibres contain layer planes stacked predominantly parallel to the fibre axis and form well developed "sheets" with a graphitic structure [13,36]. Oberlin *et al.* [37], after observing sections of Union Carbide MP-based carbon fibres in the TEM, distinguished three phases namely: polycrystalline graphite, a microporous phase and a major turbostratic phase similar to that found in PAN-based high-modulus fibres (layers smoothly curved and entangled parallel to the fibre axis). They reported that the three phases are distributed at random

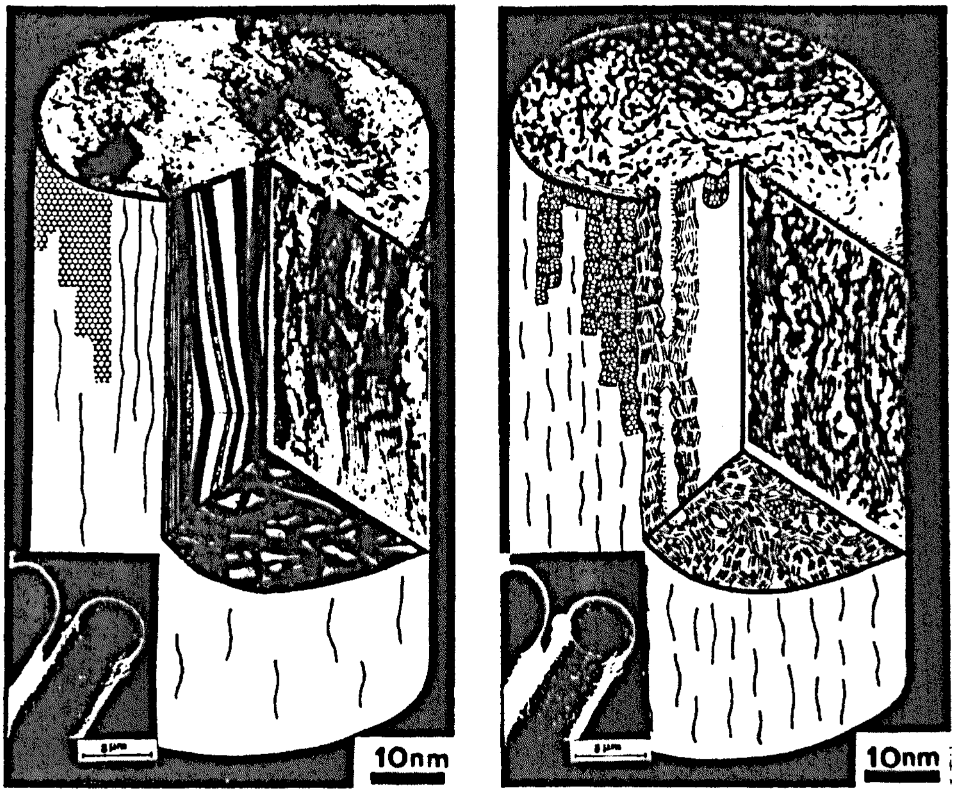

(a) (b)

Figure 1-9. (a) A model of type I PAN-based fibre and (b) a model of type II PAN-based carbon fibre [35].

either parallel or perpendicular to the fibre axis. It was proposed that the Young's modulus increases with either increasing the percentage of the graphite phase or decreasing the percentage of the microporous phase and the degree of layer curvature.

From electron microscopy studies of ultrafine (0.3 μm) MP-based carbon fibres which did not require sectioning, Roche *et al.* [38,39,40] proposed a mosaic arrangement of graphitic sheets. The model is shown in Figure 1-10, where parameter L_{cg} represents the thickness of the graphite grain which consists of a few atomic layers only.

Endo [36] investigated the microstructure of some commercially available MP-based carbon fibres (Amoco and Kashima) by SEM, TEM and X-ray diffraction, and proposed the structural model as shown in Figure 1-11. It was considered that an oriented core structure (Figure 1-11a), associated with relatively flat and highly oriented layer planes, tends to develop into a three-dimensional graphitic structure giving rise to an ultra-high modulus fibre; while a folded layer structure (Figure 1-11b), composed of sheets tightly folded parallel to the fibre axis, may restrict the graphitization and form turbostratic layer structures even after the high-temperature process. He suggested that the high degree of folding of the sheets will give high values for fibre strength and elongation because the folded layer planes tend to increase the resistance of crack propagation.

Bourrat *et al.* reported that folding of the sheets is observed to be associated with disclinations [41]. The density of disclinations was therefore considered to have an effect on determining the final fibre properties. It was believed that a low density of disclinations will give a high radius of curvature (planar sheets) and promote graphitization.

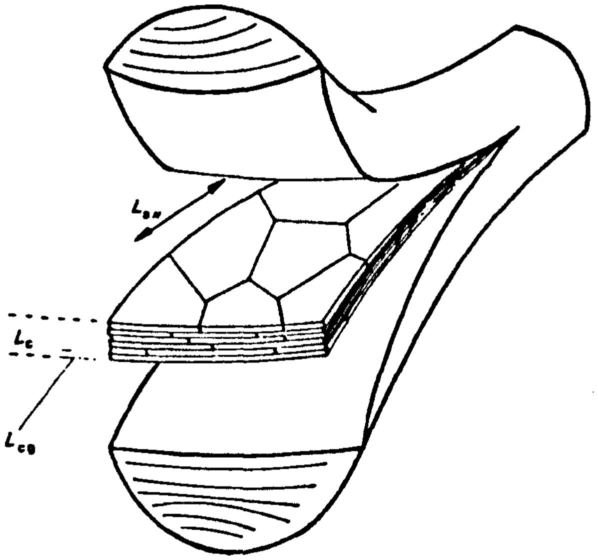

Figure 1-10. Schematic diagram showing the sheet structure in MP-based graphite whiskers L_c=30-100 *nm*, L_{cg}=1-2 *nm*, $L_{a//}$=500-200 *nm* [40].

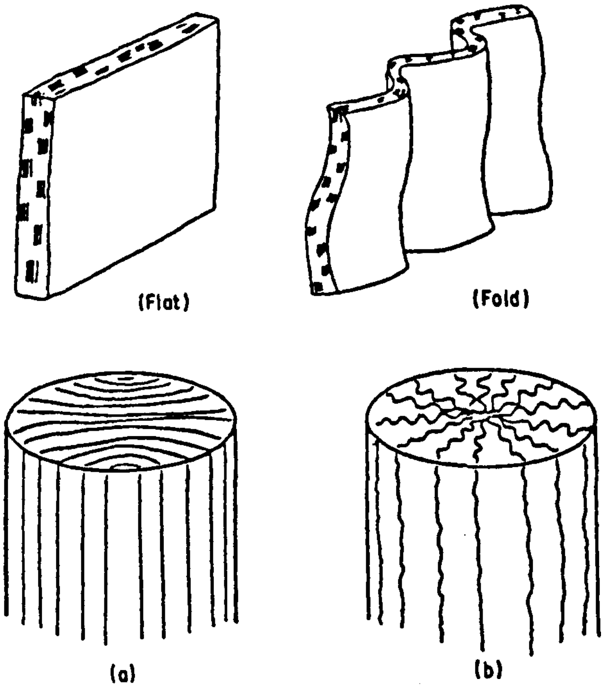

Figure 1-11. Structure models of MP-based carbon fibre: (a) oriented core structure, and (b) folded layer structure [36].

Later, it was claimed [42] that there were three levels of structural organization in MP-based carbon fibres. At the molecular level, the pitch molecules are stacked together creating small coherent domains. At the intermediate level, molecular assemblies of several microns length with long range orientational order parallel to the fibre axis form microdomains. These domains are limited laterally by wedge disclination to a few hundred nanometers. The highest level of organization defines the fibre texture, which is reflected by variations in long range molecular orientation.

Very recently, Pennock *et al.* [43,44] investigated the structure of a number of commercially available MP-based carbon fibres by using light and electron microscopy. They considered that in Amoco MP-based carbon fibres domains are present which are up to 100 μm long but much thinner laterally (ribbon-like structural units) arranged parallel to the fibre axis. Unlike Oberlin's three phase structure, only two types of distinct domains were found in their works, i. e, dense domain and microporous domain. Dense domains consist of densely stacked graphitic layer planes oriented parallel to the fibre axis, whereas microporous domains contain voids with thin walls of graphitic sheets with no preferred orientation. Domain boundaries were formed either between dense and microporous domains or between adjacent dense domains whereever the orientation changes discontinuously. They finally claimed that the proportion of each domain and their distribution influence the mechanical properties [43].

Following this study, Pennock *et al.* [44] investigated a series of commercial Du Pont fibres and concluded that these fibres were spun from mesophase pitch containing an isotropic phase and that the microporous phase and domain found in Amoco fibres do not exist in these fibres. Moreover, continuously folded layer structures containing a high density of disclinations were also found, which is consistent with Endo's suggestions [36] and Bourrat's observations [41], i. e. a high density of disclinations will result in a high degree of layer folding and thus help to improve fibre strength and elongation.

1. 4. 3. 2. Macrostructure studies

The macrostructure of carbon fibres derived from mesophase pitch have been studied extensively by optical and scanning electron microscopy. Various transverse structures have been observed in mesophase pitch-based fibres as shown in Figure 1-12 [14].

Singer [45] first observed that the transverse structure, in as-spun fibres from Union Carbide, is characterized by either onion-skin, radial or random textures, and that these structure are essentially retained through carbonization or graphitization. It was reported that these arrangements depend upon the spinning conditions, such as melt temperature and viscosity. Hamada *et al.* [18] found that extrusion without stirring tends to give a radial texture and with stirring either random or onion type forms

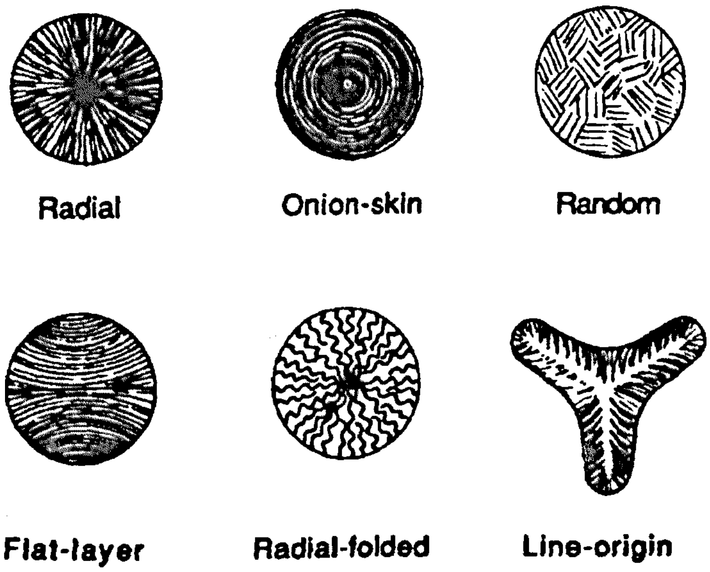

Figure 1-12. Morphology of mesophase pitch-based carbon fibres [14].

depending on the nozzle shape, stirring conditions and viscosity of the pitch. On the other hand, however, Matsumoto [46] controlled the transverse texture of MP-based carbon fibres by changing the dimension of the spinneret, i. e. the length/diameter ratio.

Apart from the three classical types discussed above, other transverse structures have been observed in MP-based carbon fibres. For example it was reported that newer varieties of Amoco high modulus MP-based fibres exhibit a flat-layer texture [14], whilst the Kashima fibre appears to consist of radially-folded layers [36]. In addition, White *et al.* [20] observed that shrinkage during graphitization leads to oval-shaped cross sections in oriented-core fibre; and in some cases missing sector structures might develop from radial cracks in the as-spun fibre [13,20].

Recently, great efforts have been made to modify the flow profile during extrusion so as to create new transverse structures that are less flaw-sensitive and thus exhibit high tensile strengths or improved compressive strength. Edie *et al.* [47] spun two types of carbon fibre with non-circular cross-sections namely: trilobal and octalobal shapes, from petroleum pitch through non-circular spinning nozzles. Surprisingly they found that such fibres possessing line-origin structures have both higher strengths and moduli than those fibres with a circular cross section. However, Mochida *et al.* [48], by spinning the mesophase pitch through non-circular spinning nozzles, have obtained fibres with a circular cross-section having a random or a random-onion texture. Such carbon fibres exhibited greater elongation and tensile strength than fibres with radial texture spun from the same pitch.

Mochida *et al.* [49] also claimed that fibres only moderately stabilized and then carbonized under strain tend to exhibit a skin-core structure. It was found that such fibres exhibited higher orientation, higher modulus and better graphitizability than fully stabilized fibres.

These studies of macrostructure in MP-based carbon fibres indicated that modifying the transverse structure and cross sectional shape may improve the mechanical properties such as tensile modulus, tensile strength and compressive strength.

1. 5. Mechanical Properties of carbon fibres

1. 5. 1. Tensile properties of carbon fibres

1. 5. 1. 1. Tensile modulus

The theoretical tensile modulus of perfectly aligned graphite fibres has been calculated to be about 1000 *GPa*, which has nearly been achieved practically in the case of carbon whiskers [50]. In principle, the tensile modulus is governed by the preferred orientation of the graphitic crystallites relative to the fibre axis. Fourdeux and co-workers [24] measured the orientation parameter q of a number of rayon-, PAN-, and pitch-based carbon fibres, and found that the tensile modulus is indeed a function of orientation, i. e. the more highly oriented the layer planes, the higher the tensile modulus. Therefore, tensile modulus can be increased by enhancing the preferred orientation during the carbon fibre processing. For PAN-based fibres stretching the fibre at high temperature [51], boron-doping and neutron irradiation [52,53] seemed to be effective methods although they are not commercially viable. For MP-based fibres, however, high tensile modulus can be achieved by treatment at high temperature. Values of the tensile modulus of some PAN- and MP-based carbon fibres are given in Table 1-1.

1. 5. 1. 2. Tensile strength

Studies of the tensile strength of carbon fibres have been reviewed by Johnson [54,55]. Unlike the theoretical Young's modulus, the theoretical tensile strength of a solid is difficult to evaluate [56]. Generally, the Orowan-Polanyi equation is widely accepted as one approach to calculate the theoretical tensile strength σ_t,

$$\sigma_t = (E\gamma_a/a_d)^{1/2}$$

Where γ_a is the surface energy, and equal to 4.2 J/m^2 for the prismatic bonds in graphite [54], a_d is the distance between the planes which are to be separated by the applied tensile stress and E is Young's modulus. For perfect graphite a theoretical strength of 100 *GPa* was calculated from the above expression [54]. However, the practical strength is always much more lower than the theoretical one due to the existence of defects. For example, the tensile strengths of type I fibres (E=370 *GPa*) and type II fibres (E=300 *GPa*) are about 2.8 *GPa* and 5.7 *GPa* respectively. For a graphite whisker, the most perfect form of fibrous carbon so far produced, the tensile strength can reach 20 *GPa* with a Young's modulus of 680 *GPa*. In brittle solids the defect can be considered to be small cracks (acting as stress concentrators), and which grow under the action of a stress σ_t if they are greater than a critical size C as determined by the Griffiths relationship,

$$\sigma_t^2 = 2E\gamma_a/\pi C$$

For a graphite whisker the critical flaw size is 4.5 *nm*; for a type I fibre it is 126 *nm*, and for a type II fibre it is 25 *nm* [54].

The observed tensile strengths of some PAN- and MP-based carbon fibres are shown in

Table 1-1. Tensile properties of carbon fibres (manufacturers' data) [55,36]

Manufacturer	Fibre	E (GPa)	σ_t (GPa)	e (%)
PAN-based High Modulus (Low Strain to Failure)				
Celanese	Celion Gy-70	517	1.86	0.4
Hercules	HM-s Magnamite	345	2.21	0.6
Hysol Grafil	Grafil HM	370	2.75	0.7
Toray	M50	500	2.50	0.5
Toray	M55j	540	3.63	0.7
PAN-based Int. Modulus (Int. Strain to Failure)				
Celanese	Celion 1000	234	3.24	1.4
Hercules	IM-6	276	4.40	1.4
Hysol Grafil	Apollo IM 43-6000	300	4.00	1.3
Toho Beslon	Sta-grade Besfight	240	3.73	1.6
Union Carbide	Thornel 3000	230	3.10	1.3
Toray	M30	294	3.92	1.3
PAN-based High Strength (High Strain to Failure)				
Celanese	Celion ST	235	4.34	1.8
Hercules	AS-6	241	4.14	1.7
Hysol Grafil	Apollo HS 38-750	260	5.00	1.9
Toray	T 800	300	5.70	1.9
Toray	T1000	294	7.06	2.4
Mesophase Pitch-based				
Union Carbide	Thornel P-25	140	1.40	1.0
	P-55	380	2.10	0.5
	P-75	500	2.00	0.4
	P-100	690	2.20	0.3
	P-120	820	2.20	0.2
Osaka gas	F-140	140	1.80	1.3
Donacarbo	F-600	600	3.00	0.5
Kashima Oil Co.	HM 50	490	2.8	0.6
	HM 60	590	3.0	0.5
	HM 80	790	3.5	0.4

E--Young's modulus, σ_r--Tensile strength, *e*--Tensile strain.

Table 1-1. It should be noted that although tensile strength has been improved significantly in recent years (so far the highest values achieved for PAN-based and MP-based carbon fibres are 7 *GPa* and 3.5 *GPa* respectively) there is still a very large difference between the theoretical and practical values. It is widely accepted that the presence of gross flaws is a major strength limiting factor. This was first demonstrated by Moreton and Watt [57] who eliminated major contaminants by filtering the dope and spinning PAN precursor in a clean room. In this way the strength of the fibres could be significantly improved. Additional confirmation was obtained by Jones, Barr and Smith [58] who deliberately contaminated the mesophase pitch precursor and found that subsequent fibre strength decreased considerably.

1. 5. 1. 3. Tensile failure models

(A) Reynolds-Sharp model

A well known model for tensile fracture is shown in Figure 1-13 [59]. It was based on the work of Reynolds and Sharp who considered that crystallites are weakest in shear on the layer planes and so tensile fracture will occur in regions where the layer planes are locally misoriented [60]. As illustrated in Figure 1-13, when misoriented crystallites are subjected to a tensile stress, the shear stress will be produced. Since the shear stress can not be relieved by cracking or yielding between layer plane the shear strain energy as stored may be sufficient to cause basal-plane rupture in the misoriented crystallites, and subsequently a crack is formed across the misaligned layer plane. The rupture of one crystallite by this failure mode would not lead to fibre rupture unless the crack continued to propagate across neighboring crystallites by transference of shear stress.

This can only occur if either one of two conditions are fulfilled:

(1) the crystallite size in one of the directions of propagation of a crack (L_c or $L_{a\perp}$) must be greater than the critical flaw size C (failure in tension as determined by the Griffiths equation).

(2) The crystallite which initiates catastrophic failure must be sufficiently continuous with its neighboring crystallites for the crack to propagate.

It was found that the first condition is not normally fulfilled because both L_c and L_a are much less than the critical flaw size C. The second condition is most likely to be satisfied in regions of enhanced crystallization and misorientation observed around defects. Bennett *et al.* [59] examined the possibility of such a mechanism by direct electron microscope observations on PAN-based carbon fibres containing many flaws. They

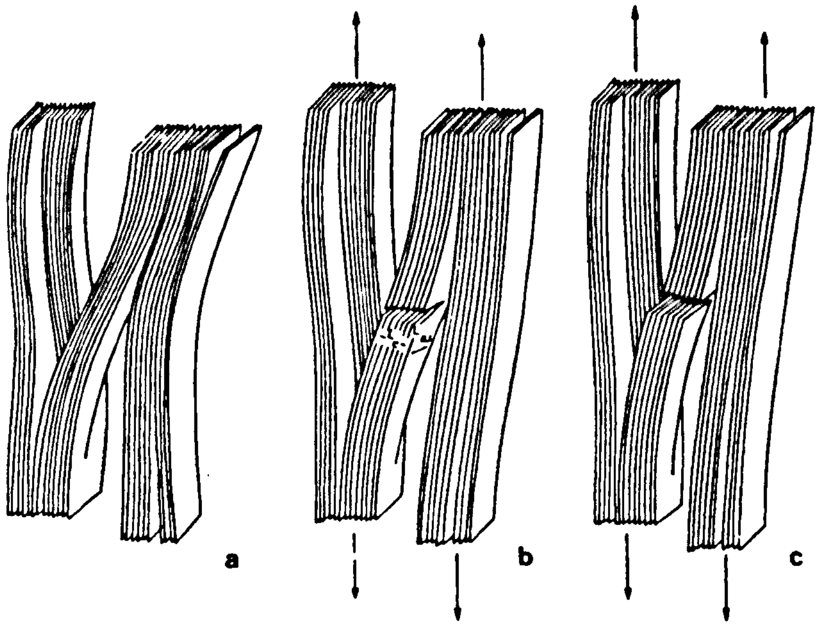

Figure 1-13. Reynolds-Sharp model of tensile failure. (a) misoriented layers linking two crystallites parallel to fibre axis. (b) Tensile stress applied parallel to fibre axis causes layer-plane rupture in direction $L_{a\perp}$, crack develops along $L_{a\perp}$ and L_c. (c) further application of stress causes complete failure of misoriented crystallite [59].

observed that internal flaws which did not initiate failure have walls containing crystallites arranged mainly parallel to the fibre axis, and internal surface flaws which did initiate failure exhibited large misoriented crystallites in the walls of the flaws. Therefore they concluded that it is the presence of misoriented crystallites rather than the flaw itself which determines whether or not tensile failure will occur, which is consistent with the Reynolds-Sharp model.

As discussed above, whether or not fibre rupture occurs depends upon the propagation of the crack through adjacent crystallites. Guigon *et al.* [33,34] suggested that the tensile strength correlates with the radius of the layer folding in the case of PAN-based carbon fibre. Endo [36] also studied the relationship between structure and tensile properties of some MP-based carbon fibres and found that the tensile strength of carbonic fibres (possessing a folded layer structure) is about 1.5 times that of Thornel fibres (consisting of relatively flat layer planes). Therefore he considered that the propagation of a fracture crack will possibly be impeded by folded layer planes resulting in an improved tensile strength. On the basis of this idea he proposed a model shown in Figure 1-14 to illustrate the propagation of fracture cracks in the case of MP-based

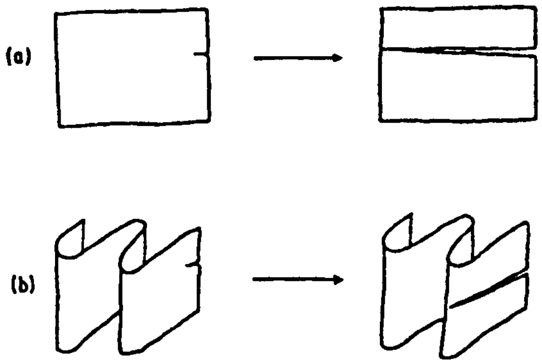

Figure 1-14. Profile of fracture model for MP-based carbon fibre with (a) a flat structure unit,and (b) a folded structure unit [36].

carbon fibres. For a flat layer structure the resistance to crack propagation is low; while for a folded layer structure the resistance to crack propagation is increased.

1. 5. 2. Compressive properties of carbon fibres

1. 5. 2. 1. Compressive strength

It is well known that the compressive strength of a fibre composite is directly related to the compressive strengths of the fibres themselves [61,62]. Unfortunately the compressive strengths of carbon fibre are significantly lower than their tensile strengths [63]. Since the low compressive strength of carbon fibres forms a major limitation to the broader usage of carbon fibre composites, recently considerable effort has been focused in understanding the compressive behaviour.

DaSilva and Johnson [64] studied the flexural behaviour of PAN-based carbon fibres. They concluded that fibres containing sheetlike structures are more brittle and thus have a lower compressive strength than those containing more highly inter-linked random structures. Kumar and Helminiak [63] have shown that the compressive strength decreases with increasing the thickness of the graphite crystallites and decreasing the interlayer spacing. Dobb *et al.* [65], after studying the compressional behaviour of PAN- and MP-based carbon fibres using the single fibre recoil test method, also concluded that the relatively low compressive strength of high-modulus MP-base carbon fibres arises from the high degree of order and inherent sheet-like microstructure. Therefore it appears that an extensive highly ordered graphitic structure will tend to lead to a low compressive strength.

Kumar [66] investigated the influence of structure and morphology on the compressive strength of MP-based and PAN-based fibres as well as a rayon-based fibre and concluded that the width of the graphitic sheets, the crystallite sizes, the preferred orientation and the interlayer spacing play significant roles in accounting for the large differences between compressive strengths of various carbon fibres. In addition, for carbon fibres from a given precursor, the compressive strength decreases with increasing tensile modulus. This effect arises not because of the increased orientation , but because of the increased crystallite size. If the fibre orientation could be increased while limiting the increase in L_c and $L_{a//}$, then fibres with high modulus and relatively high compressive strength could possibly be produced.

Edie *et al.* [67] studied the compressive strengths of two types of MP-based fibres using the tensile recoil test and found that the compressive strengths of Du Pont fibres with folded-radial textures are superior to that of Thornel fibres with flat-layer textures at all modulus levels. They considered that the folded-radial texture tends to inhibit shearing of the basal planes and hence account for the comparatively large compressive strengths.

Northolt *et al.* [68,69] suggested that there is a strong correlation between the compressive strength and shear modulus of carbon fibres. He found that non-graphitized PAN-based fibres have a considerably higher shear modulus than the pitch-based fibres, which, he supposed, may be caused by more cross-links between the layer planes of PAN-based fibres (graphitization will reduce the number of cross-links considerably). Therefore, the degree of covalent bonding between the basal planes may also be an important factor accounting for the difference in compressive strength between pitch- and PAN-based carbon fibres.

1. 5. 2. 2. Compressive failure models

(A) Park's model

Park *et al.* [65] further studied the compressive failure mechanisms after tensile recoil tests and proposed failure models for PAN-and MP-based carbon fibres. Figure 1-15a indicates that PAN-based fibres typically buckle on compression and form kink bands at the innermost surface of the fibre. A crack initiated at the side under tension can be seen as it propagates across the fibre. Subsequently a stepped fracture face is formed at 90^0 to the fibre axis. In contrast, MP-based fibres deform by a shear mechanism with kink bands formed at 45^0 to the fibre axis as shown in Figure 1-15b. This kink band will initiate oblique rupture across the whole fibre on further deformation. However, an exception was reported for MP-based P-25 low modulus fibre which follows the failure mechanism for PAN-based fibres.

(B) Edie's model

Edie *et al.* [67] observed the failure surfaces of MP-based carbon fibre after recoil testing and found that the fibres may be bent slightly before either buckling or shearing occurred. The lower-modulus fibres exhibit stepped fracture indicative of combined tensile and compressive failure. This result led them to conclude that during the recoil test, a macroscopic lateral displacement may occur due to the dimension of the test specimen as shown in Figure 1-16. This lateral displacement travels along the fibre length with the zero stress front, and exhibits characteristics of a wave whose amplitude is inversely dependent on the tensile modulus of the fibre.

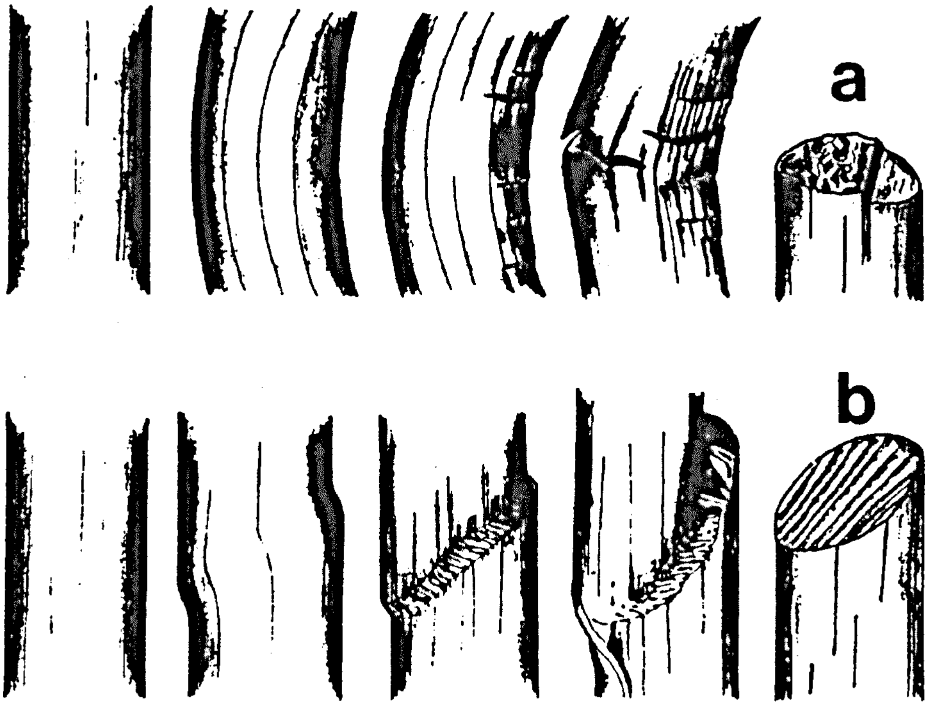

Figure 1-15. Schematic diagram of compressive failure mechanisms in (a) PAN-based (b) MP-based, carbon fibres [65].

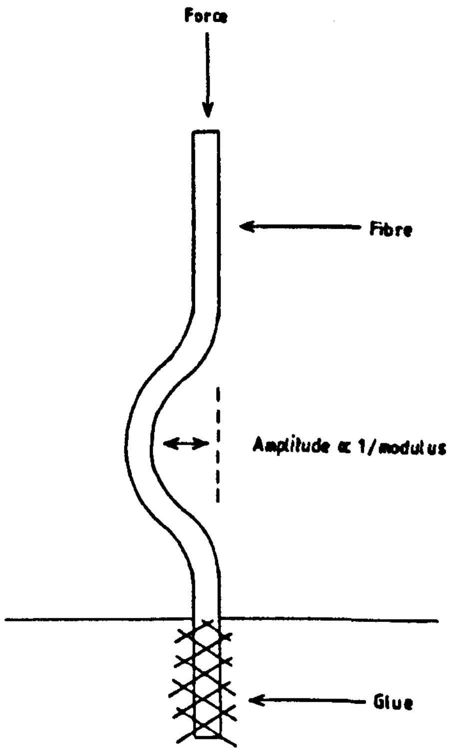

Figure 1-16. Edie's model showing the lateral displacement of the fibre under the tensile recoil test [67].

1. 6. The scope of this work

It is well known that with carbon fibres the compressive strength is significantly lower than the tensile strength, especially in the case of mesophase pitch-based fibres. Since the mechanical properties of fibres depend mainly upon their structures, apparently the improvement in mechanical performance can only be achieved on the basis of a detailed understanding of structure property relations of fibres. Recently such investigations have been carried out by other workers (as reviewed previously), however a further and complete understanding of compressive behaviour of carbon fibres is necessary.

Therefore, this work has been mainly focused on :

(1) Structural studies of a particular range of MP-based carbon fibres, including both macrostructure and microstructure. In particular, for the first time microstructural parameters were determined quantitatively from TEM micrographs using image analysis techniques.

(2) The investigation of compressive behaviour of MP-based carbon fibres. Compressive strengths of the fibres were measured and failure mechanisms were proposed.

(3) The establishment of possible structure property relations in MP-based carbon fibres. The influence of both macro- and microstructure on the fibre compressive strength are discussed thoroughly in the final chapter.

Chapter 2

Experimental Aspects

2. 1. Materials

All the samples examined in this work were mesophase pitch-based carbon fibres manufactured by the Du Pont company. The code names, together with their values of Young's modulus, tensile strength, and elongation are listed in Table 2-1.

Table 2-1. Single filament tensile properties of Du Pont MP-based carbon fibres

Fibres	Young's Modulus (GPa)	Tensile Strength (GPa)	Elongation (%)
E35	224	2.38	1.02
E55	374	3.05	0.74
E75	490	2.92	0.58
E105	750	3.10	0.48
E120	857	3.19	0.44
E130	905	3.59	0.48
E35C	237	2.54	1.02
C700	871	3.37	0.49

Notes:
E35, E55, E75, E105, E120 and E130 fibres are grouped into high modulus fibre G products;
E35C and C700 fibres are high thermal conductivity fibres.

2. 2. Structural studies

2. 2. 1. Scanning Electron Microscopy (SEM)

2. 2. 1. 1. Principle

The layout of a typical SEM is shown schematically in Figure 2-1. Electrons, which are emitted from an electron gun (usually a hot tungsten filament), are accelerated down a vacuum column by applying a high voltage between the cathode and anode. The electron beam is then focused to a fine probe (by the electromagnetic lenses) which is scanned in the form of a raster across the specimen surface. The specimen is mounted

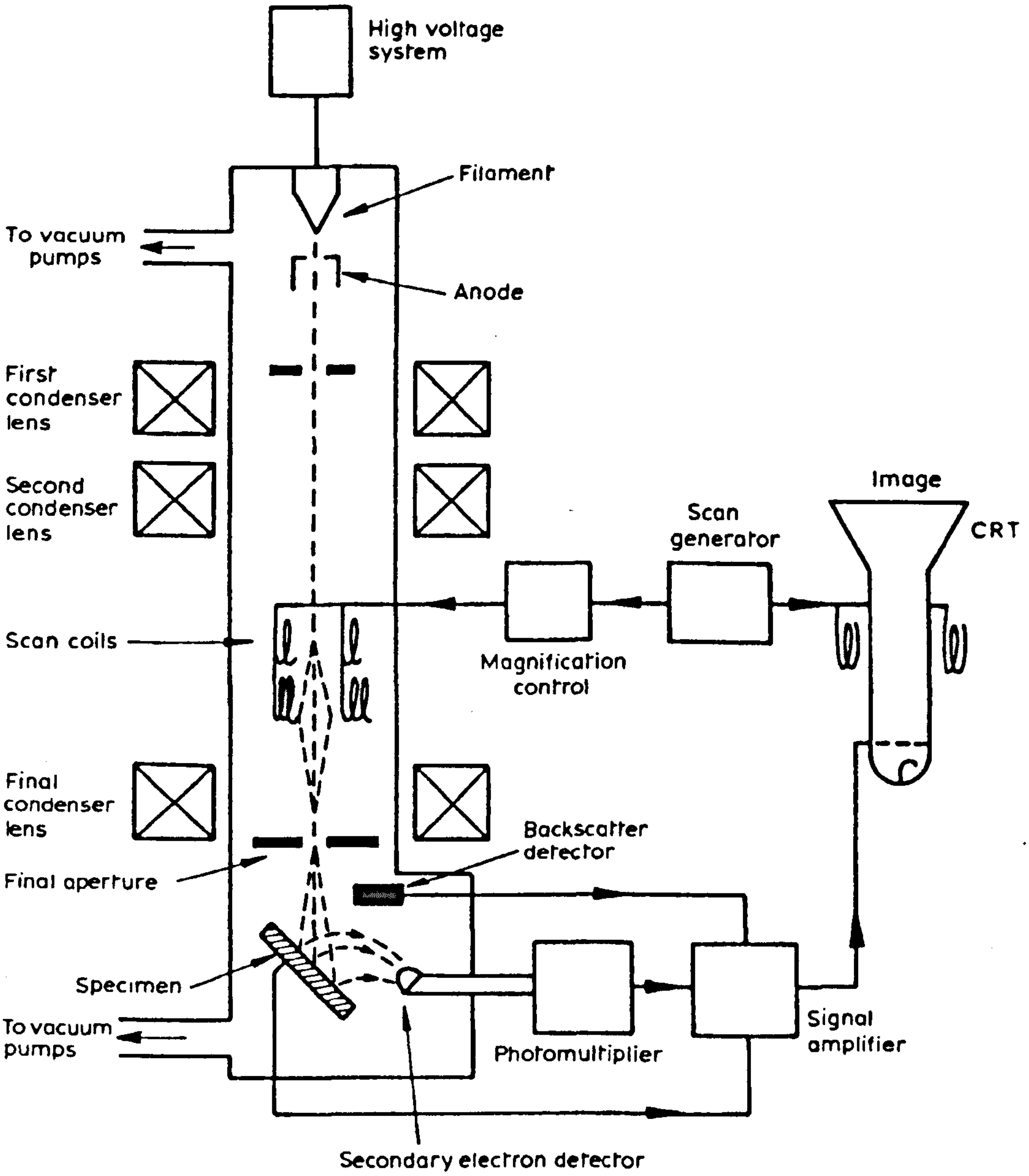

Figure 2-1. Schematic block diagram of a scanning electron microscope [70]

on a stage, which allows specimen translation, tilting or rotation in an evacuated chamber. When the electron beam is scanned over the specimen surface, two main types of electron are emitted from the specimen, namely, (1) low-energy secondary electrons (SE), and (2) high-energy backscattered electrons (BE). These two types of electrons are usually detected by different electron collector systems. The detection of SE is optimized by applying a small positive bias on the front of the detector, which allows them to reach a positively biased scintillator [71]. Usually some backscattered electrons moving in the direction of the scintillator are also detected. The emitted light travels along a light guide to a photomultiplier tube. Amplified signals from the photomultiplier are used to modulate the electron beam in a display cathode ray tube. The backscattered electrons can be picked up by a second detector and also used to display an image.

The important advantages of scanning electron microscopy over light microscopy include the larger depth of field, the wide range of magnification and the much improved resolution ($<5nm$). In most cases, the specimen preparation and the image interpretation are relatively easy. In addition, since the information is available in the form of an electronic signal, it can be processed in various ways to present images in different forms.

2. 2. 1. 2. Experimental procedures

The specimens were prepared for SEM observation as follows. Fibres were mounted in parallel on an aluminium sheet using silver dag glue, and cut with a sharp razor blade to produce cut face sections. The fibre assembly was then clamped into the specimen holder and placed in a Polaron Coating Unit E5000. The samples were then sputtered with a thin layer of gold (app. 20 *nm*) [72]. The purpose for doing this is to increase both the electrical conductivity and the secondary electron emission coefficient of the surface. The conditions for sputtering were as follows:

Coating chamber pressure : about 0.1 *torr.*

Potential difference between cathode and specimen : 1.4 *kV.*

Leak current : between 8 *mA* and 18 *mA*.

Coating time : 7 minutes.

All samples were then examined in a Cambridge Stereoscan 360 operating at an accelerating potential of 10 *kV.*

2. 2. 2. Transmission Electron Microscopy (TEM)

2. 2. 2. 1. Principle

Unlike the scanning electron microscope, the transmission electron microscope produces images by a system of lenses which allows electrons to pass through a thin specimen. The interaction of a beam of electrons with a thin specimen is complex [73]. The transmitted electrons can be classified into three types, namely, (1) directly transmitted electrons which pass through the specimen with little change of direction or energy, (2) elastically scattered electrons, which are deflected through relatively large angles due to atomic collision without loss of energy, and (3) inelastically scattered electrons which normally undergo both a directional change and a partial energy loss.

The amplitude contrast (due to elastically scattered electrons being removed by the objective aperture), together with phase contrast (due to elastically scattered electrons passing through the aperture and interfering with the direct beam), produce the overall contrast of an image. For crystalline materials, electron scattering at discrete angles (arising from diffraction by the lattice planes) occurs.

In practice, the contrast of a given specimen is usually varied by changing the angular size of the objective aperture or by adjusting the accelerating potential of the electrons.

2. 2. 2. 2. Modes of operation

Bright-field image (BF)

A bright-field image in the TEM is formed when the directly transmitted electrons combine with a limited number of scattered electrons as determined by the size of the objective aperture.

Dark-field image (DF)

A dark-field image in TEM is formed by the scattered electrons only (the direct beam is completely removed). The simplest way to obscure the directly transmitted electrons and produce a dark-field image is by displacing the objective aperture as shown in Figure 2-2a. However the image formed is of poor quality due to spherical aberration caused by off-axis electrons. In practice, high quality dark-field images are formed by tilting the incident electron beam at such an angle that the scattered beams of interest travel down the axis of the objective lens and pass through the aperture, whilst the direct beam is obstructed by the aperture as shown in Figure 2-2b.

The dark-field mode is particularly important for studying crystalline materials. The

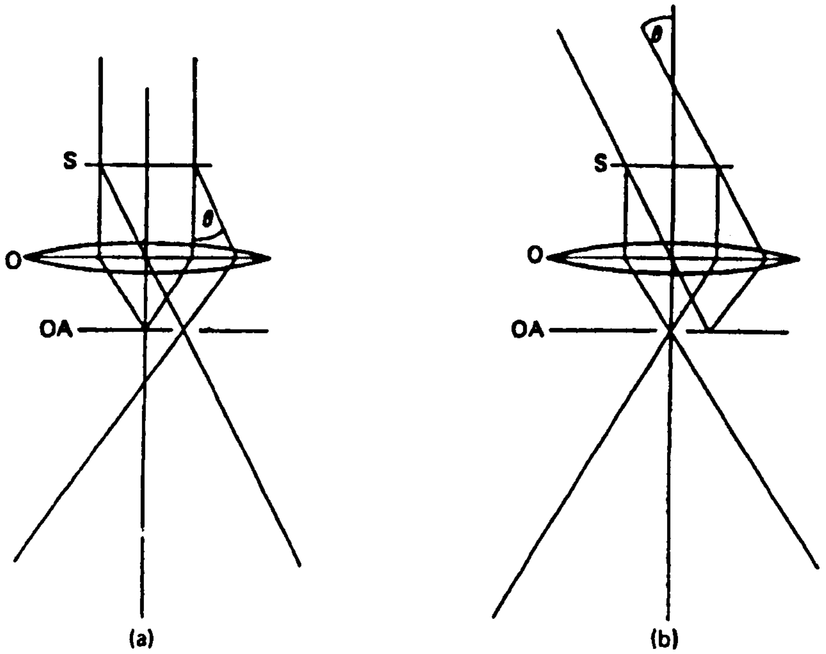

Figure 2-2. Formation of dark-field images by (a) displacing the objective aperture (OA) from the axis of the objective lens, and (b) tilting the incident beam through an angle θ [74].

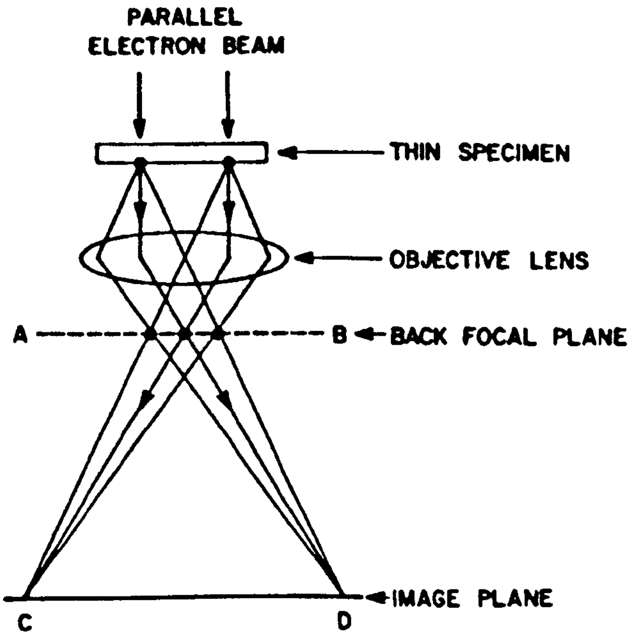

Figure 2-3. Formation of the diffraction pattern in the back focal plane (AB) of the objective lens in the TEM [71].

bright regions in the images are formed by appropriate diffracted beams arising only from crystalline domains in the specimen. Consequently the crystallite size and orientation can be measured.

Selected area electron diffraction (SAED)

In crystalline specimens electron beams will be diffracted at specific angles, which depend on electron wavelength and crystal lattice spacing according to Bragg's law. These diffracted electrons can be focused in the back focal plane of the objective lens and form diffraction patterns as shown in Figure 2-3. If a selected aperture of diameter D is now inserted in the back focal plane of the objective lens (of magnification M), then only those electrons diffracted from an area of diameter D/M on the specimen will reach the final screen. This technique is know as selected area diffraction.

Typically, the selected area diffraction mode is used to identify phases in an inhomogeneous specimen since it is possible to take diffraction patterns from different small areas of the specimen. A correlation between the features observed on the micrographs and the crystallography of the specimen can then be made.

Lattice-fringe image (LF)

Lattice-fringe images are formed when the direct beam interferes with diffracted beams. The intensity of phase contrast in the image is complex [73] but is now well understood. Depending on the focal condition of the objective lens, an image with periodic variations in intensity can be produced. A particular set of lattice planes can be resolved only if there is a strong diffracted beam due to that set of planes. The formation of the lattice-fringe image is illustrated in Figure 2-4. Generally, lattice-fringe images are greatly influenced by spherical aberration, however this is reduced when tilted illumination is employed. However, the actual interference fringes are complicated by other factors, such as crystal thickness, deviation from the Bragg condition, incorrect focusing etc. [75]. Therefore the lattice-fringe patterns of crystalline specimens can only be imaged under optimum conditions of microscope alignment and very high magnification. It should be noted that some crystals are very sensitive to the electron beam and rapidly degrade, thus preventing the recording of lattice-fringe images.

This imaging mode is typically used to detect and locate crystal lattices and their imperfections. Furthermore with the development of image processing technique, it is possible to quantify the lattice imperfections in the specimens from lattice-fringe images.

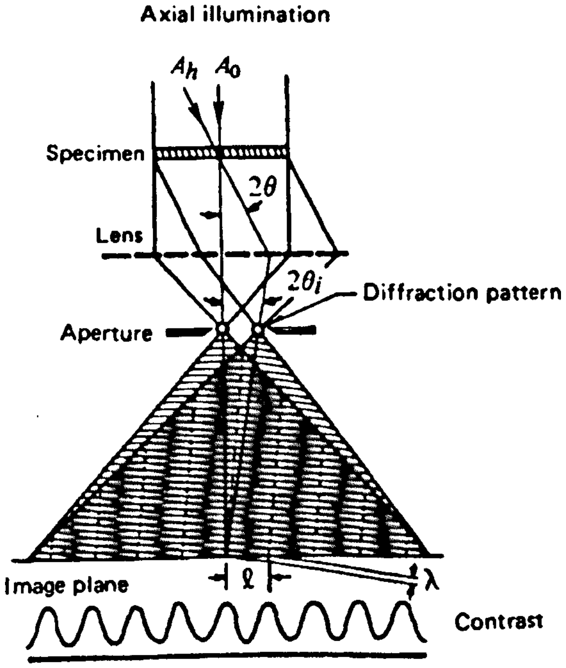

Figure 2-4. Formation of the lattice-fringe image by interference of two beams [75].

2. 2. 2. 3. Experimental procedures

Single fibres were embedded in a hard resin to form a specimen block. The composition of the embedding resin was :

Agar Resin 100 : 12 *ml*

DDSA (Dodecenyl succinic anhydride) : 4 *ml*

MNA (Methyl nadic anhydride) : 9 *ml*

BMPA (Benzyl dimethylamine) : 0.5 *ml*.

The specimen blocks were then cured for 48 hours at 70^0 *C*, and cut longitudinally on an LKB Ultramicrotome equipped with a diamond knife. A series of thin sections (showing silver or grey optical interference colours) were carefully collected on 200 mesh copper grids covered previously with a thin carbon supporting film.

The longitudinal thin sections were examined in a JEOL 100CX transmission electron microscope operating at 100 *kV*. For lattice-fringe imaging, the objective aperture was removed so that all the diffracted beams interfere with the direct beam. The images were recorded at an instrumental magnifications of 300,000x. In order to obtain good images, it was very important to correct astigmatism on the phase structure of the carbon support film. For selected area electron diffraction studies, a 25 μm aperture was chosen giving a selected area diameter of approximately 1 μm. The patterns were recorded for exposure times of 4 to 16 seconds with an effective camera length of about 800 *mm*. Tilted beam dark-field images were recorded using the 002 reflection at a magnification of 30,000x. A small objective aperture (20 μm) was used to exclude all other reflections. The exposure times for dark-field images was from 4 to 8 seconds.

All images were recorded on Kodak 4489 plates (6.5x9 *cm*), developed for 4 minutes in a solution of 2:1 (v/v) water : diluted Kodak D-19 developer, and fixed with Kodak FX-40 for at least 10 minutes.

2. 2. 3. Wide-Angle X-ray Scattering (WAXS)

2. 2. 3. 1. Principle

X-ray diffraction occurs when a parallel X-ray beam is scattered in phase by atoms in a materials. The directions of possible diffraction depend only on the packing of the atoms or molecules, which in a crystalline material are defined in terms of a unit cell. The intensities of the diffracted waves depend on the type and arrangement of atoms in the crystal structure. Thus studies of the geometry and intensities of diffraction from a crystalline material can be used to find the unit cell dimensions and arrangement of atoms.

X-ray diffraction can be mathematically described by Bragg's law, $n\lambda=2dsin\theta$, where n is an integer referring to the order of the reflection, λ is the wavelength of a monochromatic X-ray beam, d is the interlayer spacing and θ is the half angle of scattering. The ideal diffraction intensity from a crystal is given by $I = |F_{hkl}|^2$, where F_{hkl} is known as the structure factor and is defined as :

$$F_{hkl} = \sum_{n=1}^{N} f_n exp2\pi i(hu_n + kv_n + lw_n)$$

where (hkl) are the Miller indices, u_n, v_n and w_n are the fractions of unit cell edges, f_n is the atomic scattering factor, and N is the total number of atoms in the unit cell.

In practice, in order to achieve accurate measurement of structural parameters using X-ray diffraction methods, the above ideal intensity should be modified by the following factors [76] :

1. Specimen absorption factor; because the incident and reflected beams are partially absorbed in passing through the specimen, consequently the scattered intensity is less than it would be from a perfectly non-absorbing substance. The effect of this absorption is dependent on the absorption coefficient and thickness of the specimen. Therefore the observed intensity data should be appropriately multiplied by an absorption factor to obtain the corrected intensity.

2. The Lorentz factor; in most X-ray methods the specimen is given a controlled motion in the path of the X-ray beam. Various planes in the crystal are therefore successively presented to the beam at their Bragg angles and are given an opportunity to diffract. The rate at which the planes pass through the Bragg condition varies with the diffraction angle, and therefore each intensity measurement must be separately corrected for the time that a particular plane spends in rotation through the Bragg angle. The form of this correction is known as the Lorentz factor.

3. Air scattering and absorption factor; the X-ray beam is scattered and absorbed by air during the passage from the source to the detector and continuous scattering will overlap the X-ray diffraction spectrum of the specimen.

4. Incoherent scattering factor (Compton scattering); refers to the inelastic scattering which is a result of the exchange of energy between a photon of wavelength λ and an electron. A detailed explanation can be found in the reference [76].

2. 2. 3. 2. Experimental procedures

Measurement of interlayer spacing d_{002} using a diffractometer

The Spectrolab series 3000 diffractometer is based on a 120^0 curved position sensitive detector (referred to as PSD). It is a gas flow proportional counter operating at a pressure of 6.5 bar and a nominal flow rate of 30 *ml/min.*. The diffractometer was controlled by a Dell 220 system PC which governs all timings, data collection and data analysis. The X-ray diffraction spectra were plotted on a DXY-1300 x-y plotter.

The optimum thickness t of the specimen used for X-ray diffractions is generally given by $t=1/\mu$, where μ is the linear absorption coefficient of the specimen. For wide-angle X-ray diffraction of polymers the thickness of the specimen is usually taken as 0.5~1.0 *mm* [77]. Therefore, in this work a parallel bundle of fibres (app.1 *mm* thickness) was mounted on to the X-ray specimen holder in a vertical position. In order to obtain accurate d-spacings of the carbon fibres, the calibration standard material, a 3 *mm* square silver foil was placed in the middle of the fibre bundle. The specimen was then mounted on the PSD diffractometer, and the diffraction spectra were obtained using nickel filtered C_uK_α radiation (λ=1.541 Å) at an accelerating potential of 40 *kV* and a tube current of 16 *mA* for a count time of 30 minutes.

Using software mounted on the Dell PC the 002 peak occurring in each spectrum was then fitted to a Gaussian distribution. The peak position and interlayer spacing d_{002} were determined using the diffraction peaks of silver (the peak position values in terms of 2θ 30.91, 38.10, 44.28, 54.97, and 64.41, and the a_0 axis value 0.4088 were used). The apparent crystallite size L_c was estimated from the uncorrected intensity data using the well known Scherrer equation, $L_c = K\lambda / B_{002}\cos\theta$,Where λ is the X-ray wavelength, θ is the Bragg angle and K is the Scherrer parameter. B_{002} corresponds to the half-height width or integral breadth of the (002) reflection when K=0.89 or 1.0 respectively [78].

Measurement of preferred orientation using photographic method

To obtain the X-ray diffraction patterns, fibres were mounted in a specimen holder and positioned in a flat plate camera. Extreme care must be taken to ensure that the fibres are parallel to each other in order to exclude errors from fibre misorientation. The camera fitted with a pinhole collimator was mounted on a Hiltonbrooks DG2 X-ray generator and the diffraction patterns were obtained using nickel filtered CuK_α radiation (λ=1.541Å) at an accelerating potential of 40 *kV* and a tube current of 16 *mA*. The patterns were recorded on Kodirex film with a camera length of 40 *mm* for approximately 30 minutes. The exposure time must be adjusted such that the intensity of (002) reflection falls within the linear portion of the photographic density plotted against exposure (defined as the energy per unit area in the exposed film so it is the product of the intensity and the time of exposure), i.e. the photographic density is neither saturated nor too weak, see Figure 2-5. This step was essential in order for meaningful measurement of the integral breadth of the 002 reflection as described in Chapter 4.

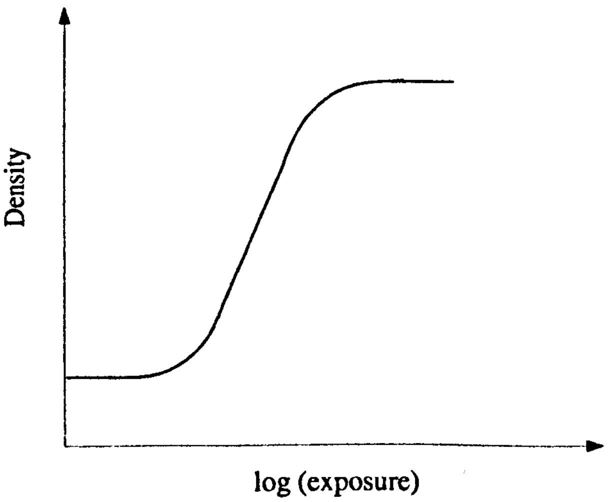

Figure 2-5. The photographic density against exposure

2. 3. Image analysis system

2. 3. 1. General introduction

Image analysis can be broadly defined as the extraction and measurement of structural parameters of areas of interest on overall specimen images. Figure 2-6 is a typical flow chart of the main steps involved in an image analysis system.

The images, which can be either micrographs from light and electron microscopes, or X-ray and electron diffraction patterns, consist of two-dimensional distributions of intensity measured by grey levels. Images can also be transferred directly to the

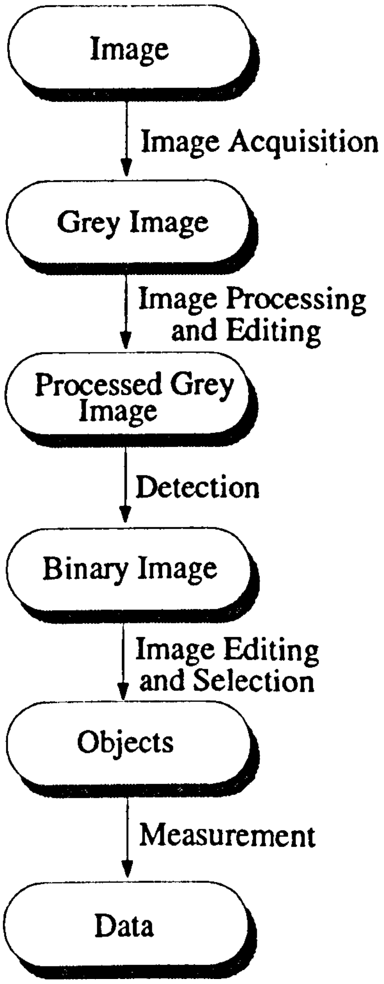

Figure 2-6. The steps involved in an image analysis system analyser from the source equipment (e.g. scanning electron microscopy or light microscopy).

The first step in the analysis is image acquisition or image capture, which usually includes storing the image from usually a video-camera. The captured image (grey image) consists of a 512x512 square grid of picture elements (pixels); the brightness of each pixel is represented by 256 discrete intensity levels (grey levels), where zero represents black and 255 represents peak white. The illumination level, magnification of the image, and image area are carefully selected, since a well-defined image makes subsequent processing and measurement simpler, faster and more precise.

Also image enhancement to improve the contrast and image filtering to smooth the noise is sometimes necessary. The major advantage of processing the grey image is that images may be manipulated taking into account the full extent of the original image data before converting to a binary form. Many techniques have been developed to process the grey image and usually they are classified into four distinct groups: (1) point transforms (pixel by pixel), (2) convolutions (multiplied by a kernel), (3) frequency-domain transforms, and (4) morphological transforms [79].

Point transforms are also known as look-up table transforms in most image analysis systems. Each pixel is transformed to a new value according to some mathematical function such as 'log', 'exp' or 'square root' and 'inverse' etc. with the result rescaled to the grey range 0~255, which is independent of its neighbours. The purpose of using these transforms is to improve the visualization of an image by stretching or compressing the grey level range.

Convolution involves sweeping an *m* x *m* kernel across the image, multiplying the elements of the kernel with the corresponding pixels in the image and normalizing the result. The resulting value at any pixel is therefore a function of its grey level and each of its m x m neighbours, weighted by the values of the kernel. Typical uses of convolutions are in image smoothing and edge or gradient detection.

A typical and most common frequency-domain transform is the Fourier transform. The principle considered in this transform is that the image is the sum of a set of sinusoidal waves of varying frequency; the higher the frequency of the sine wave, the finer the detail it refers to. Mathematically, this relationship may be stated as [80]:

$$j(x) = \sum^{h} j_h \left[cos\left(\frac{2\pi hx}{l}\right) + isin\left(\frac{2\pi hx}{l}\right)\right]$$

where $j(x)$ is the image intensity at the position x in the image with a periodicity of l; j_h is referred to as a Fourier coefficient and represents the weighting factor given to a particular sine wave of frequency $v = h / l$. Obviously there is an inverse relation between the image and its Fourier transform: small periodicities (small spacing r) correspond to high frequencies v, and any measurement of v can be related to a spacing r in the image by r =1 / v.

The Fourier coefficient j_h can be calculated from the image using the inverse relation:

$$j_h = \frac{1}{l}\int_{0}^{l} j(x) exp\left(\frac{-2\pi ihx}{l}\right) dx$$

The Fourier transform coefficient j_h holds two pieces of information: the energy information represented by the real part (the amplitude of j_h) and the phase information represented by the imaginary part (the phase of j_h). Therefore the Fourier transform contains exactly the same information as that of the original function. They differ only in the manner of presentation, i.e. real domain and frequency domain.

The Fast Fourier Transform(FFT) is simply an algorithm which calculates the discrete Fourier transform much more rapidly than other available algorithms [81].

The morphological transform is based on mathematical morphology theories which have been specifically established to solve many problems in image analysis [79]. The images are treated by a series of processing stages to remove irrelevant detail and obtain information about the contents according to the rules of the 'hit or miss' transform (HMT), which is the basic concept of most morphological functions. The value of each pixel in the output of an HMT depends on the value of the centre point in the input image and its immediate neighbours defined by the structuring element (typically a 3x3 array).

A typical morphological transform used in this work is image skeletonisation. The medial line, which is formed by nearest boundary points between opposing edges of a geometric object, is called a skeleton, and the erosion processing, in which pixels are removed from the periphery until the medial line is obtained, is known as skeletonisation [82]. Thus the final skeleton has no point in it with more than two immediate neighbors unless it is a junction.

However measurements cannot be directly based on the skeletonized images alone because some grey images have too complex a skeleton to measure due to their irregular periphery. Hence, the skeletonized image should be further processed or edited before any measurement.

Image editing is a process in which the operator interacts with the image to modify it by using a light pen (or Mouse). Detail may be added or removed from the image according to the judgement of the operator. Some of the commonly provided functions are "COVER", "DRAW" and "BRUSH" using the selected grey level.

Image detection following image processing and editing is the next logical step. The cleaned grey image can be transferred into a binary image by setting grey level thresholds to separate interested object from the background. Consequently the boundary of the objects to be measured is defined. In some case, this binary image may also require some editing, for example, to separate touching objects, complete broken lines, or smooth rough outlines.

Whether binary editing is required or not, the next step is generally measurement of the required parameters. These may be either global (field) or feature-specific parameters. Global measurements pertain to all the features in the binary image and represent data describing the property of a complete field of view, e.g. area, perimeter, count etc.. Feature measurements deal with individual features viewed in the selected image and provide statistical data indicating the property of each feature and its distribution. Generally feature measurement can be grouped into four basic categories [71]: (1) size, (2)shape, (3)position, including both the location and the orientation of features, and (4) brightness (phase identification).

It is important to note that magnification calibration must be made before a field or feature measurement (in terms of pixels) is carried out. Thus pixel size is related to some real distance.

The measured data can then be analyzed and interpreted in a number of ways, e.g. classification and statistical analysis, and clearly presented by means of graphics, histograms and scatter plots.

2. 3. 2. Instrumental aspects

A Leica Quantimet 570 image analyser was used in this work; the details of operation can be found in the manuals [79].

2. 3. 3. Definitions of the basic parameters used in this work

(*a*) *Feret diameter* (*Caliper diameter*)

The Feret diameter is defined as the distance between two parallel tangents which are on opposite sides of the object, in other words, it is the maximum dimension of an object in a specified direction. In the Quantimet 570 image analyser, it is possible to measure 64 Ferets (i.e. along 64 different directions). For example, Feret 0 is the maximum diameter measured horizontally (at 0^0 degree) and Feret 90 is the maximum diameter measured vertically (at 90^0 degrees) as shown in Figure 2-7.

(b) *Object orientation*

In the Quantimet 570 image analysis system three parameters may be used to measure the object orientation as shown in Figure 2-8: (1) the orientation angle of the maximum Feret with respect to the horizontal axis; (2) the orientation angle of the minimum Feret with respect to the horizontal axis; and (3) the calculated orientation angle, defined as the mean of the angles of Ferets having the same maximum value with respect to the horizontal axis [79].

Figure 2-7. Feret diameters measured (a) horizontally and (b) vertically [79].

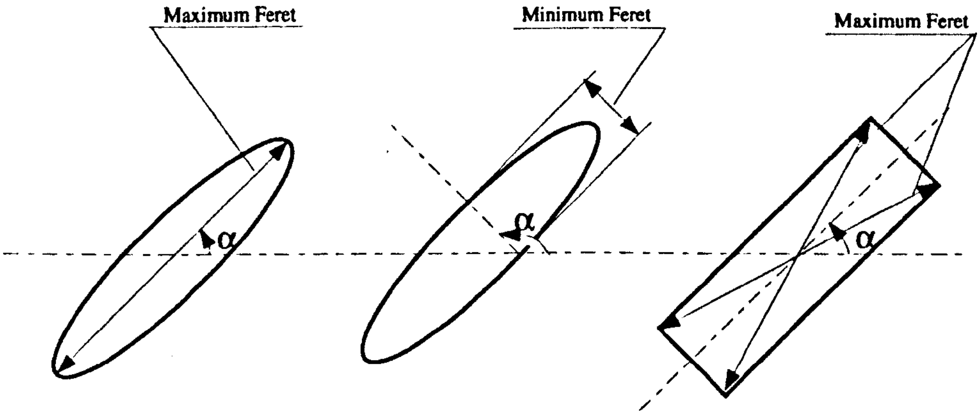

(a) (b) (c)

Figure 2-8. The definition of (a) the orientation angle of maximum Feret, (b) the orientation angle of minimum Feret, and (c) the calculated orientation angle.

2. 4. Compressional strength testing

2. 4. 1. General introduction

It is very difficult to precisely measure the single-fibre compressive strength due to the fact that it is difficult to impart purely uniaxial compressive forces to very thin fibres. A number of methods have been developed to estimate the single-fibre compressive strength [63], including : (1) the elastic loop test [83], (2)the bending beam test [84], (3) the single-fibre-composites test [62], (4) the critical fibre length method [85], and (5) the tensile recoil test [86].

In the elastic loop test, the maximum tensile or compressive strain is measured by bending a single fibre and analysing the shape of the elastic loop. The compressive strength is calculated as the product of the compressive strain and the compressive modulus (assumed equal to the tensile modulus). In the bending beam test, a single fibre is adhesively bound on to the beam and the compressive strain of the fibre is monitored while progressively bending the beam. Using the single-fibre-composite test, the compressive strain of a single fibre embedded in a matrix can also be determined by optically monitoring the fibre failure. It is clear that these three methods provide data on the compressive strain but require additional information about compressive modulus in order to calculate the compressive strength.

In the critical fibre length method, which was developed to estimate the axial compressive strengths of PAN- and pitch-based carbon fibres, a single fibre embedded in a resin matrix is compressed and the section lengths of broken fibre are measured. The fibre axial compressive strength is estimated using the average length of broken fibre and the yield shear strength at the fibre-matrix interface. The compressive strengths determined from this method may be influenced by matrix properties and the nature of the fibre-matrix interface.

In the tensile recoil test, a single fibre is compressed by the recoil force after controlled tensile stress and subsequent cutting. The recoil compressive stress is assumed to have the same magnitude as the initial tensile stress. This method, originally developed by Allen [86], appears to be the currently preferred technique to measure the compressive strengths of high performance fibres since it was considered that the fibre samples are uniformly compressed by a purely uniaxial compression forces. This test has been used in current work to measure the compressive strengths of a series of MP-based carbon fibres.

2. 4. 2. Tensile recoil test

2. 4. 2. 1. Principle

It is assumed that the fibre (1) obeys Hooke's law for a linear elastic material, (2) is rigidly clamped at each end of the gauge length, (3) has a zero initial velocity and (4) has an initial uniform tensile stress along it's length at failure except at the break location where the stress is zero. If these conditions are satisfied and dissipation effects are neglected, then the magnitude of the compressive stress generated during recoil is equal in magnitude (but of opposite sign) to the tensile stress at failure. Therefore by selectively controlling the tensile stress, a threshold stress for observation of recoil compressive damage could be determined and hence a measure of fibre compressive strength obtained.

2. 4. 2. 2. Experimental procedures

The fibres were mounted on 2 *cm* square card-holders and secured at each end with Durofix. The fibre ends on the card-holder were gripped by pneumatic jaws attached to an Instron testing machine. Then, the two sides of the card-holder were cut with a pair of sharp scissors, and the fibre stressed in an Instron to a predetermined tensile stress level. The fibre recoil was initiated by cutting the fibre quickly and steadily at the centre of the gauge length with very sharp surgical scissors. If the preselected tensile stress exceeds the critical recoil compressive strength of the fibre, compressive failure will occur. For brittle materials like carbon fibres, the failure phenomenon is catastrophic and lengths of fibre could be observed breaking away from the clamps. Observations were made for each half of the cut filament providing two results per test sample as shown in Figure 2-9. This testing procedure is schematically illustrated in Figure 2-10.

It is not possible to determine the actual compressive strength directly from a single test since the applied stress may have exceeded the critical failure strength by an unknown amount. Therefore the resultant data must be evaluated statistically in order to give correct values for the compressive strength. Currently there are two major methods of analysing the recoil data, (1) a tabulation method as proposed by Allen [86], and (2) a probability-plot method as suggested by Park [72]. In the tabulation method, the data are arranged in ascending order of applied tensile stress. A range of stress levels is identified over which the failure observations change from 100% survival to 100% failure. Subsequently the average of the applied tensile stresses between the start-point and the end-point of this range can be taken as the recoil compressive strength. In the

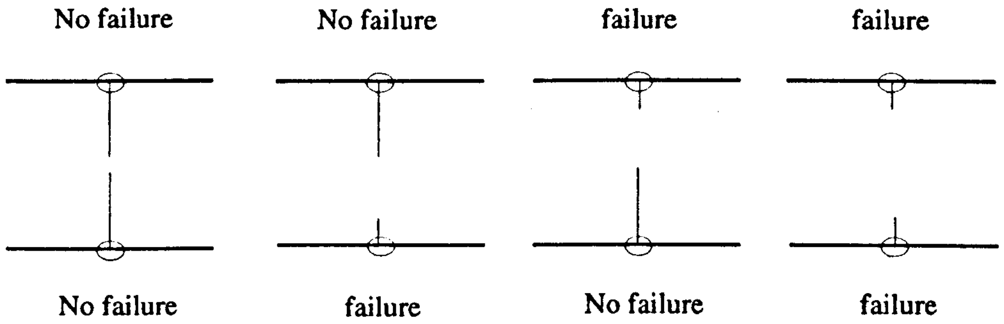

Figure 2-9. Schematic diagram showing the observation of recoiled carbon fibres

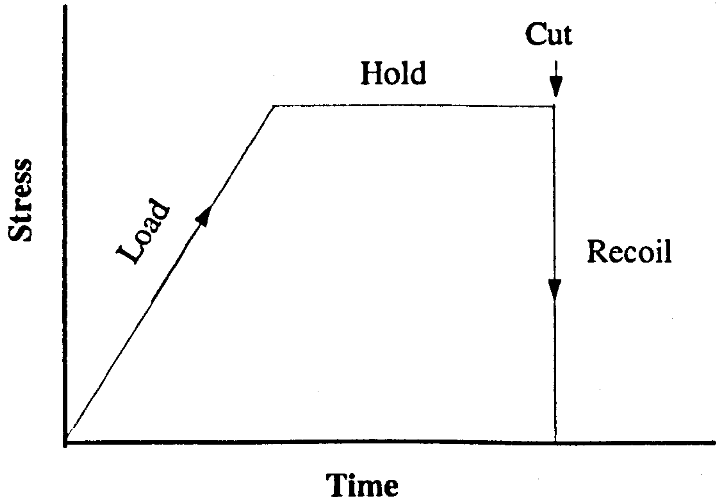

Figure 2-10. The procedure for tensile recoil testing [86].

probability-plot method, the probability of failure after compression at a given stress level was calculated from the equation,

$$Probability\ of\ failure\,(\%) = \frac{No.\ of\ failed\ fibres}{Total\ no.\ of\ tested\ fibres} \times 100(\%)$$

and plotted against compressive stress. The critical compressive strength is taken as the stress level at which there is a *50%* probability of failure. It is considered that this method provides a good graphical means of presenting the resultant data. This method was used in the current work to determine the compressive strengths from eighty samples (160 readings) for each type of MP-based carbon fibre. However, this probability-plot method has been improved in the present work. Instead of drawing the plot simply following the experimental data, the linear regression line was obtained for each sample. Clearly, the critical compressive strength decided from regression data is more reasonable statistically.

It should be noted that although 100 samples were initially prepared only eighty samples were useful since some specimens were broken due to problems of handling such brittle materials.

After each recoil test, specimens were collected and coated with a thin layer of gold as described previously in section 2.2.1, and examined in a Cambridge Stereoscan 360 operating at 10 *kV*. Two regions of the specimens were studied in detail, namely, (1) the fracture surface and (2) the anchor regions on the card-holders.

Chapter 3

Structure of MP-based Carbon Fibres

3. 1. Macrostructure of MP-based carbon fibres

3. 1. 1. SEM studies

The topography observed in the cut face cross sections of the series of MP-based carbon fibres exhibits considerable variations as shown in Figures 3-1a to 3-1h. All the high modulus fibre group (from E35 to E130) have a circular or slightly elliptical cross section, while the high thermal conductivity fibres E35C and C700 exhibit two types of cut face sections, namely, (a) a circular cross section or (b) a missing sector structure.

All fibres are characterized by folded pseudo-radial layers. The variations in the organization of the layers can be characterized in terms of four different domain structures, namely (1) irregular radial type, (2)radial-ribbon type, (3) regular radial type and (4) missing sector radial type. The schematic diagrams of the four type structures are shown in Figure 3-2.

The texture of the irregular radial type (Figure 3-2a), which is shown by E35 and E55 fibres, consists of zig-zag folding of individual layers. The folded layers are pseudo-radially oriented and appear to form domains. The amplitude of folding is irregular and the wavelength of the folding is variable. In some domains the layer folding is pronounced, while in other domains the amplitude of the layer folding is smaller although the thickness of the layers is approximately constant (0.1 μm).

In the case of the radial-ribbon type (Figure 3-2b), which was exhibited by E75 and E105 fibres, two domains are separated by a third domain which is linearly oriented along the diameter. However, in these two domains the highly folded layers appear to be pseudo-radially oriented.

For the regular radial type structure (Figure 3-2c), the smoothly and regularly folded layers are tightly packed to form a single quasi-uniform domain. This well-developed layer texture is exhibited by fibres E120, E130 and C700, which have the higher moduli in this group of carbon fibres.

As shown in Figure 3-2d, fibres E35C and C700 sometimes exhibit the missing sector radial type, and the layers form a pseudo-radial structure. Compared with fibres having a circular cross section, the fibres with a missing sector possess layers which are typically unfolded and almost planar. The difference is more pronounced in C700 fibre than in E35C. In addition the larger the angle of the missing sector, the more planar the sheets. A reasonable explanation may be that when the wedge is formed by opening along a radial crack, the compressional stress which is stored within the fibre during initial formation is released and the layers within the fibre extend. As a result, the layers become more planar.

The looped layer separated by two radial cracks in the cross section of E35C fibre as shown in Figure 3-1g_1 is of interest. The central hole of the loop probably results from a crystalline disclination, and may represent an initial stage in the formation of missing sector structure. On the other hand it may result from an initial impurity inclusion which is vaporised during filament formation at high temperature [59].

The macrostructures of the high modulus fibre group (E35~E130) have also been studied by Pennock *et al.* [44], who considered that a three-zoned texture could be identified in most fibres as shown in Figure 3-3. They found that a common texture in the core region (1~2 μm across) is an oriented structure although some radial layering or concentric layering was also observed in this region. In the sheath, the layer orientation was found to be predominantly radial but strongly folded in a zig-zag manner.

Between the core and sheath regions, the fibres generally show a transition zone, in which the layer orientation changes either abruptly or gradually into the zig-zag pattern observed in the sheath.

It is clear that the macrostructures observed in this work are generally consistent with the observation of the zig-zag folding pattern suggested by Pennock *et al.* although in the present work different domain structures rather than a three-zoned region were observed. However, the oriented core structure suggested by Pennock *at al.* was found only in the case of fibres E75 and E105 (see Figures 3-1c and 3-1d).

The missing sector structure exhibited by fibres E35C and C700 has also been found in other types of MP-based carbon fibres, e.g. P120 [72] and P130X [43]. White *et al.* [20] considered that the missing sector structure may develop from a radial structure containing a radial crack which widens on carbonization since the thermal shrinkage is much higher in the transverse than in the longitudinal direction. This is schematically shown in Figure 3-4. However, Park [72] argued against this explanation by pointing out the following facts : (1) the missing sector structure as observed in fibre P120 is developed from a deformed flat-layer rather than a radial transverse structure, (2) the origin of a radial crack is not included in the explanation, (3) on the basis of this explanation more than one "missing sector" would be formed in a fibre and (4) such a large angle of missing sector (80^0~180^0) could not be formed by thermal shrinkage alone. Park, therefore, suggested that conditions of the fibre formation and the inherent microstructural features of MP-based fibres may contribute to the formation of the missing sector structure. Indeed, it is widely accepted that various transverse structures found in MP-based carbon fibres are due to variations in the spinning conditions.

E35

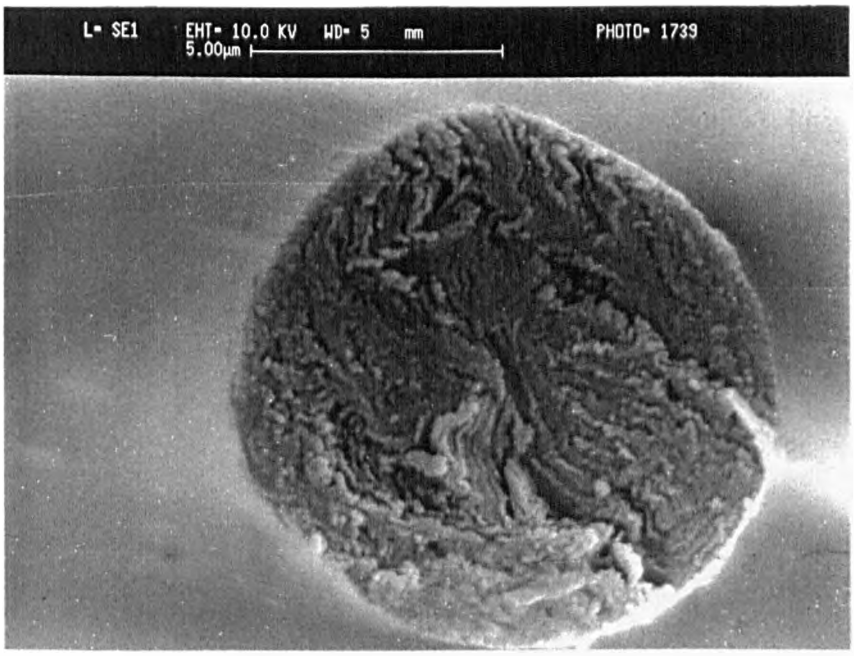

E55

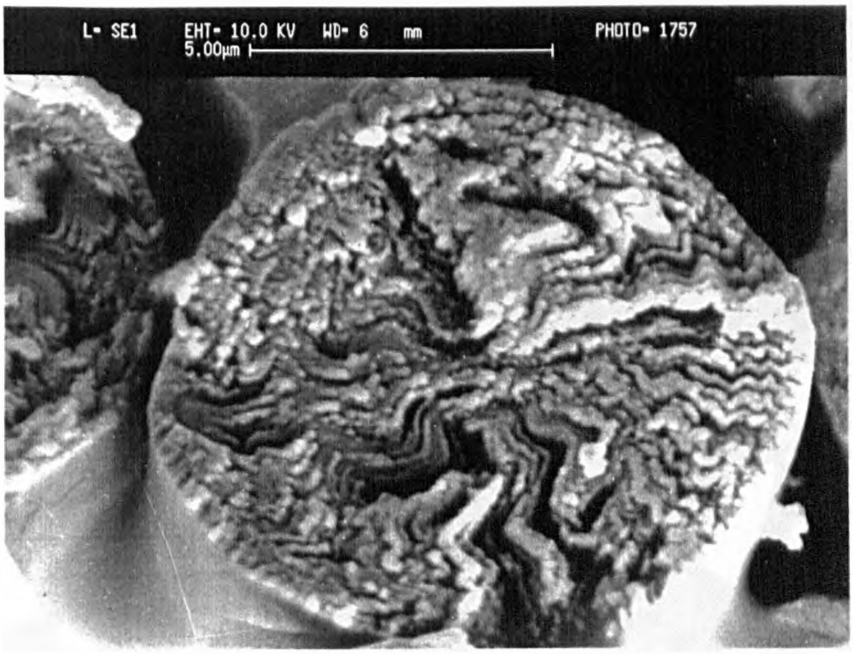

Figures 3-1. SEM micrographs from cut face cross sections of MP-based carbon fibres : E35, E55, E75, E105, E120, E130, E35C, and C700.

E75

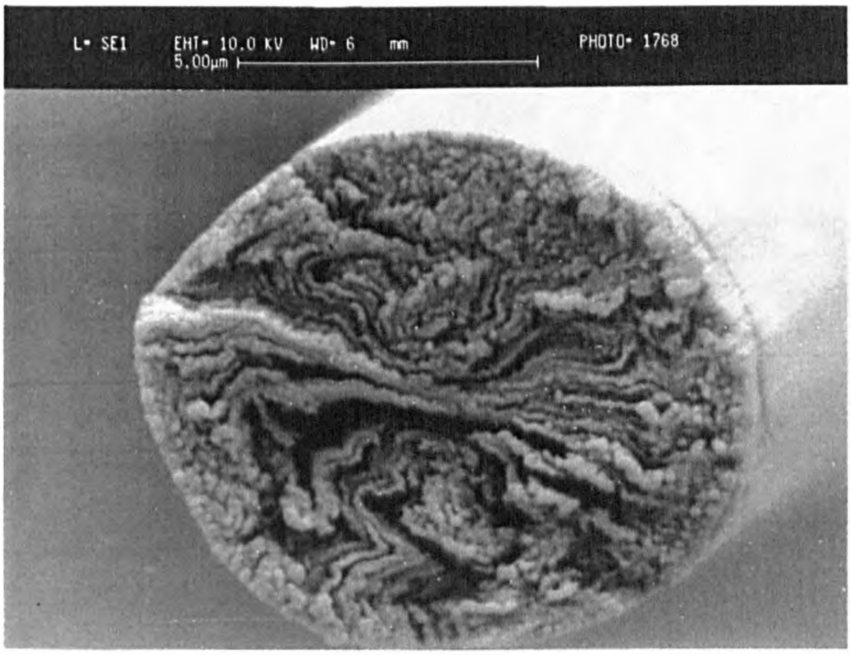

E105

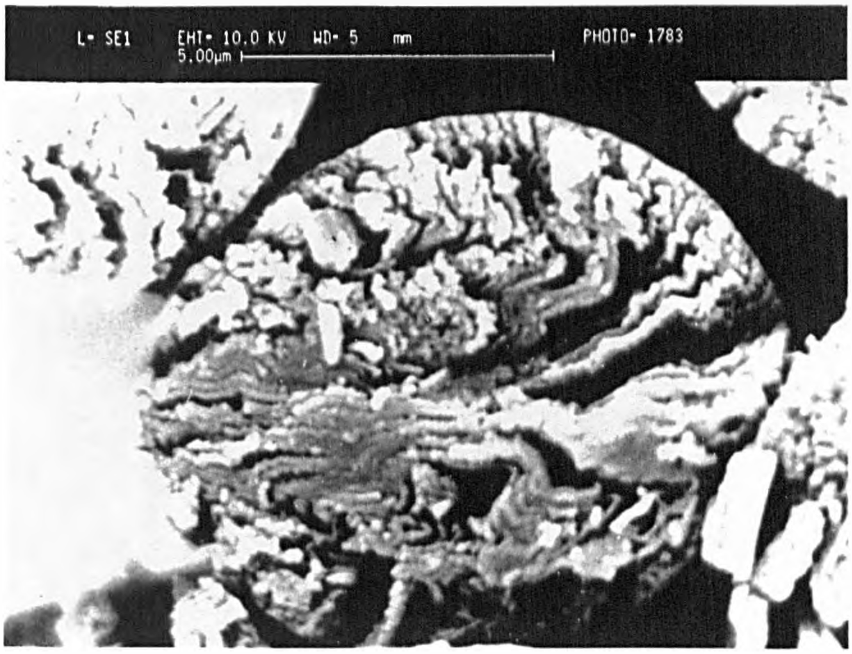

Figures 3-1. SEM micrographs from cut face cross sections of MP-based carbon fibres : E35, E55, E75, E105, E120, E130, E35C, and C700.

E120

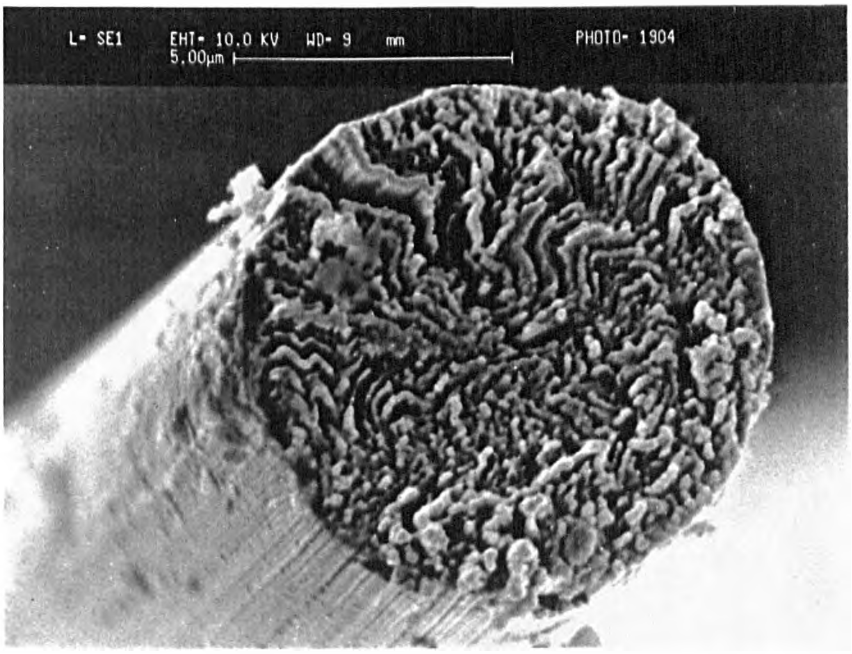

E130

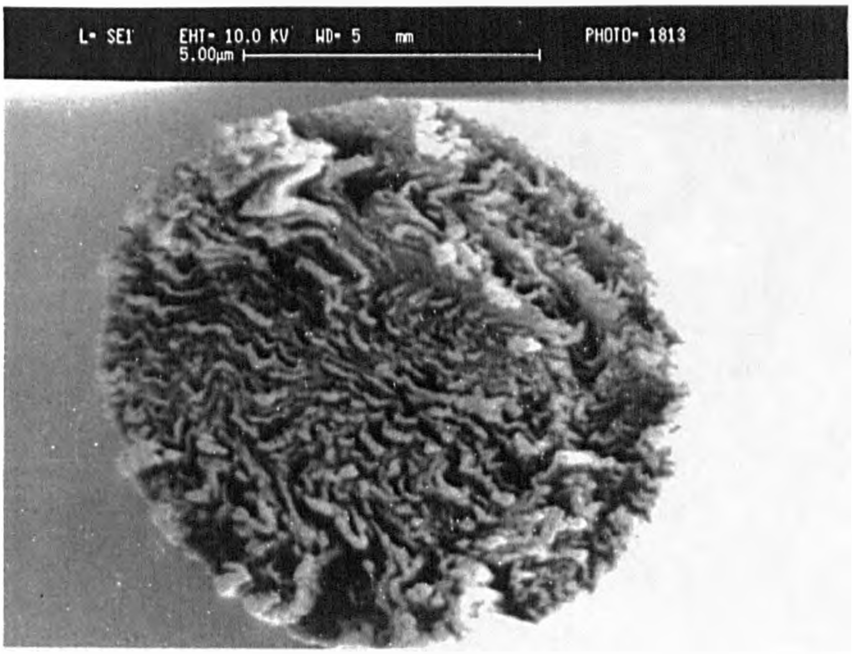

Figures 3-1. SEM micrographs from cut face cross sections of MP-based carbon fibres : E35, E55, E75, E105, E120, E130, E35C, and C700.

E35C

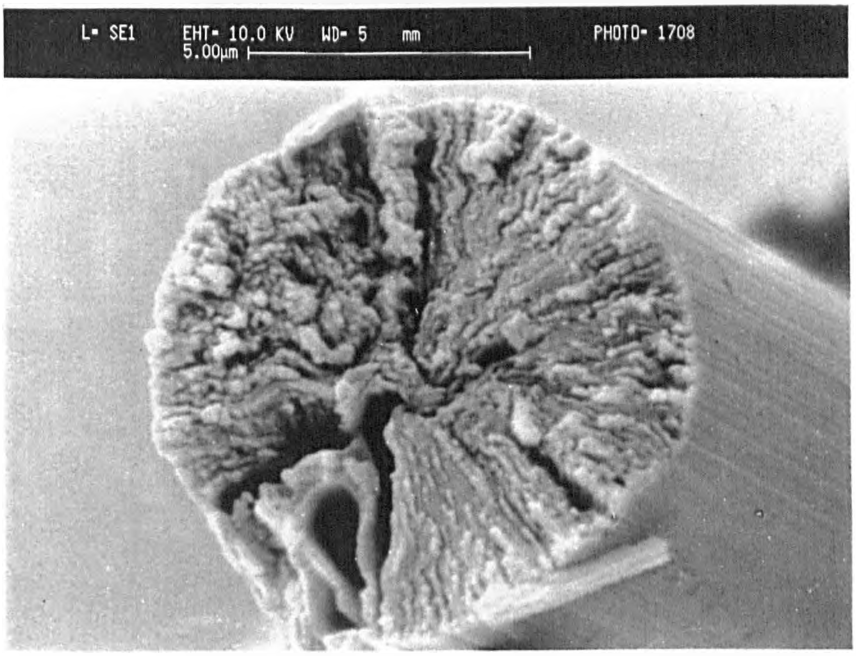

E35C with a missing sector

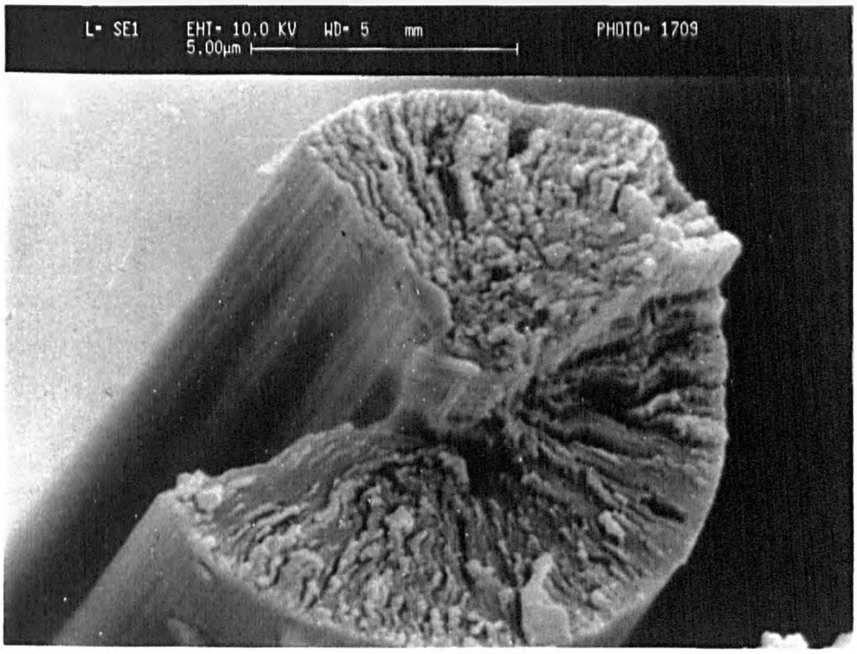

Figures 3-1. SEM micrographs from cut face cross sections of MP-based carbon fibres : E35, E55, E75, E105, E120, E130, E35C, and C700.

C700

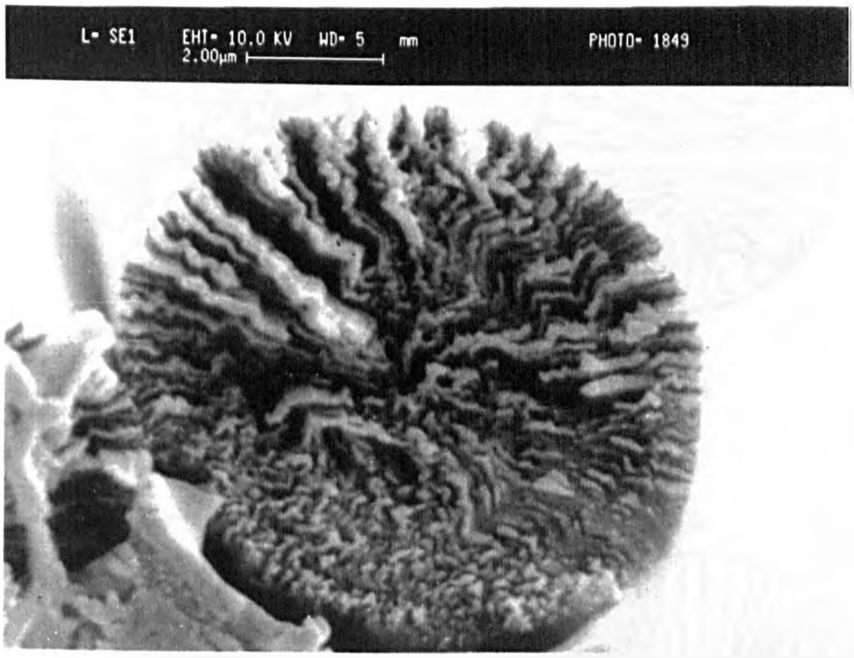

C700 with a missing sector

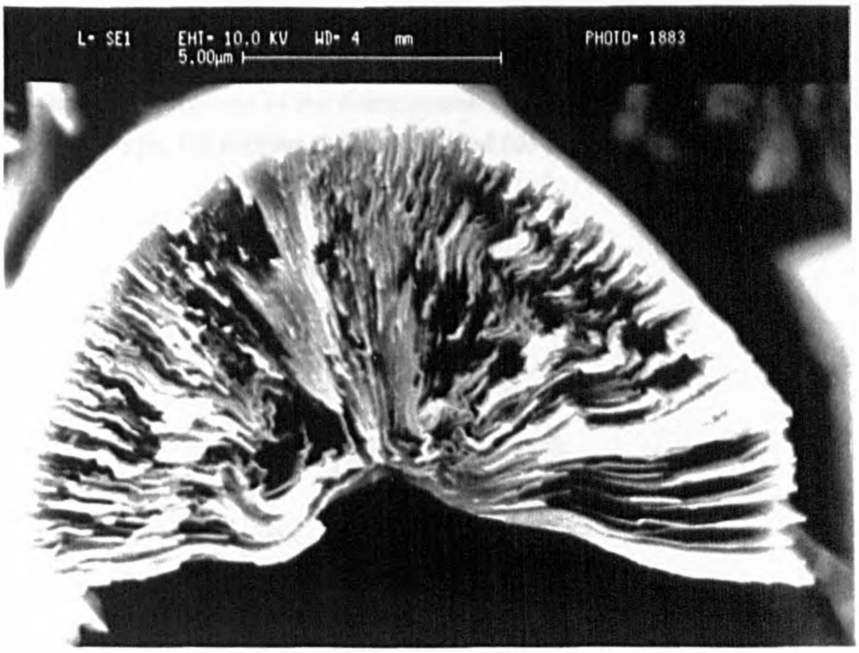

Figures 3-1. SEM micrographs from cut face cross sections of MP-based carbon fibres : E35, E55, E75, E105, E120, E130, E35C, and C700.

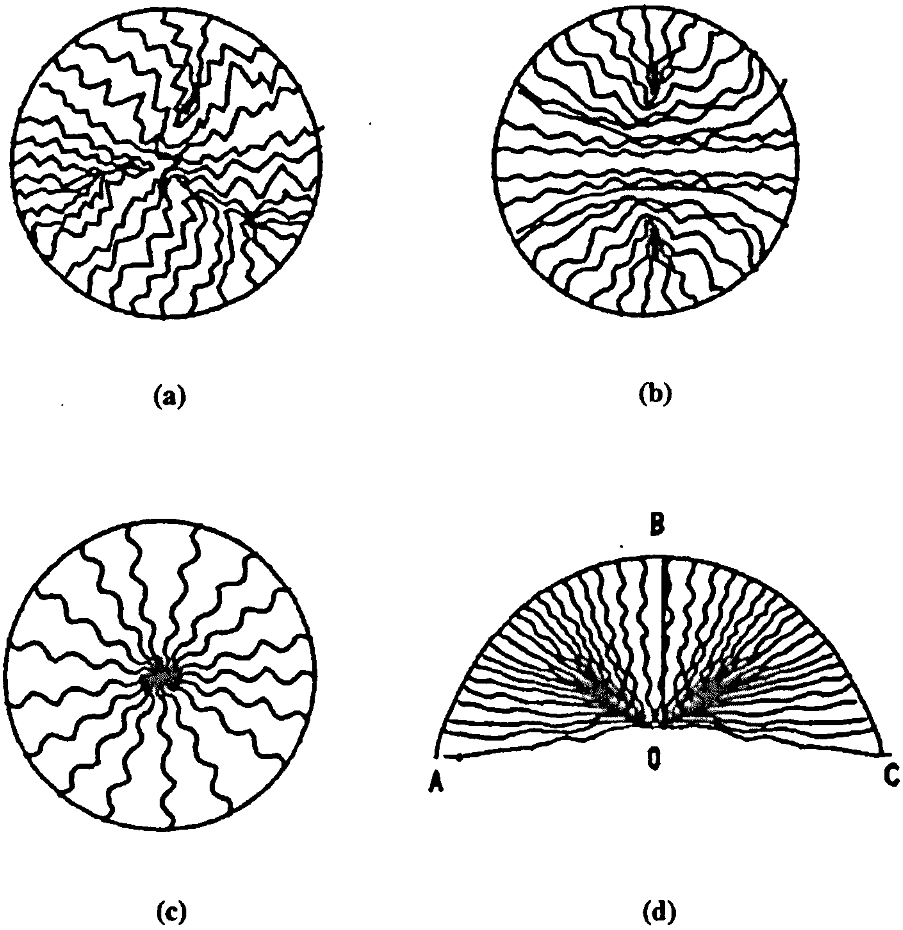

(a) (b) (c) (d)

Figures 3-2. Schematic diagrams of the domain structure for (a) irregular radial type, (b) radial-ribbon type, (c) regular radial type, and (d) missing sector radial type.

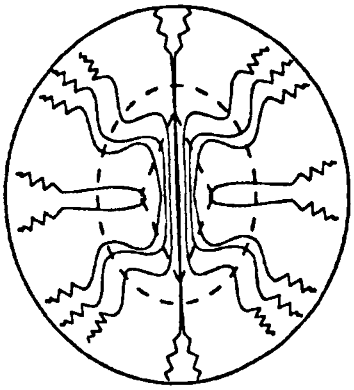

Figure 3-3. Schematic diagram showing the three-zoned texture observed in SEM fracture surfaces of E35~E130 fibres [44].

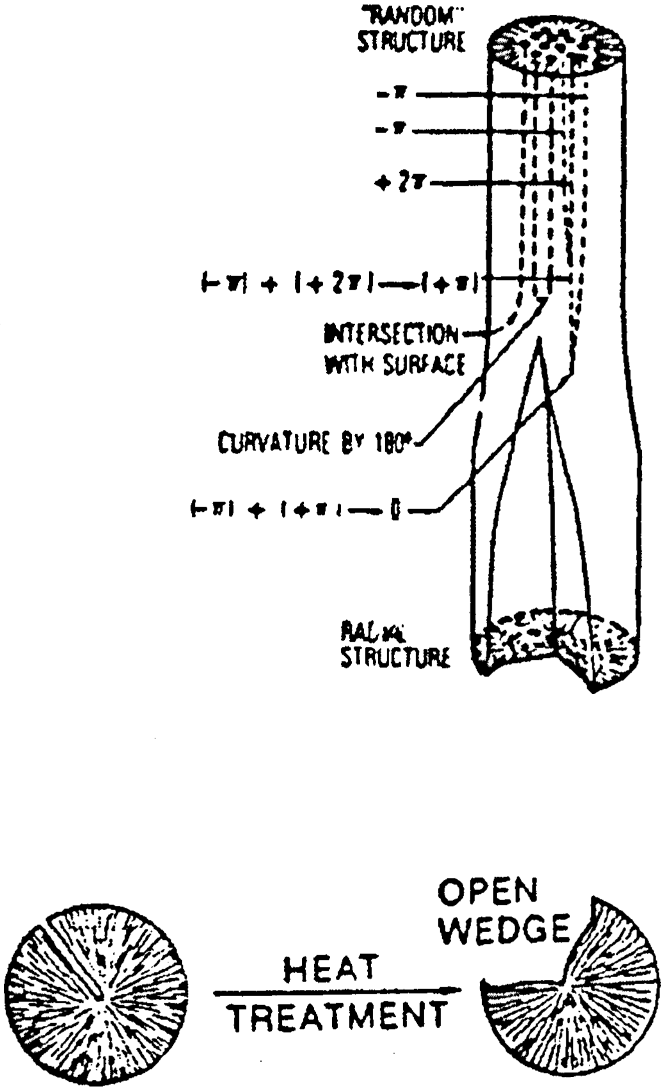

Figure 3-4. Schematic diagram showing the formation of a missing-sector structure from a radial crack [20].

3. 2. Microstructure of MP-based carbon fibres

3. 2. 1. TEM studies

3. 2. 1. 1. Dark-field images

002 dark-field images from longitudinal sections of all fibres studied are shown in Figures 3-5a to 3-5h. The diffracting crystallites are seen as white regions on a dark background. Since the contrast in dark-field image is high, all crystallites can be readily detected and measured (see Chapter 4).

In all specimens, except for the fibre E35C, the crystallites appear to be of a columnar form oriented roughly parallel to the fibre axis and separated by irregular spaces. Apart from fibre C700 the crystallite columns appear to split and sometimes interlink with adjacent columns. In the case of the C700 fibre, however, the crystallite columns appear to be isolated.

Clearly there is a distribution of crystallite thickness or stacking size L_c, which is reported and discussed later in Chapter 4. The length of the crystallite columns of all carbon fibres studied (except for the fibre E35C) is extremely long, at least 1.6 μm.

It is very interesting to note that fibre E35C exhibits an unusual structure. As shown in Figure 3-5a, the crystallites appear as discontinuous arrays of "extended droplets" oriented along the fibre axis and of limited length of approximately 200 *nm*. There are two possible explanations accounting for the apparent discontinuity. One possibility is that the actual radial layers are continuous but are considerably folded about the fibre axis. Thus a longitudinal section through such a folded layer will therefore appear to be discontinuous with the length of each segment being dependent on the folding frequency. As a result the crystallites appear to be discontinuous rather than extended columns along the fibre axis. Another possibility is that the actual radial layers are indeed discontinuous along the fibre axis although in terms of the physical properties this is most unlikely. It should be noted that continuous columnar crystallites are occasionally observed interspersed with the discontinuous "droplets".

3. 2. 1. 2. Lattice-fringe images

Lattice-fringe images from longitudinal sections are shown in Figures 3-6 to 3-13 for the whole series of carbon fibres. Typically two phases are evident in every fibre. One phase (ordered phase) consists of extensive arrays of lattice fringes and the other phase is devoid of fringes or contains very few small arrays of fringes and appears to be generally disordered.

As shown in Figure 3-6, the lattice fringes in fibre E35C are short ranged and have a variable orientation. In addition the arrays of lattice fringes have an irregular profile and a large length to width ratio.

Fibre E35 exhibits extensive but wavelike lattice fringes in the ordered phase as shown in Figure 3-7. The general orientation of the fringes is roughly parallel to the fibre axis but locally variable. In the other phase, very few lattice fringes are visible and their lateral extent rarely exceeds 2 *nm*.

The ordered phase in E55 fibres appears to be of two types as shown in Figure 3-8. One type appears to consist of columnar crystallites filled with the lattice fringes of longer range than in fibre E35. The orientation is generally better although some meandering of the fringes can still be seen. The second type contains small areas of lattice fringes together with other regions of apparent disorder.

The lattice fringes in E75 fibres (Figure 3-9) appear to be very similar to those in E55 fibre, however the layer planes are better oriented and the crystallite regions are more perfectly formed.

The ordered phase of fibre E105 consists of long range and well oriented fringes as shown in Figure 3-10. The layer plane aggregation is laterally extensive. In some regions the crystallites appear to fork and interlink with adjacent crystallites. In other regions small blocks of fringes appear to curve through 90^0 and the layer planes are misoriented and interlinked.

As shown in Figure 3-11, the lattice fringes of the E120 fibre are ordered over long range but sometimes branch and interlink with adjacent crystallites. It is interesting to note that in some regions the layer planes appear to finish abruptly and then reappear some distance away along the fibre axis. This is probably due to phase changes in the formation of the lattice image.

Fibres E130 and C700 (Figure 3-12 and 3-13) both exhibit the columnar profile of the ordered phase. The lattice fringes are almost perfectly aligned over large distances.

It is clear that the degree of meander of lattice fringes decreases from fibre E35C to fibre C700, which indicates that generally the lattice perfection and layer orientation increase. These two parameters have been determined and are discussed later in Chapter 4.

It is important to note that the absence of lattice fringes in a region of a micrograph may be due to lattice planes not being at the Bragg condition for diffraction. Thus the absence of fringes does not necessarily imply the presence of a disordered region .

E35C

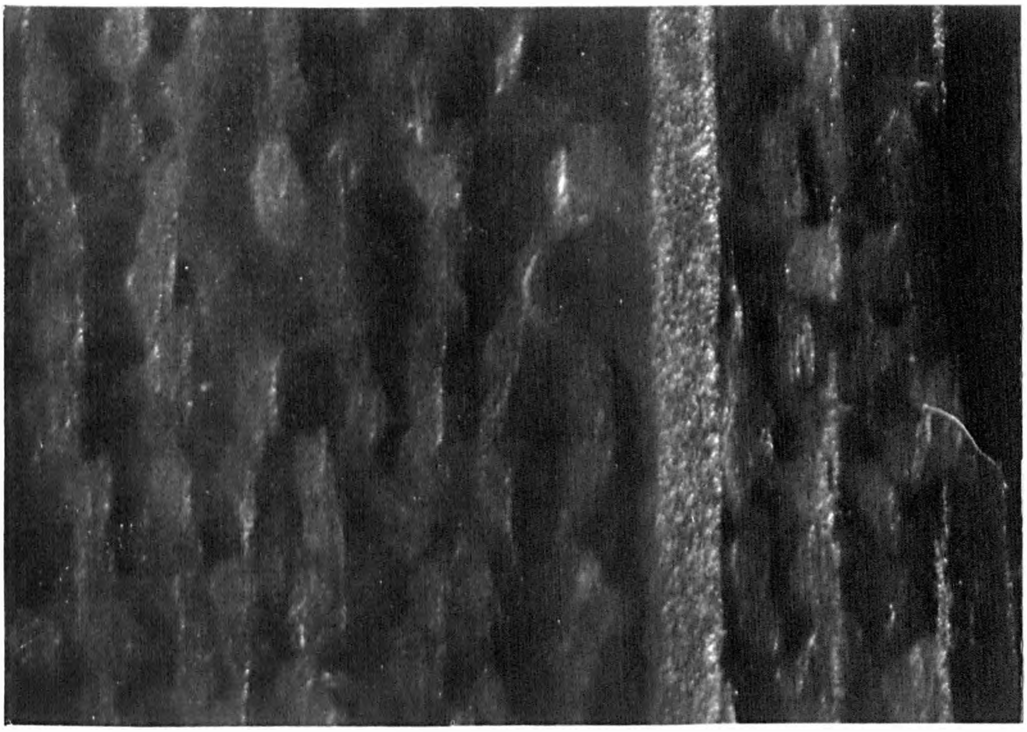

E35

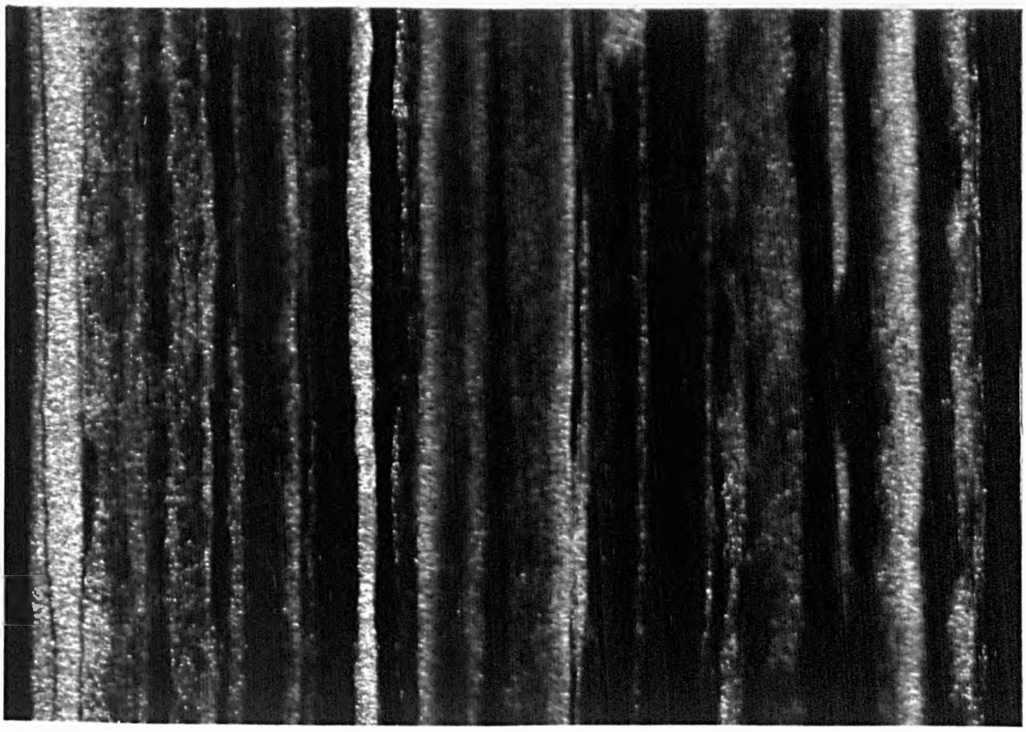

Figures 3-5. TEM (002) dark-field images from longitudinal sections of MP-based carbon fibres : E35C, E35, E55, E75, E105, E120, E130, and C700

E55

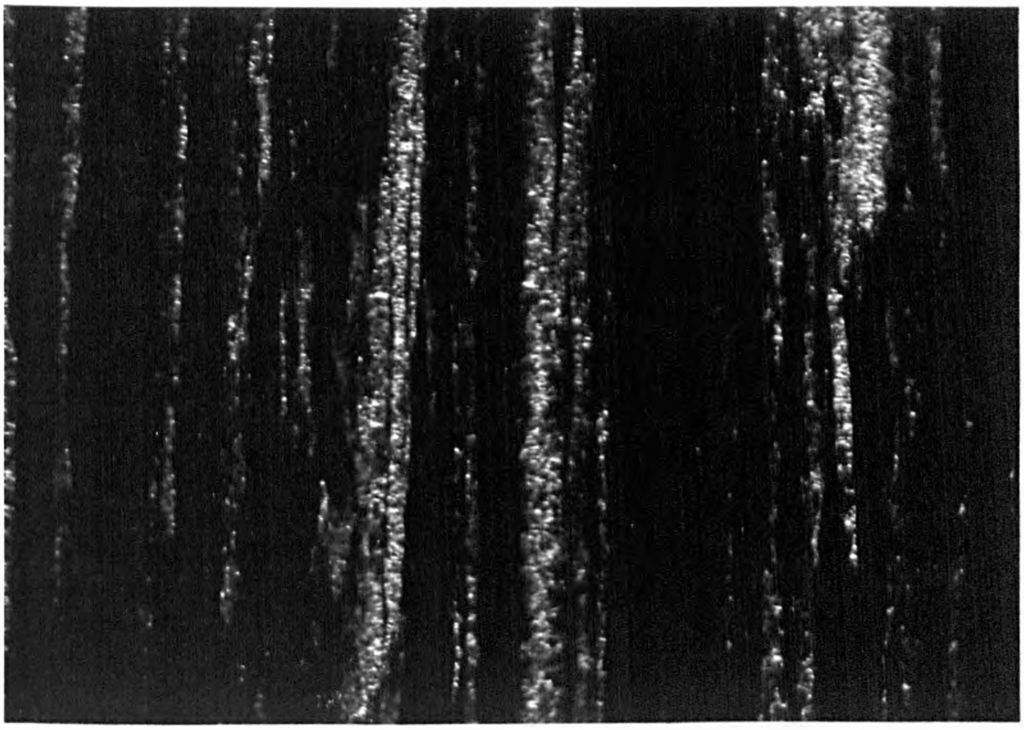

E75

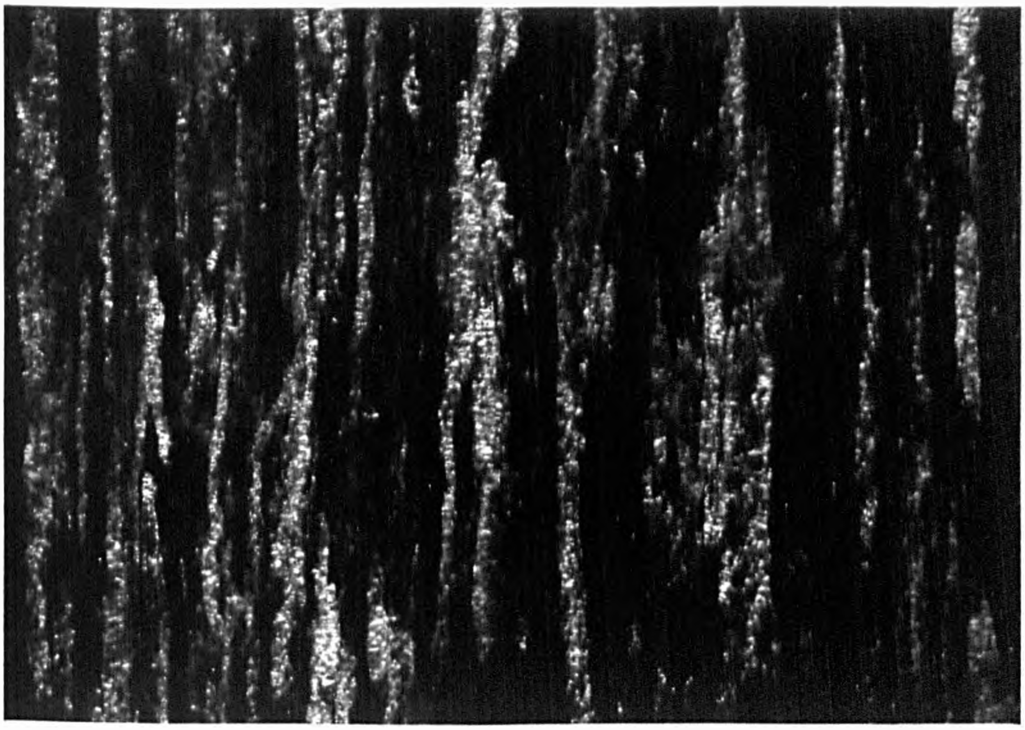

Figures 3-5. TEM (002) dark-field images from longitudinal sections of MP-based carbon fibres : E35C, E35, E55, E75, E105, E120, E130, and C700

E105

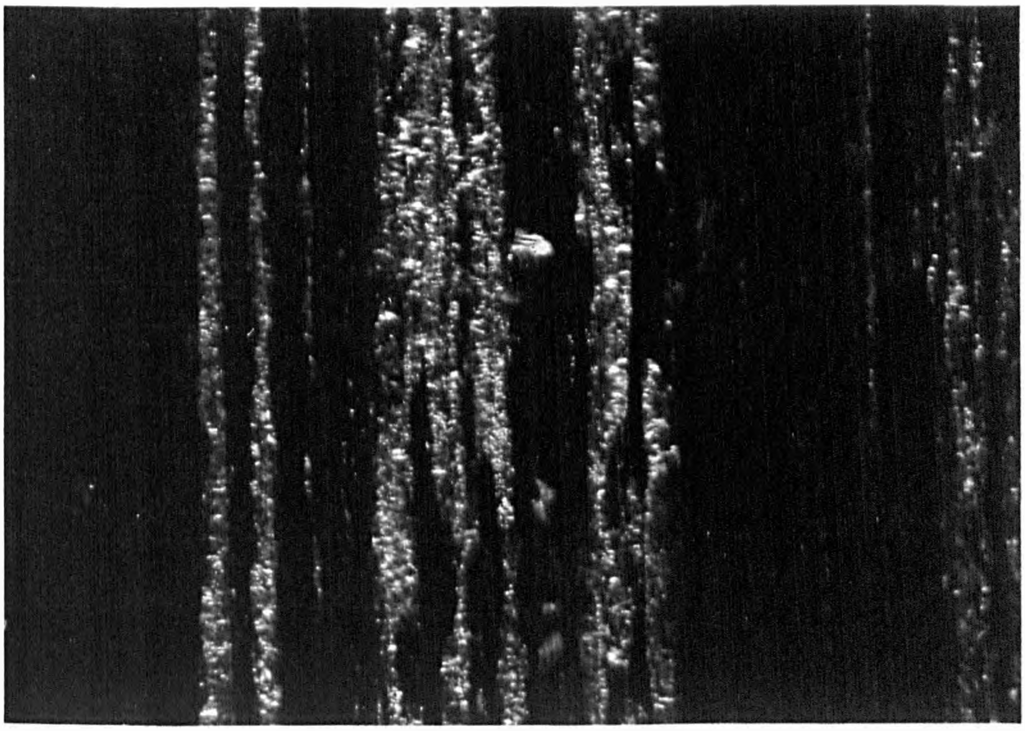

E120

Figures 3-5. TEM (002) dark-field images from longitudinal sections of MP-based carbon fibres : E35C, E35, E55, E75, E105, E120, E130, and C700

E130

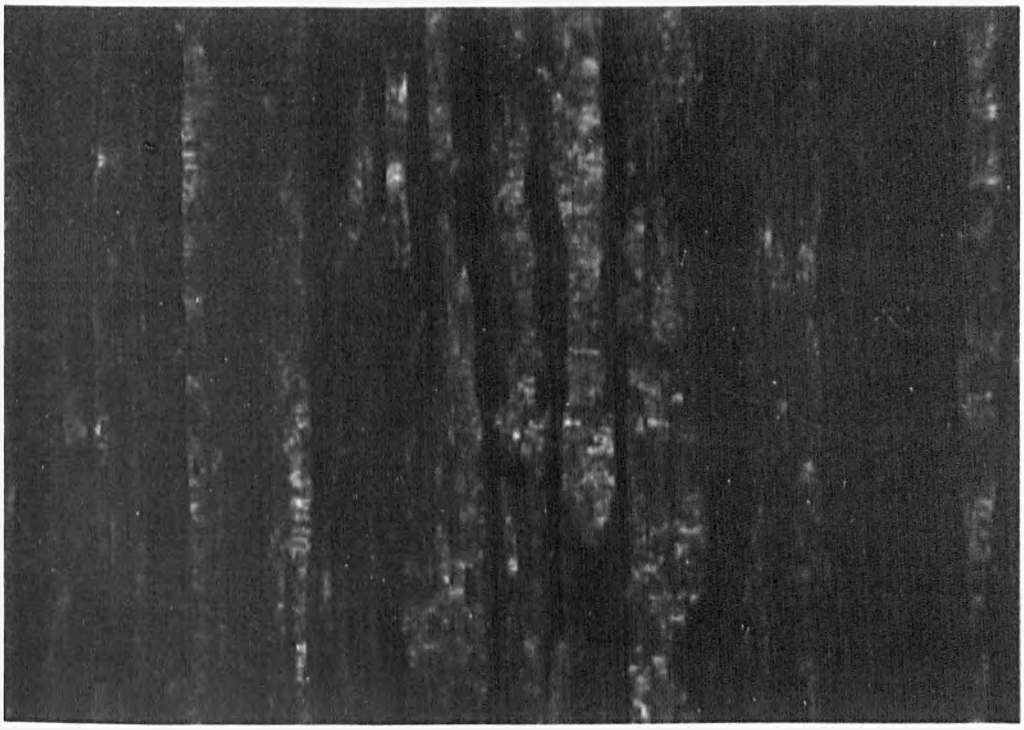

C700

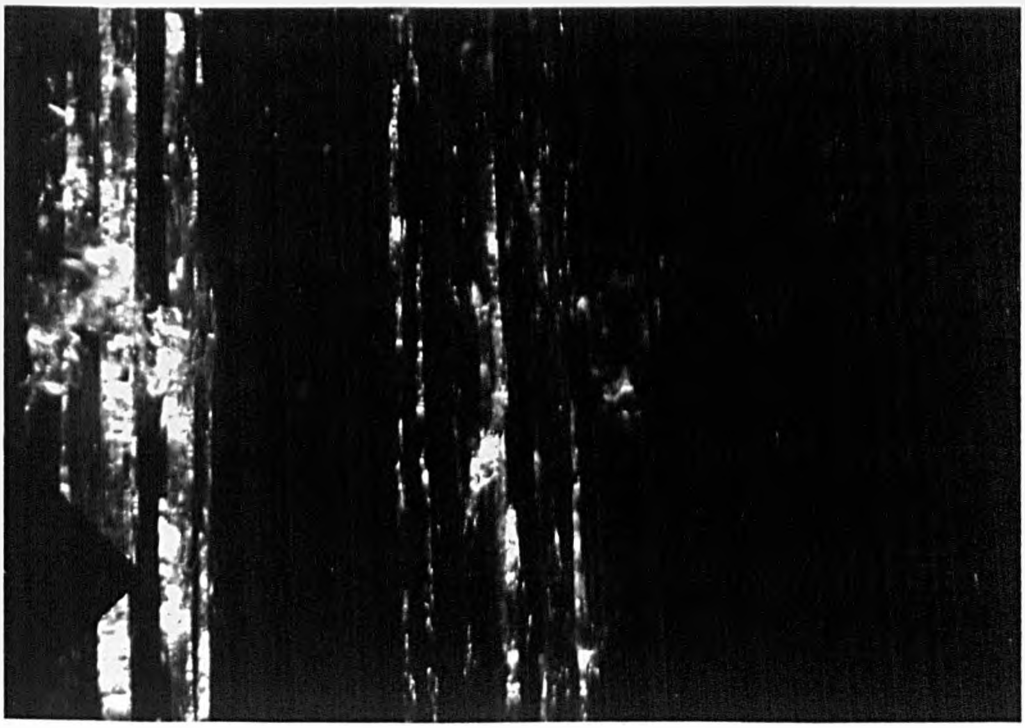

Figures 3-5. TEM (002) dark-field images from longitudinal sections of MP-based carbon fibres : E35C, E35, E55, E75, E105, E120, E130, and C700.

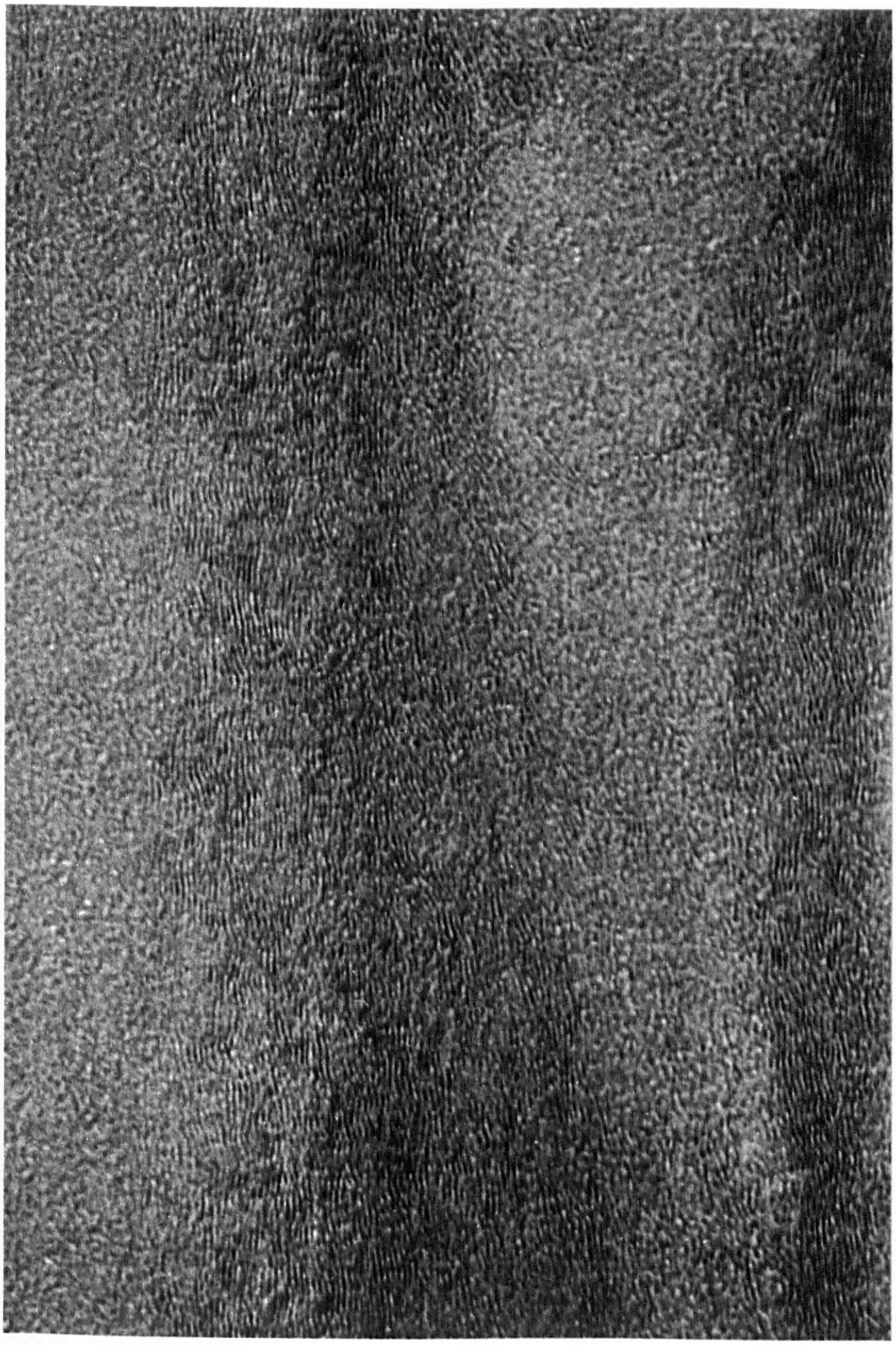

Figure 3-6. A (002) lattice-fringe image from a longitudinal section of E35C fibre.

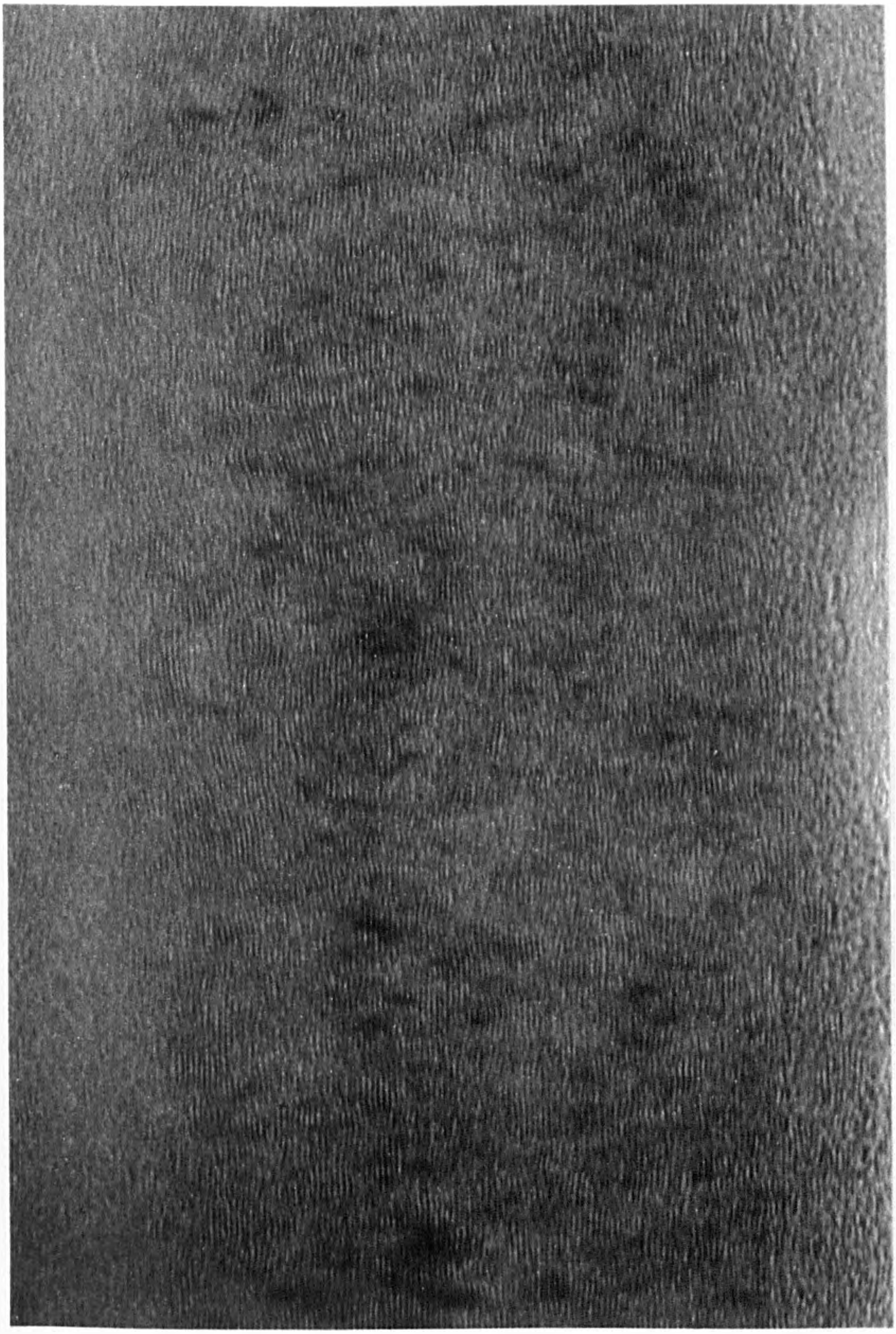

Figure 3-7. A (002) lattice-fringe image from a longitudinal section of E35 fibre.

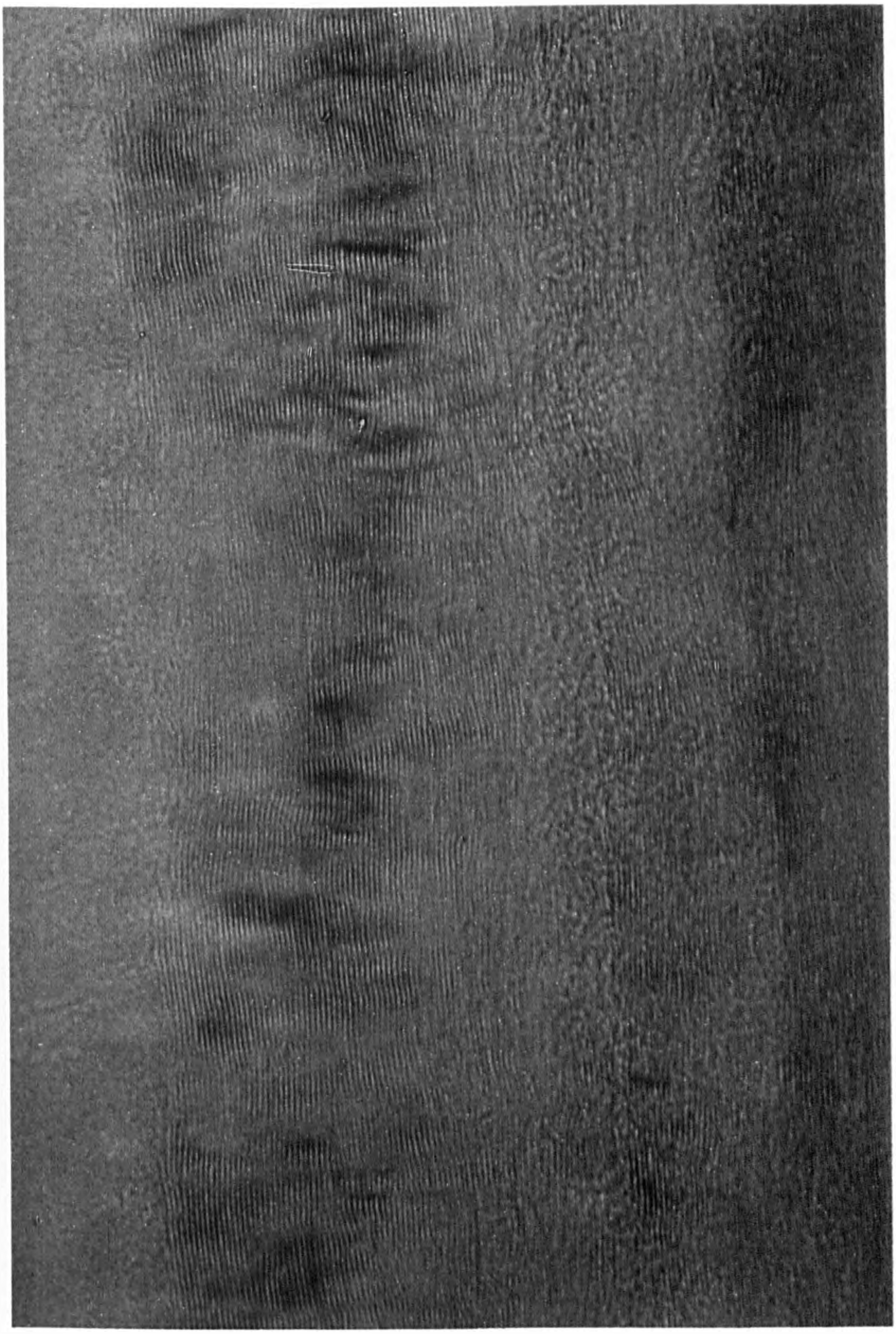

Figure 3-8. A (002) lattice-fringe image from a longitudinal section of E55 fibre.

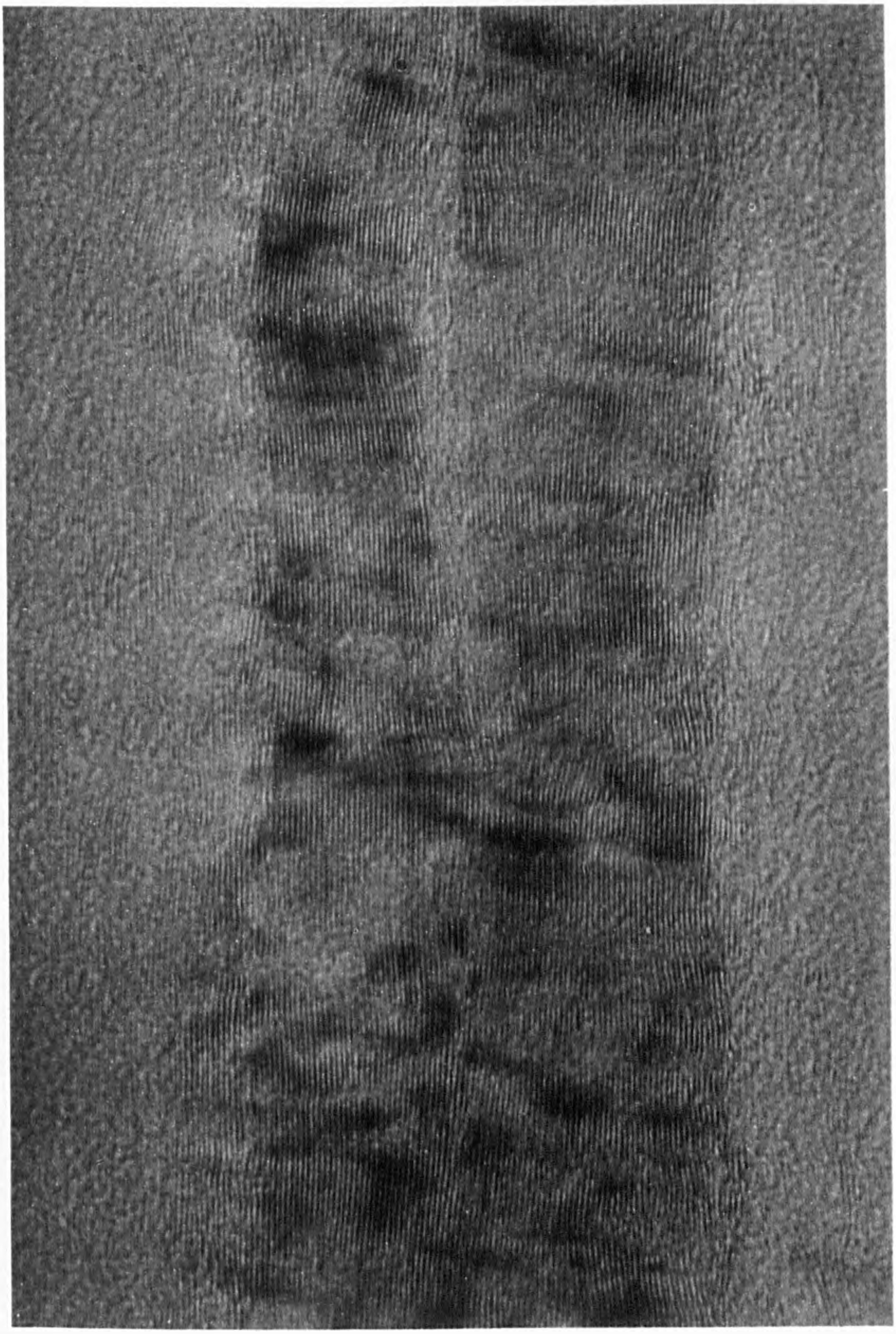

Figure 3-9. A (002) lattice-fringe image from a longitudinal section of E75 fibre.

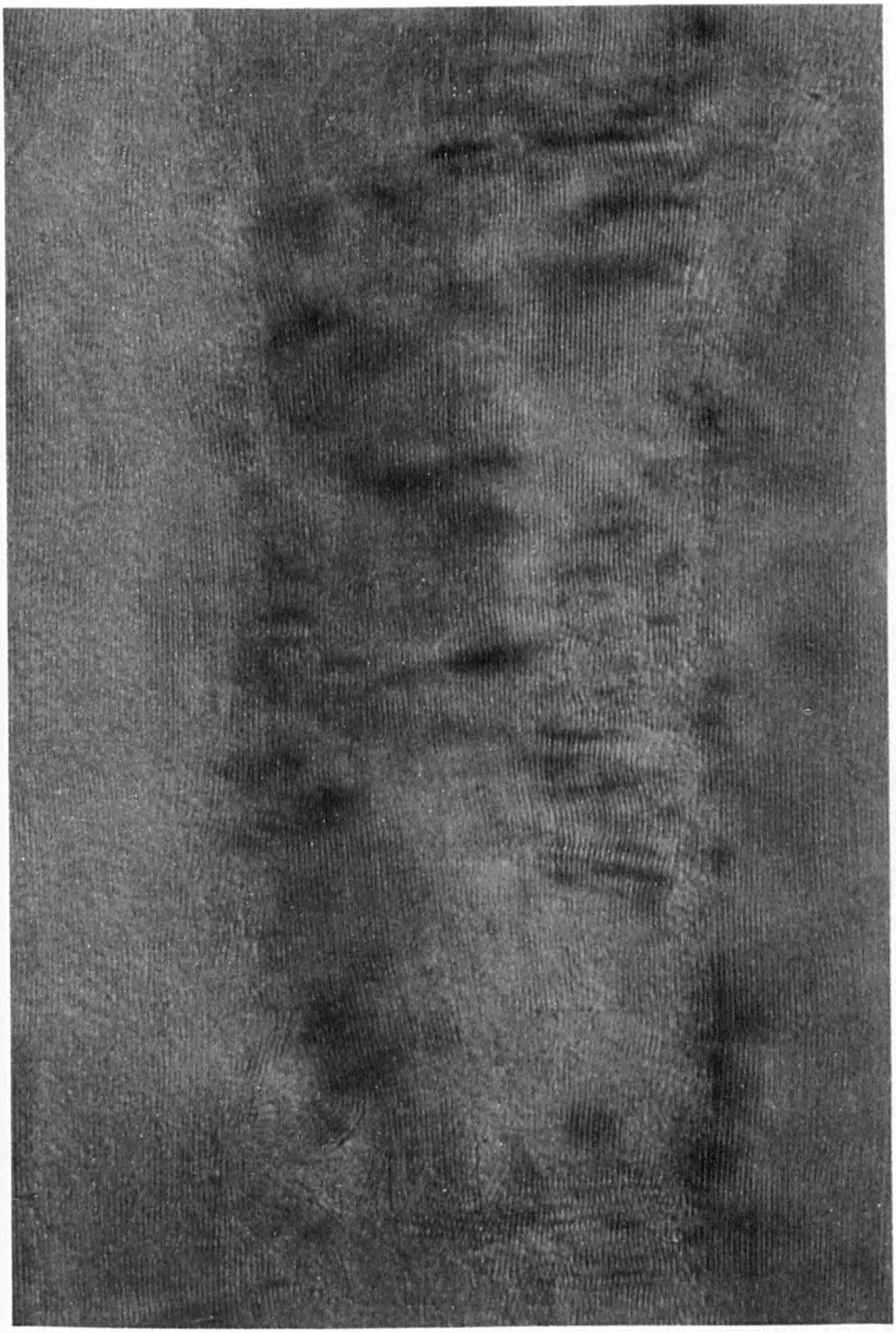

Figure 3-10. A (002) lattice-fringe image from a longitudinal section of E105 fibre.

Figure 3-11. A (002) lattice-fringe image from a longitudinal section of E120 fibre.

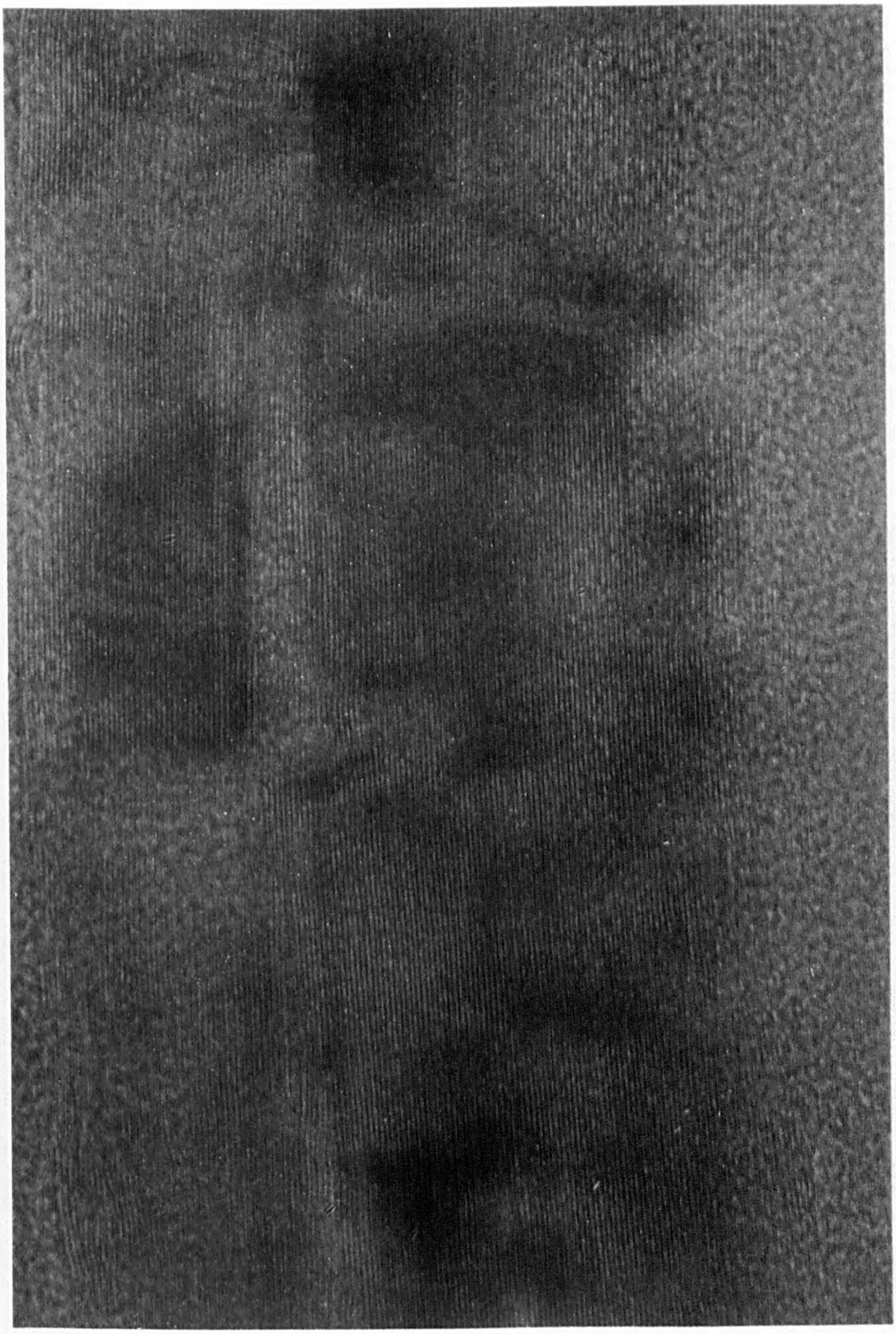

Figure 3-12. A (002) lattice-fringe image from a longitudinal section of E130 fibre.

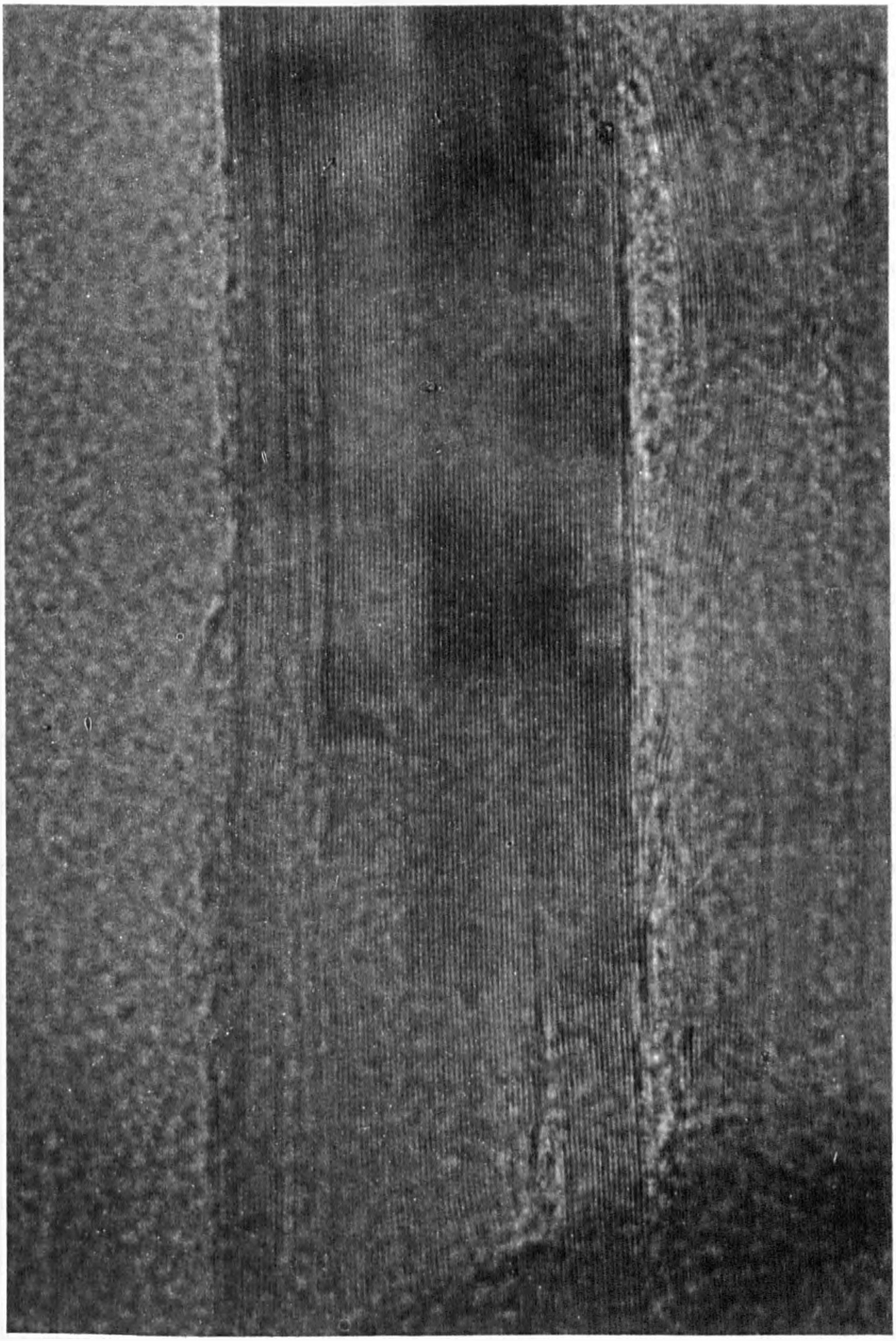

Figure 3-13. A (002) lattice-fringe image from a longitudinal section of C700 fibre.

3. 2. 1. 3. Selected area electron diffraction

Selected area electron diffraction patterns from longitudinal sections of all fibres studied are shown in Figures 3-14a to 3-14h. All MP-based carbon fibres exhibit diffraction patterns with strong 002 reflections and the 100 and 110 rings which are more intense on the meridian. Weak 004 reflections are also evident on the equator for every fibre except fibre E35C.

However, there are differences between the patterns from different fibres. For example, the intensity of the 00*l* reflections becomes progressively stronger and sharper and the degree of arcing becomes smaller in the order of E35C, E35, E55, E75, E105, E120, E130 and C700 fibre. This suggests that the orientation improves and the crystallite size of the layer plane increases.

Another difference in this series of SAD patterns is that for the fibres E105, E120, E130 and C700 there is a tangential streak on the meridian of 100 and 101 reflections. This probably arises from improved preferential orientation of the layer planes with respect to each other [25]. The intensity of the streaks is particularly strong in Figures 3-14g and 3-14h. Consequently, it is thought that the fibres E130 and C700 have a high degree of graphite-like order.

Closer inspection of patterns obtained from the fibres E130 and C700 shows additional features : (a) the 100 and 110 rings are discontinuous (spot-like) unlike those exhibited by the other fibres, and (b) the 112 reflection also appears, which is a characteristic of three-dimensionally ordered graphite. The intensity of the 112 reflection of fibre C700 is much stronger than that of the fibre E130. These two features support the evidence that fibres C700 and E130, which have a very high modulus, are highly graphitic.

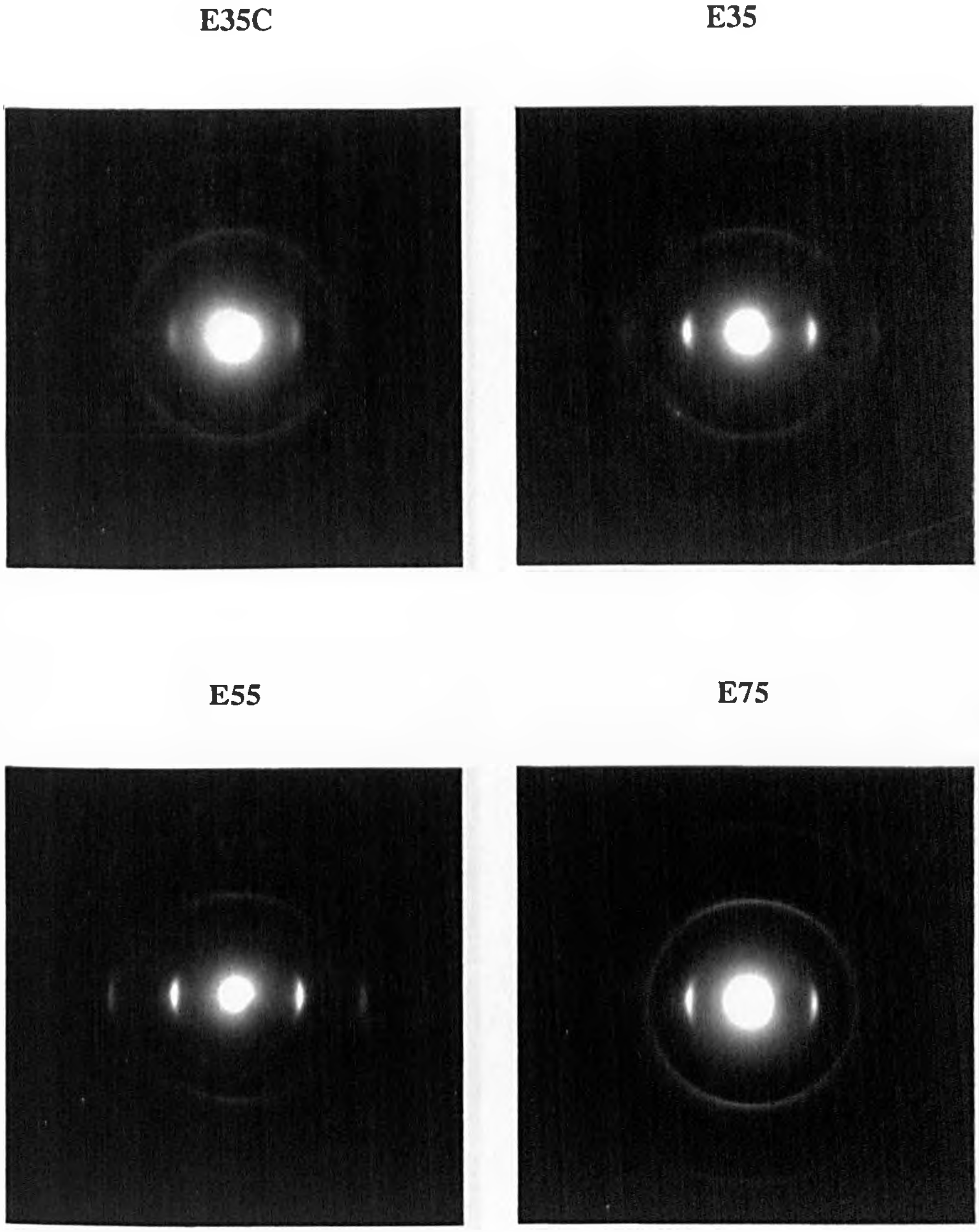

E35C

E35

E55

E75

Figures 3-14. Electron diffraction patterns from longitudinal sections of MP-based carbon fibres : E35C, E35, E55, E75, E105, E120, E130, and C700

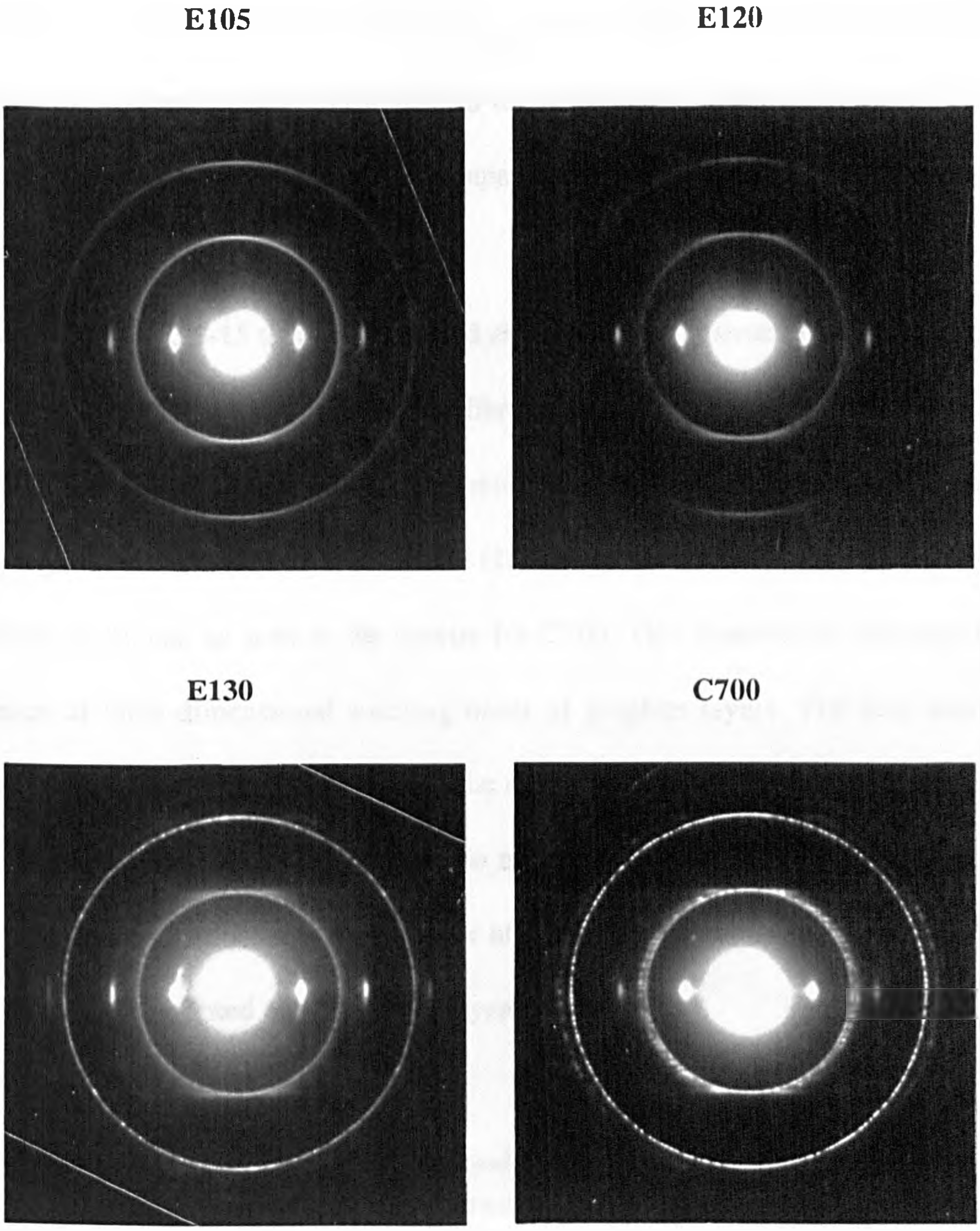

E105

E120

E130

C700

Figures 3-14. Electron diffraction patterns from longitudinal sections of MP-based carbon fibres : E35C, E35, E55, E75, E105, E120, E130, and C700

3. 2. 2. X-ray diffraction studies

Figure 3-15 shows the equatorial X-ray scans of the series of MP-based carbon fibres and Table 3-1 gives the interlayer spacing d_{002} and the apparent crystallite thickness L_c obtained from these spectra. Orientation measurements derived from the X-ray diffraction patterns are discussed and compared with those obtained by other techniques in Chapter 4.

As shown in Figure 3-15 there is a marked change in crystal structure from the least ordered fibre (E35C) to the highly ordered fibre (C700). Sharpening of the $(00l)$, (100) and (110) are clearly seen indicative of increasing order. The separation of diffraction scattering into the two reflection (100) and (101), together with the appearance of the reflection (112), can be seen in the spectra for C700. This observation indicates the existence of three-dimensional stacking order of graphite layers. The four sets of crystallographic layer planes from which the reflections arise are illustrated in Figure 3-16. On the other hand, all other fibres do not exhibit such resolution into separate (100) and (101) reflections, nor the presence of the (112) reflection which suggests that these fibres are composed of turbostratic layered structures.

Table 3-1. The interlayer spacing d_{002} and the apparent crystallite thickness L_c determined from X-ray diffraction on MP-based carbon fibres

	E35C	E35	E55	E75	E105	E120	E130	C700
d_{002} (*nm*)	0.3455	0.3421	0.3418	0.3417	0.3399	0.3396	0.3376	0.3360
L_c (*nm*)	3.2	3.7	8.5	12.0	16.8	19.2	23.8	27.9

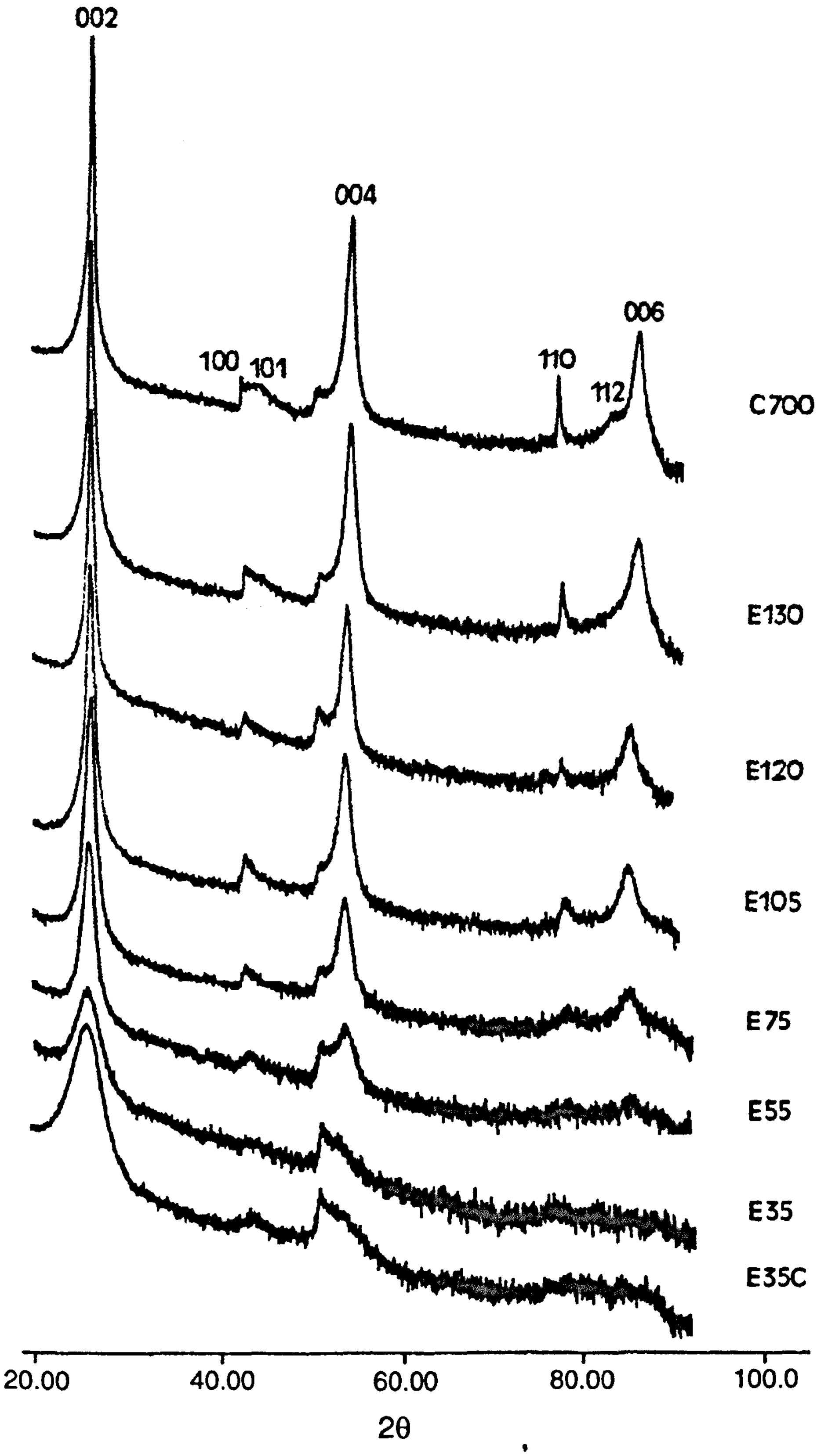

Figure 3-15. The equatorial X-ray scans of MP-based carbon fibres

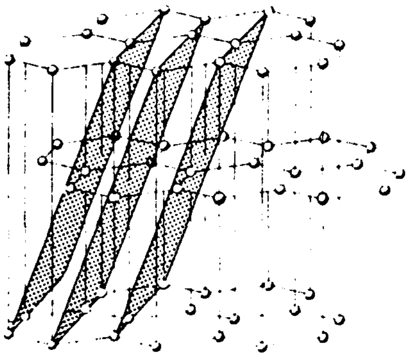

Tilted (112) planes indicative of 3 dimensional ordering
d = .1155 nm

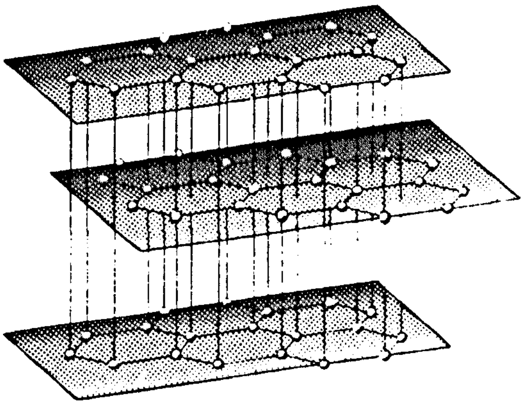

(002) layer planes
d = .3345 nm

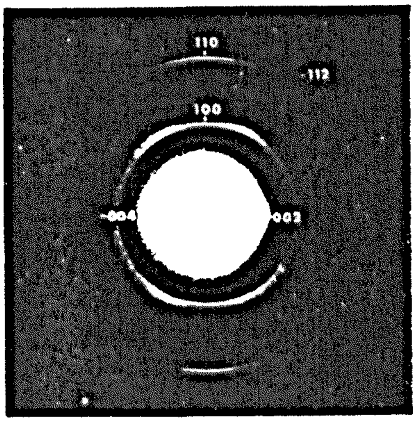

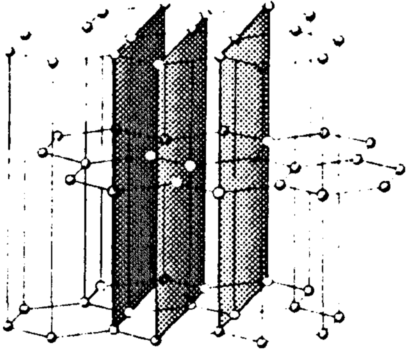

(110) planes
d = .1232 nm

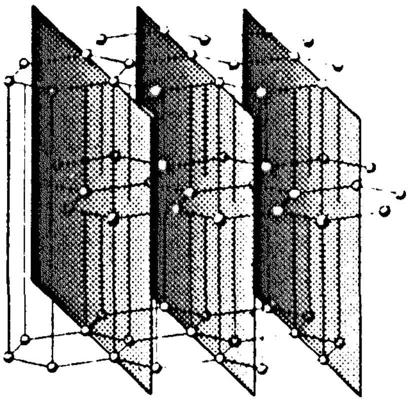

(100) planes
d = .2132 nm

Figure 3-16. Crystallographic planes in graphite [87]

The interlayer spacing d_{002} is very sensitive to lattice imperfections, and variations in interlayer spacing can be correlated with the degree of lattice perfection. Detailed discussion can be found in Chapter 4. From Table 3-1 it can be seen that the interlayer spacing d_{002} increases from fibre C700 (0.3360 *nm*) to E35C (0.3455 *nm*), which indicates that the degree of graphitization decreases.

It is also clear that the apparent crystallite thickness increases considerably from the least ordered fibre E35C to the highly ordered fibre C700. The significant differences between the crystallite thicknesses estimated from X-ray scans and measured from dark-field images are discussed in Chapter 4.

3. 3. General discussion of structure

The SEM studies show that this series of MP-based carbon fibres all exhibit folded pseudo-radial layers although the fibres E35C and C700 have a missing sector structure. Generally, as modulus increases (i.e. the degree of graphitization increases) there is a tendency to form a single domain of uniformly folded radial layers.

Each fibre, except for the fibre E35C, appears to consist of aggregates of transversely folded lamellae aligned approximately parallel to the fibre axis. This is in agreement with Endo's folded layer structure model (see Figure 1-11). In fibre E35C, however, the possibility of further folding about the fibre axis cannot be excluded depending on the interpretation of the distinctive dark-field images (see Figure 3-17b).

TEM and X-ray studies indicate that the degree of crystallite layer perfection increases from fibre E35C to C700. Indeed, electron diffraction patterns and X-ray scans reveal that the intensity of 00*l*, 100 and 110 reflections become progressively stronger.

Furthermore, high resolution TEM images show that the degree of meander of lattice fringes become progressively less in the series of E35C to C700.

It was found that fibres E130 and C700 have a high degree of three-dimensional order since these two fibres exhibit diffraction patterns with the discrete 100 and 110 rings and the appearance of the 112 ring. In addition, the layer planes as deduced from lattice-fringe images are almost perfect over large distances. However, it is noted that the 112 reflection can not be seen in the X-ray spectra of fibre E130 (Figure 3-15). This suggests that compared with C700, fibre E130 is slightly less ordered. Actually, the interlayer spacing of E130 is slightly larger than that of C700 as shown in table 3-1, which also implies a relatively lower packing-perfection.

It is clear that as the graphitization proceeds from E35C to C700, there is a tendency to develop a three-phase microstructure (consisting of graphitic, turbostratic and disordered components) from an original two-phase microstructure (turbostratic and disordered components only). This finding is consistent with Oberlin's suggestion [37] and Park's observation [72] on other MP-based carbon fibres.

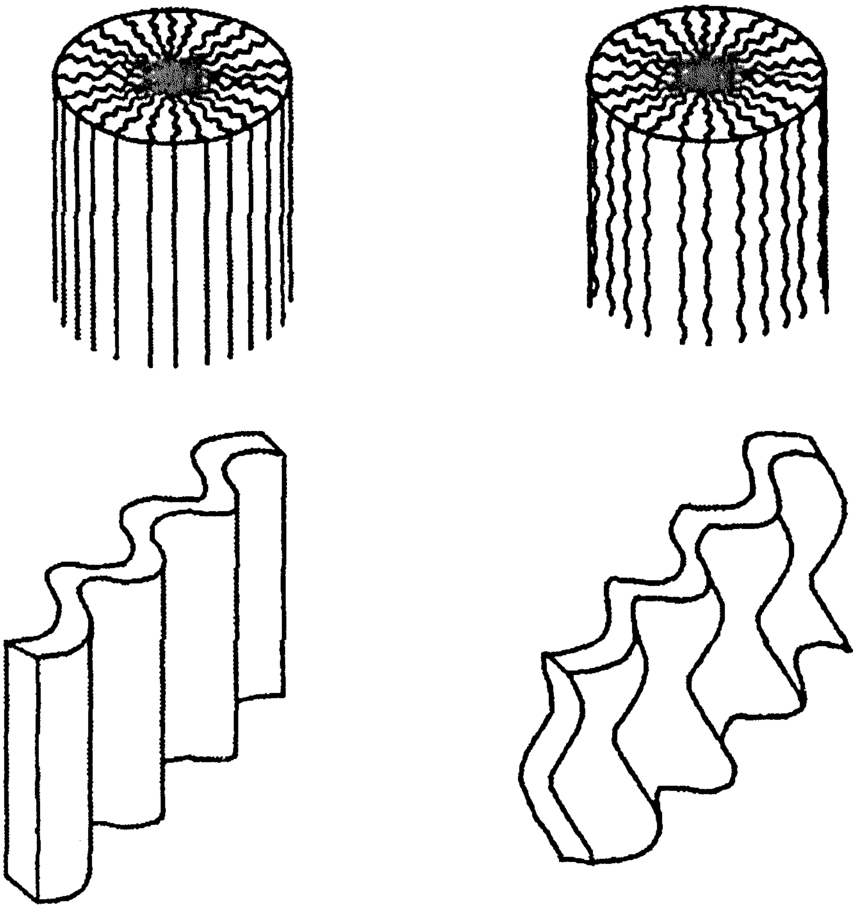

(a) (b)

Figure 3-17. Schematic diagrams showing two distinctive folded layer structures.

Chapter 4

Image Analysis of the Microstructure in Carbon Fibres

4. 1. Layer stacking size in carbon fibres

4. 1. 1. Stacking size and X-ray measurement

Generally the crystallite sizes represent the apparent average dimensions of the crystallite domains parallel (L_a) and perpendicular (L_c) to the layer planes. L_a is further subdivided into $L_{a/\!/}$ and $L_{a\perp}$ which respectively give the apparent layer dimensions parallel and perpendicular to the fibre axis. Since the presence of crystallites of finite size will broaden the X-ray diffraction peaks in the same direction [88], in principle the crystallite dimensions can be determined from the profile of one diffraction peak.

The crystallite thickness L_c (stacking size) of carbon fibre is determined from the breadth of the 002 reflection. This is achieved by using the well known Scherrer equation: $L_c = K\lambda \ / \ B_{002}\cos\theta$, where λ is the X-ray wavelength and θ is the Bragg angle. The Scherrer parameter K can be considered as the factor by which the apparent size must be multiplied in order to determine the true size [89]. For $00l$ reflections K is usually given a value of 0.89 and 1 when B_{002} corresponds to the half-height width and integral breadth respectively [78].

The crystallite dimension L_a is generally estimated from the X-ray line broadening of the 100 reflection. The meridional width of the 100 reflection, B_{100}, is used to obtain the layer-plane length parallel to the fibre axis $L_{a/\!/}$; while the equatorial width is used to obtain the crystallite width perpendicular to the fibre axis $L_{a\perp}$. However, the Scherrer parameter K should be adjusted to 1.77 [90] or 2.0 [91] in both $L_{a/\!/}$ and $L_{a\perp}$ determinations.

In practice it is necessary to correct the experimental intensity profile for specimen absorption, Lorentz, polarization, air scattering and Compton scattering factors as explained in Chapter 2. Moreover the broadening of the diffraction peak depends not only on crystallite size but also on structural imperfections (such as internal strain, layer plane orientation) and instrumental broadening etc., which should be taken into consideration in order to obtain an accurate measurement of the crystallite sizes [92].

Several workers [24,93,94,95] have reported that the crystallite sizes in carbon fibre increase rapidly with increased heat-treatment temperature. Dresselhaus *et al.* [22], after analysing results obtained by other workers, plotted values for L_a and L_c (from X-ray diffraction measurements of PAN-based carbon fibres) against heat-treatment temperature T_{HT} as shown in Figure 4-1. A general monotonic increase in crystallite sizes occurs with increased T_{HT}. However, the increase is smaller with heat-treatment temperatures below 1500^0 *C*. For mesophase pitch-based carbon fibres, it was reported that the crystallite thickness L_c shows a rapid increase in the range of 1000 to 2500^0 *C* [19]. Also it was observed that the fibres characterized by a radial-folded structure tend

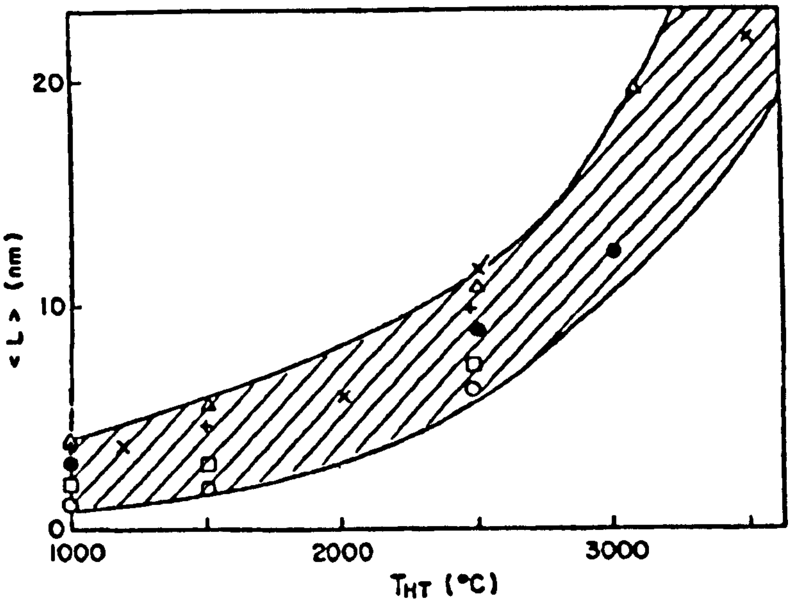

Figure 4-1. Increase of average crystallite size with increasing T_{HT} for various carbon fibres: (o) L_c [35]; (+) $L_{a//}$ [35]; (☐) $L_{a\perp}$ [35]; (Δ) L_a [37]; (x) L_c [38].

to have a higher value of L_c than those exhibiting a random structure, although the differences were insignificant below 1700^0 C.

Crystallite sizes are also influenced by other factors such as the degree of precursor fibre stretching and orientation of layer planes. It was reported that high-temperature stretching can considerably increase the apparent stacking size L_c for pitch-based [96], PAN-based [97] and rayon-based [98] carbon fibres. Perret and Ruland [99] observed that high degrees of preferred orientation of the layer planes tend to be associated with large values of the stacking size L_c. For PAN-based fibres, an important finding is that after boron doping of the sample, the stacking size L_c increased from 5.7 to 8.6 *nm* and the crystallite dimension L_a increased form 4.6 to 8.9 *nm* [100]. Finally it should be borne in mind that crystallite sizes vary depending on the precursor materials, and usually carbon fibres derived from mesophase pitch have larger values than PAN- or rayon-based fibres.

In the present work the results of the stacking sizes L_c found for the range of MP-based carbon fibres (using X-ray methods) are reported in Table 4-1.

4. 1. 2. Measurement of stacking size from TEM dark-field images

As described in Chapter 3, the diffracting crystallites as observed in dark-field images appear as bright regions on a dark background and occur in columnar form oriented roughly parallel to the fibres axis. Hence by measuring the thickness distributions of the bright regions, the average stacking size L_c can be directly determined.

Dark-field images from longitudinal sections of the series of carbon fibres were examined in the Quantimet 570 image analyser and processed according to the flow chart shown in Figure 2-6. For a meaningful thickness measurement the two edges of each bright column must be accurately detected before the measurement procedure. In order to facilitate this, a Sobel gradient transform was used to delineate the edges (the original grey level value of each pixel is replaced by a value proportional to the difference between the pixel and its neighbours). In the gradient image so obtained the edges appear bright. This processed image was then superposed on the original grey image using the ADD. function. The resultant image then showed well defined columnar structures.

Since the thickness of the columns varies considerably along the fibre axis, equally spaced horizontal black grid lines were superimposed on the images. The white segments of the columnar structures were then detected and transferred into a binary image. By measuring the distribution of horizontal projections of the bright segments, estimates of the average stacking sizes were made.

4. 1. 3. Results and discussion

The distributions of stacking sizes obtained from dark-field images for a series of carbon fibres are shown in Figure 4-2. It is clear that in all case there is a wide distribution of sizes ranging from approximately 5~100 *nm* with peak values around 20 *nm*. Inspection of micrographs reveals variations in stacking size both along and between the columnar aggregates. Such information is not available from X-ray studies which reveal only mean values of stacking size.

Table 4-1 gives the average stacking size L_c and L_c* obtained respectively from X-ray diffraction and (002) dark-field images, together with the ratio L_c/L_c* between them.

It is clear that the stacking size L_c (X-ray) increases significantly from fibre E35C to C700. Moreover apart from fibre C700, which has similar values of L_c and L_c*, all fibres have a higher value of stacking size L_c* than L_c, and the difference between values gets progressively less with increasing graphitization. This apparent anomaly can be reconciled as follows.

It is apparent that individual columns, as seen in the dark-field images (see Figure 3-5), consist of smaller separate areas of highly diffracting material (i.e. crystallites). In other words the columns cannot be considered as single crystallites except possibly in the case of C700. The different intensity scattering within each column may be due to either (a) changes in azimuthal orientation (diffracting away from the Bragg angle) or (b) resulting from structural disorder or imperfections within the column.

It is clear, however, that the discrepancy between L_c and L_c* decreases from the fibre E35C to the fibre C700 and this effect probably arises from increased annealing effects within the columnar aggregates leading to a larger stacking size. Thus X-ray values (L_c) arise from single crystallites whereas dark-field values (L_c*) are associated with aggregates of individual crystallites. Therefore in the case of high modulus fibres the crystallite stacking size L_c* is very close to crystallite size L_c whereas in the case of low modulus fibres it is much larger than L_c as shown in Table 4-1.

Table 4-1. Stacking size determined from X-ray diffraction and dark-field images

Fibres	***Lc (nm)***	***Lc* (nm)***	***Lc/Lc* (%)***
E35C	3.2	31.4	10.0
E35	3.7	32.2	11.5
E55	8.5	30.8	27.5
E75	12.0	32.9	38.8
E105	16.8	29.6	56.8
E120	19.2	29.6	54.9
E130	23.8	40.0	59.5
C700	27.9	27.7	100.7

E35C

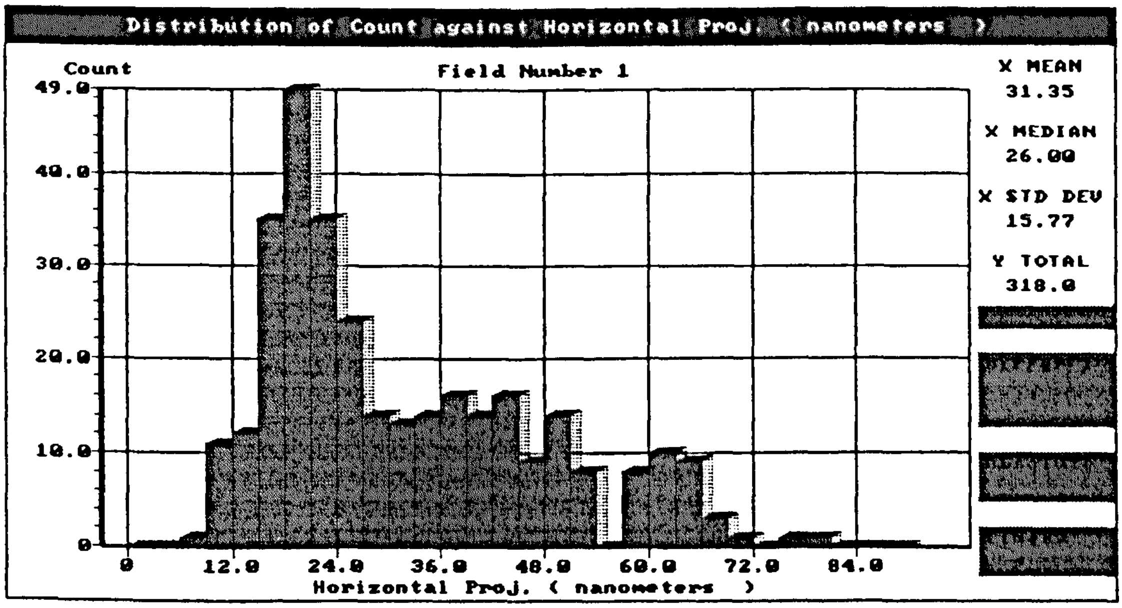

E35

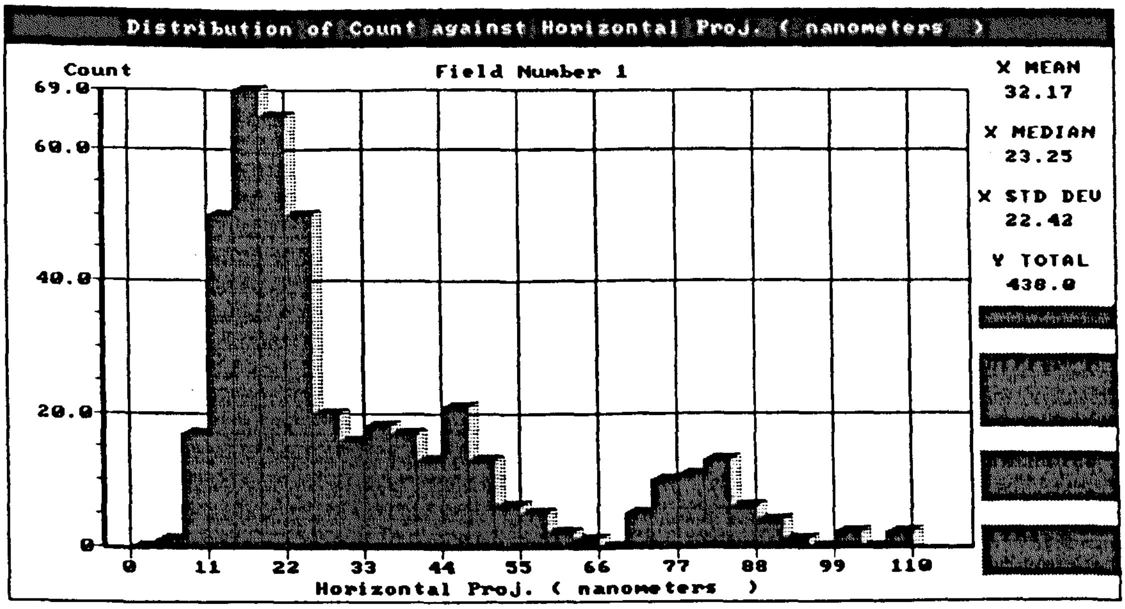

Figure 4-2. The distributions of stacking sizes L_c* for carbon fibres : E35C, E35, E55, E75, E105, E120, E130, and C700

E55

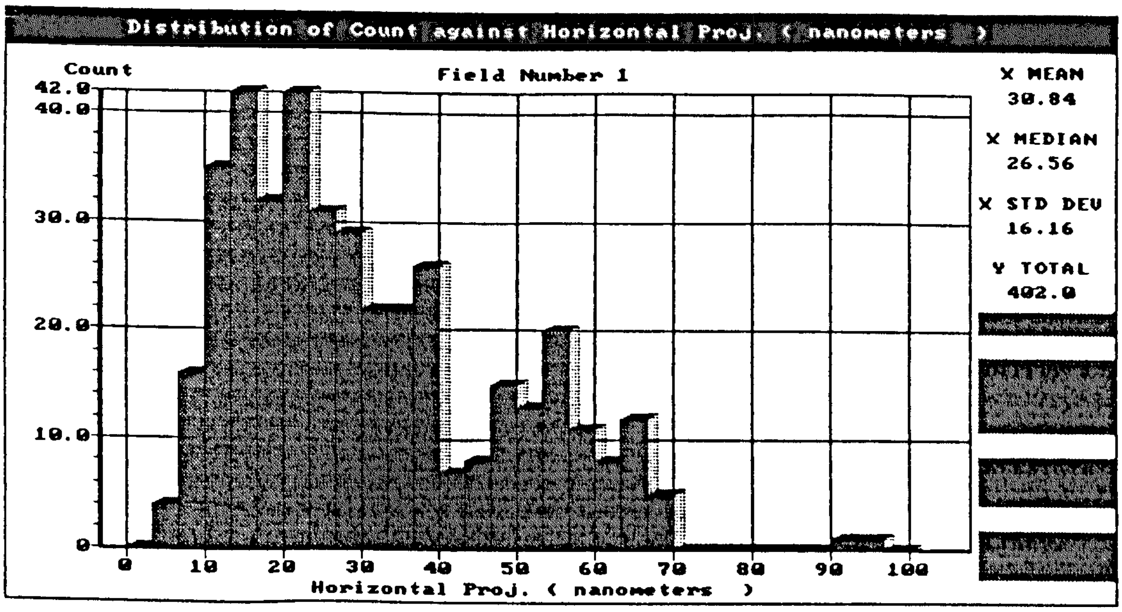

E75

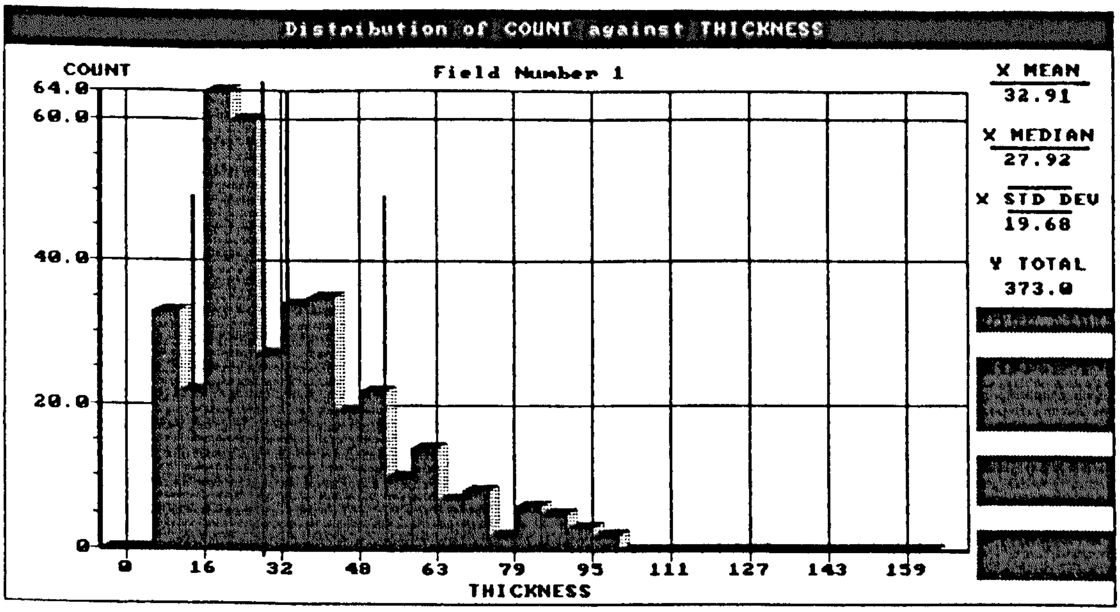

Figure 4-2. The distributions of stacking sizes L_c* for carbon fibres : E35C, E35, E55, E75, E105, E120, E130, and C700

E105

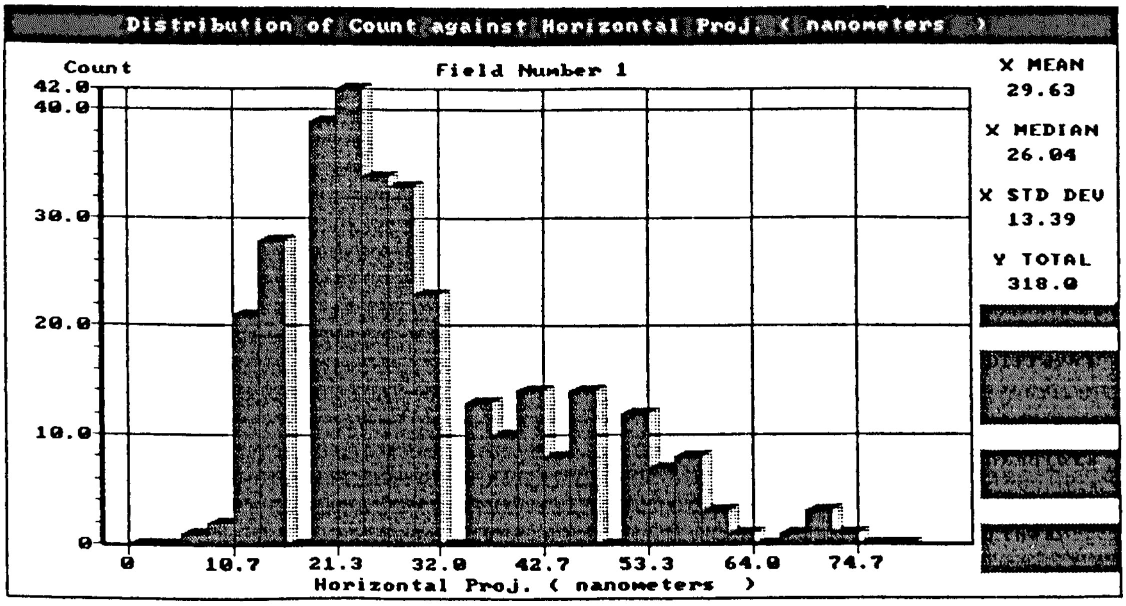

E120

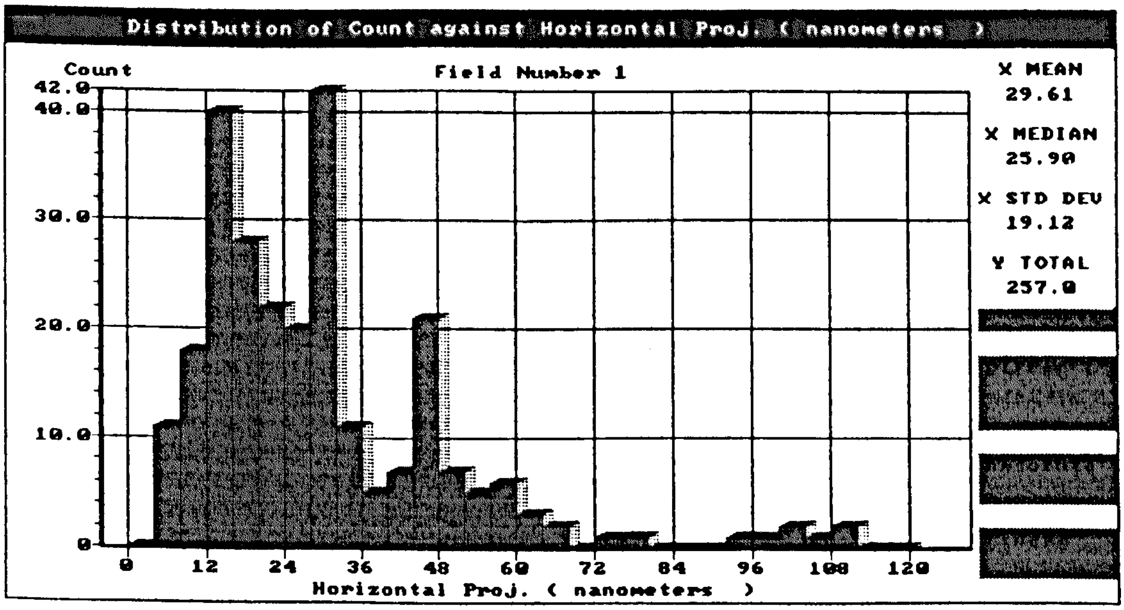

Figure 4-2. The distributions of stacking sizes L_c* for carbon fibres : E35C, E35, E55, E75, E105, E120, E130, and C700

E130

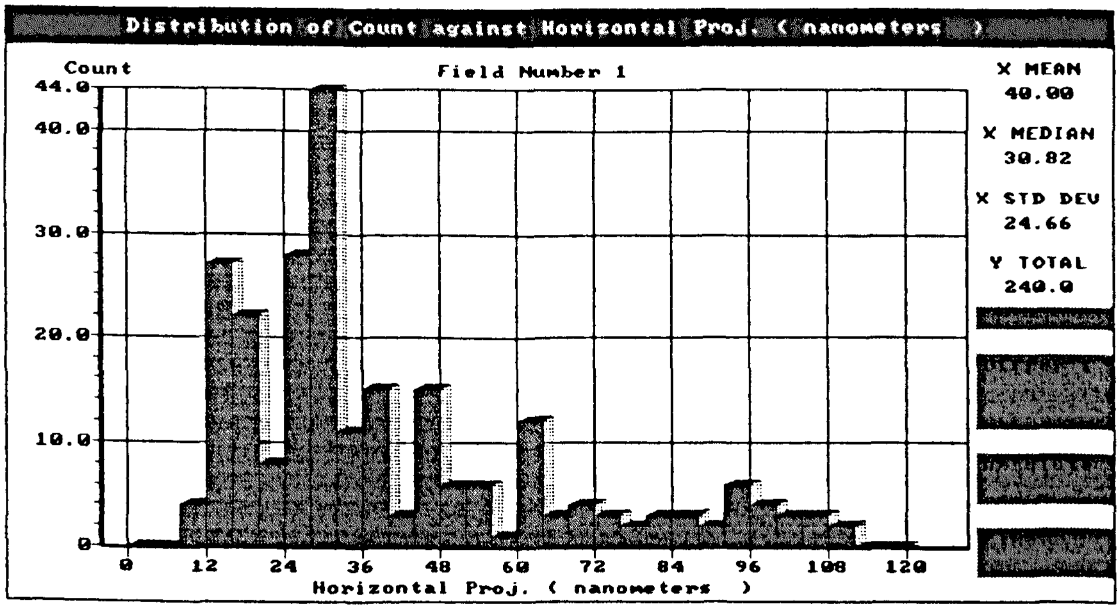

C700

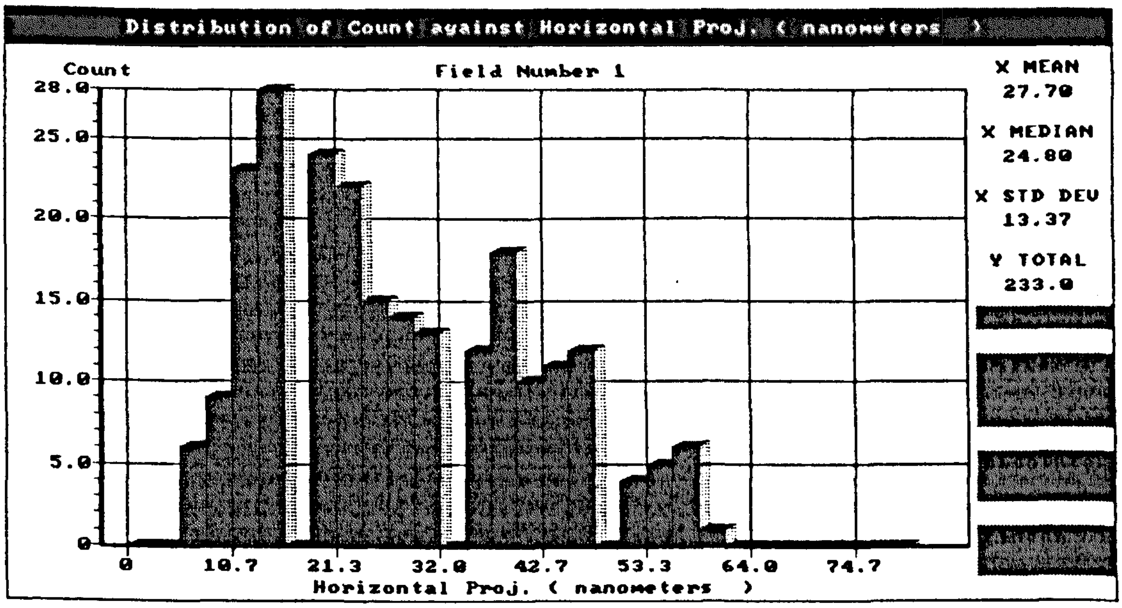

Figure 4-2. The distributions of stacking sizes L_c* for carbon fibres : E35C, E35, E55, E75, E105, E120, E130, and C700

4. 2. Axial orientation in carbon fibres

4. 2. 1. Introduction to orientation

Carbon fibres tend to have a high degree of preferred orientation of crystallites along the fibre axis, which promotes a high Young's modulus. The relationship between the degree of preferred orientation and Young's modulus for a variety of carbon fibres was studied by Ruland *et al.* and other workers [1,5,24,101]. Basically, increases in the Young's modulus of carbon fibres are directly related to improvement in the preferred orientation.

Usually, a high orientation of the precursor material tends to give a high orientation of the final carbon fibres [24,102]. However the preferred orientation in carbon fibres can also be increased either by a high-temperature heat treatment or by stretching the fibre during processing. A relationship between preferred orientation and the temperature of heat treatment for rayon-based carbon fibres has been obtained by Ruland [103]. The orientation is almost constant up to a heat treatment of $900^0\ C$ and then increases gradually with rising temperature. Shindo [94] found that the preferred orientation of PAN-based carbon fibres also shows an increase with rising temperature of heat treatment. The preferred orientation as a function of heat treatment temperature for MP-based carbon fibres was obtained by Bright and Singer [19] as shown in Figure 4-3. Generally the orientation improves significantly with heat treatment. However, the angular half-width was found to initially increase and then decrease.

The quantitative measurement of preferred crystallite orientation in carbon fibres can be determined from the intensity distribution $I_{00l}(\phi)$ of the (00l) reflection [104], where ϕ refers to the angle between the layer planes and the fibre axis (misorientation angle).

Basically the (00*l*) reflections of graphite and turbostratic carbon are spread in the form of arcs due to misorientation of the crystallites relative to the fibre axis. In the extreme case of complete misorientation, the (00*l*) reflections would be spread azimuthally into diffraction rings. In most cases, the (002) reflection is selected for measurement because its intensity is higher than the other (00*l*) reflections, and $I_{002}(\phi)$ is usually corrected for the broadening effect of finite crystallite size.

The preferred orientation derived from $I_{002}(\phi)$ may be defined in various ways as indicated below.

(a) The orientation parameter q

The orientation parameter q was proposed by Ruland [103] and determined by fitting

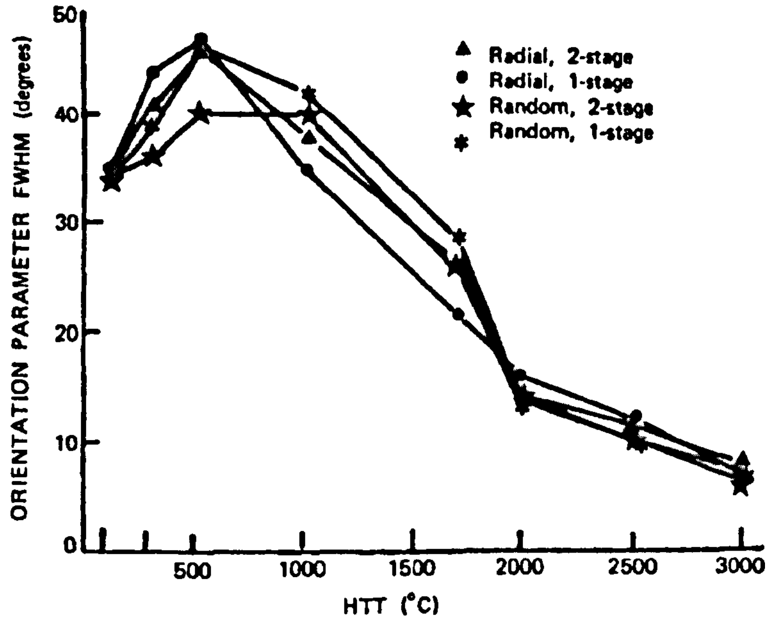

Figure 4-3. Preferred orientation as a function of heat treatment temperature in MP-based carbon fibre [19]

the measured intensity distribution function $I_{002}(\phi)$ to the expression :

$$I_{002}(\phi) = \frac{(1 - q^2)}{(1 + q^2 - 2q\cos\phi)}$$

The parameter q varies from +1 for perfect orientation perpendicular to the fibre axis, through 0 for random orientation, to -1 for perfect orientation parallel to the fibre axis.

(b) The orientation parameter R_{oz}

According to Price and Bokros [105], and also Gasparoux *at al.* [106], an orientation parameter can be calculated from the equation :

$$R_{oz} = \frac{\int I_{002}(\phi)\sin^3\phi d\phi}{\int I_{002}(\phi)\sin\phi d\phi}$$

The parameter R_{oz} varies from 2/3 for isotropic fibres to 1 for perfectly oriented fibres.

(c) The half height width orientation Z

The parameter Z, measured in degrees at half-maximum intensity, is the half-width of the intensity distribution function $I_{002}(\phi)$. Actually this parameter is a measure of the relative degree of misorientation of the basal planes to the fibre axis, and indeed it is very convenient for routine measurement of the preferred orientation of the carbon fibres.

(d) Integral breadth IB

Integral breadth of the diffraction intensity profile is defined as :

$$IB = \frac{1}{I_{max.}} \int_{0}^{\infty} I_{002}(\phi) d\phi$$

Where $I_{max.}$ is the maximum intensity of the scattering intensity profile $I_{002}(\phi)$. The value obtained for the integral breadth is given in degrees and is very similar to that obtained for the half-width orientation *Z*. The smaller the value of *IB*, the better the preferred orientation.

4. 2. 2. Preferred orientation

In this work, the preferred orientations of MP-based carbon fibres were determined from both X-ray and electron diffraction patterns and expressed using the parameter integral breadth.

4. 2. 2. 1. Measurement from X-ray diffraction patterns

The scattering intensity distribution of the (002) reflection was obtained by azimuthal scanning of each X-ray pattern in a Quantimet 570 image analyser. Using a program developed in this laboratory 'xorient5' azimuthal intensity scans through the (002) reflections were performed which were then processed to give the integral breadth. A typical plot of intensity against azimuthal angle is shown in Figure 4-4.

4. 2. 2. 2. Measurement from electron diffraction patterns

The experimental techniques for obtaining electron diffraction patterns including sample preparation and instrumental adjustment were explained in Chapter 2. For all carbon fibres, the diffraction patterns were obtained from both the peripheral and central regions (selected area diameter of 1 μm) of diametric longitudinal sections of the fibre. The integral breadths were calculated in the same way as for the X-ray diffraction patterns. In most electron diffraction patterns recorded in this work the (002) reflections were saturated, i.e. the scattering intensity distribution of the (002) reflection shows a plateau top profile which leads to a decrease of scattering intensity. Consequently it was decided to use the azimuthal intensity distributions of (004) reflections except for E35C since the (004) reflection is extremely weak and was not measured.

4. 2. 2. 3. Results and discussion

Table 4-2 gives the preferred orientation determined respectively from X-ray and electron diffraction patterns of MP-based carbon fibres.

Generally there is a good agreement between the results obtained from the two methods. Some differences between the values obtained from the two methods are to be expected, as the orientations from X-ray measurements are average values from a bundle of fibres whereas the values from the electron diffraction studies represent the orientations within much smaller regions of single fibres.

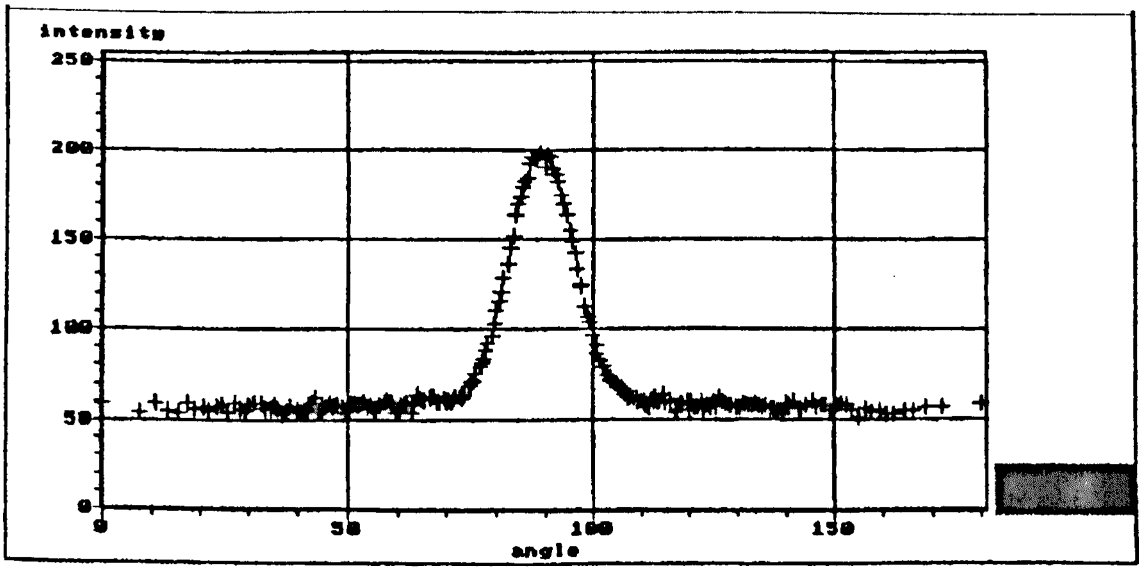

Figure 4-4 . A typical scatter plot of intensity against azimuthal angle from a X-ray pattern.

Table. 4-2 The integral breadth (degrees) of MP-based carbon fibres

Fibres	**X-ray (002)**	**SAD (004)**	
		periphery	**centre**
E35C	28.1	----	----
E35	28.4	24.7	21.1
E55	20.1	19.2	24.0
E75	16.3	20.0	17.8
E105	13.8	12.8	11.5
E120	11.4	10.2	11.4
E130	12.5	10.1	11.1
C700	9.4	9.9	8.8

As indicated in table 4-2 the integral breadths obtained from electron diffraction patterns of the periphery and central regions are similar indicating little difference in orientation across the fibres (i. e. no skin / core organization).

The relationship between Young's modulus and integral breadth derived from each method is shown in Figure 4-5. It is clear that the orientation improves gradually from the lower modulus fibre E35C to the very high modulus fibre C700. For the series of fibres E35 to E130, the relationship between the Young's modulus and the integral breadth is almost linear.

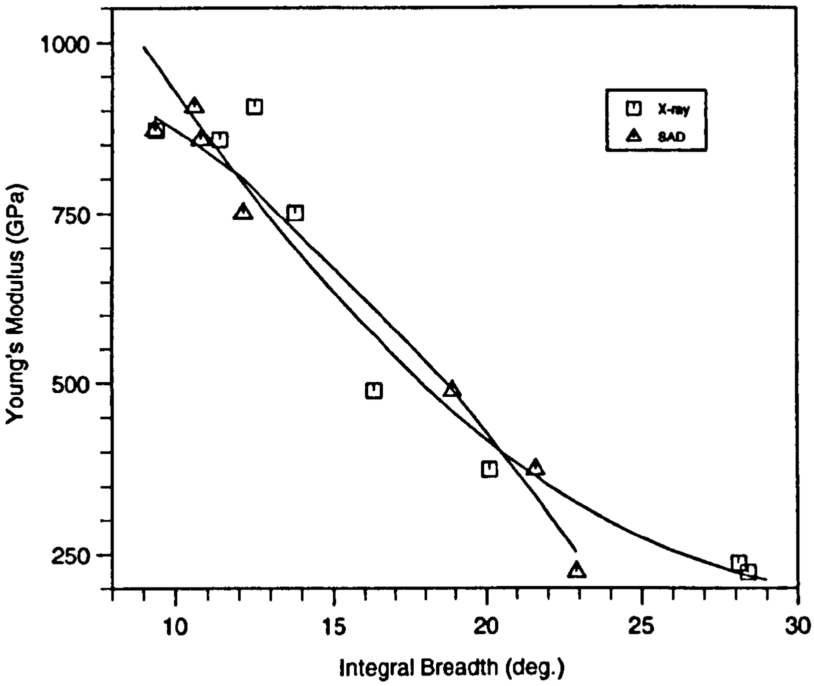

Figure 4-5. The relationship between Young's modulus and integral breadth of (002) from X-ray and (004) from SAD

4. 2. 3. Local orientation

If an individual crystallite is regarded as a domain, then the short range alignment of the layer planes relative to the domain axis may be referred to as the local orientation. Here the domain axis is defined as the long range average direction of the layer planes within the domain. The difference between the local orientation and the preferred orientation is illustrated in Figure 4-6. Clearly the preferred orientation refers to the average long range layer plane alignment angle relative to the fibre axis whereas the local misorientation relates to the short range layer plane alignment angle within single crystallites relative to the crystallite (domain) axis.

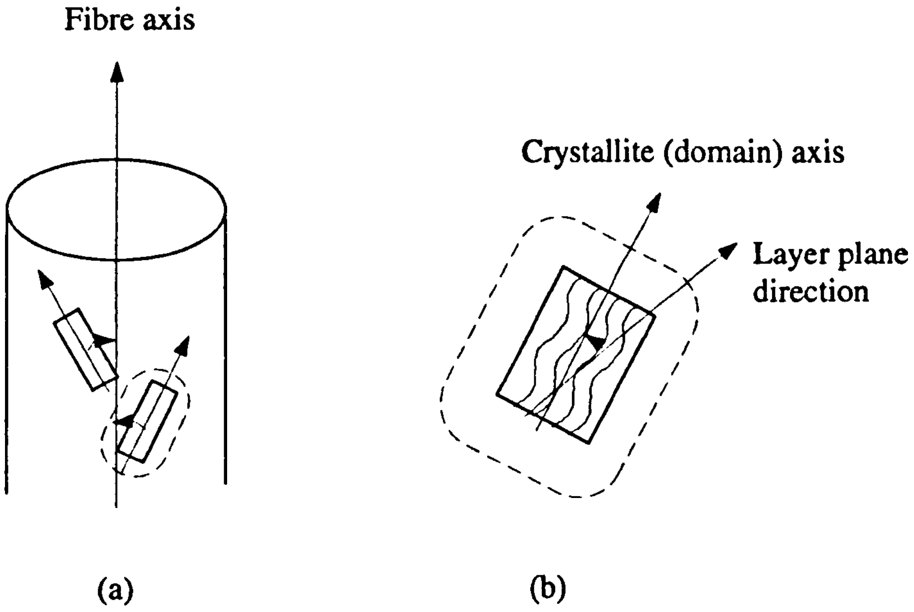

Figure 4-6. Schematic diagram illustrating the difference between (a) preferred orientation and (b) local orientation.

4. 2. 3. 1. Direct measurement from lattice-fringe images

Since a (002) lattice-fringe image is derived from a particular crystallite and can be regarded as the geometric projection of (002) layer planes on the image plane, consequently it is possible to estimate directly the local orientation of layer planes from such images using the image analyser.

The misorientation angle, derived from the calculated orientation α (as measured by the Quantimet 570), was used to represent the local orientation within a crystallite. The relation between the calculated orientation α and the misorientation angle ϕ ($\phi=\alpha-90^0$) is shown in Figure 4-7. The misorientation angle varies from 0^0 for perfect orientation parallel to the crystallite axis to 90^0 for perfect perpendicular orientation.

Before carrying out the misorientation measurements on the Quantimet 570 the acquired lattice-fringe images from electron micrographs were subject to a series of image processing stages including sharpening, skeletonisation and editing which were performed using built-in software. A typical processed image is shown in Figure 4-8.

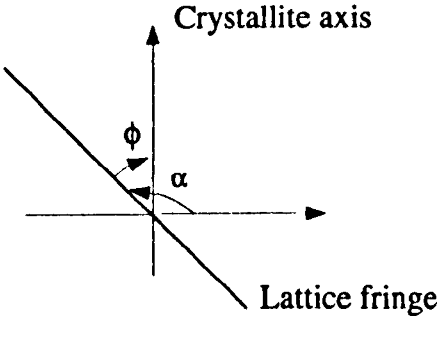

Figure 4-7. Schematic diagram showing calculated orientation α and misorientation angle ϕ

In order to obtain information about the local misorientation angles of the fringes a series of equally spaced horizontal grid lines were superimposed on the processed images displayed on the monitor. The critical step in this procedure is to decide the grid spacing (i.e. the distance between two grid lines) since for meandering lattice fringes this spacing will give rise to different values of the local misorientation angle of segments of the fringes. In this work eight grid spacings were selected ranging from 0.29 *nm* (10 pixels) to 1.3 *nm* (45 pixel). In addition, the lattice-fringe segments situated at the top and the bottom of the displayed image were removed from the image since they are usually smaller than the grid spacing.

The processed grey images were then transferred into binary images by detecting the white fringe segments on the black background, and orientation measurements were carried out using the standard software. The distributions of misorientation angle were obtained for each group of grid size from which the average and standard deviation of the misorientation angle can be derived. Subsequently the relationships between the misorientation angles of the lattice-fringe image and grid sizes were obtained for each carbon fibre sample.

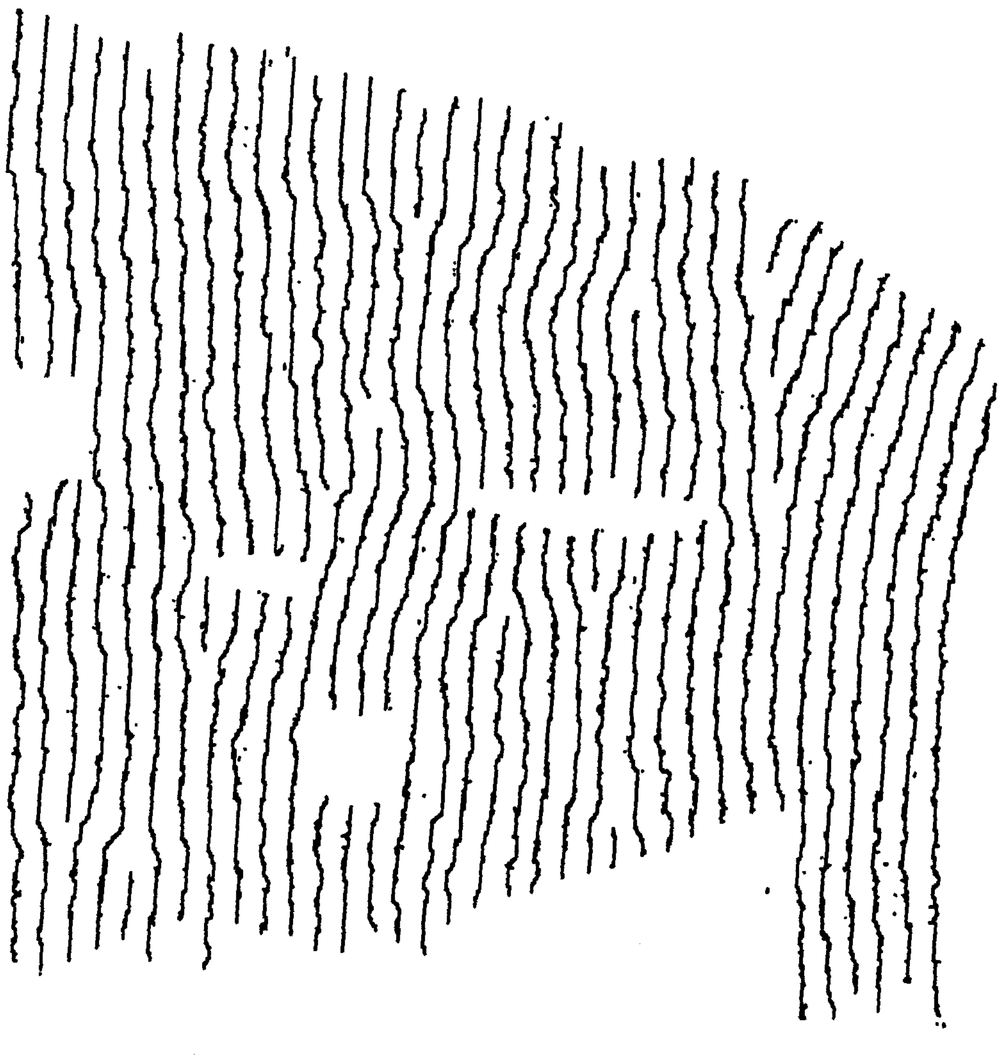

Figure 4-8. A typical processed lattice-fringe image

4. 2. 3. 2. Fast Fourier Transform of lattice-fringe images

An alternative method to the direct local orientation determination of lattice fringes is by using the Fourier transforms of lattice-fringe images. Since the lattice-fringe image is formed by interference between the direct beam and diffracted reflections the Fourier transform of the (002) lattice-fringe image should be analogous to the distribution of the (002) electron diffraction from individual crystallites. However the selected area electron diffraction pattern is usually obtained from a relatively larger region of the fibre section compared with the restricted extent of lattice-fringe images due to the high magnification necessary for visualisation.

The Fast Fourier Transform of the lattice-fringe image was carried out on the Quantimet 570 image analyser using the software QFFT [79]. The image (size 512x512 pixels) was first transformed into the frequency domain and then displayed as a power spectrum in which the grey level of each pixel was scaled to lie in the grey level range of 0-255.

A typical (002) azimuthal scattering profile from the transformed image is shown in Figure 4-9. The azimuthal integral breadth of the (002) reflection was calculated using the same method as described in section 4. 2. 2.

However, it is important to note that due to the finite image size, the intensity profile obtained from the transformed image is theoretically broadened and leads to increased integral breadths. In order to determine the size-broadening factor, a parallel line grating was drawn in the image plane of the Q570 (using appropriate software) so as to simulate a perfect array of lattice fringes. The analogue lattice fringes have identical line width and spacing, and consequently the intensity profile obtained from this analogue image is only broadened by the effect of finite image size. In the present work, however, no corrections have been applied to the IB determination of the transformed images since the integral breadth obtained from the profile of the analogue image was extremely small (about 2 pixel width) and can be neglected.

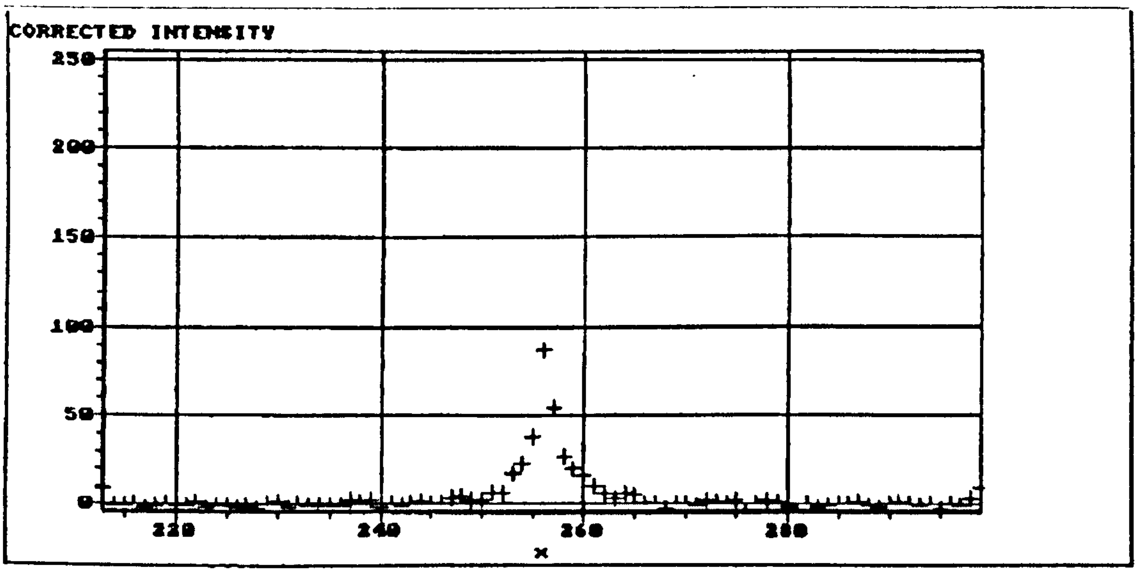

Figure 4-9. The scatter plot of intensity against azimuthal angle from a transformed image of fibre C700

4. 2. 3. 3. Results and discussion

Figure 4-10 gives the relationship between the average misorientation angle of the lattice fringes within single crystallites and the grid spacing. Clearly there is a marked decrease in misorientation angle from fibre E35C to fibre C700 irrespective of the grid spacing.

If the fringes were perfectly oriented over a long range there should be no change in orientation with grid spacing. However in the carbon fibres examined here the variation of local orientation is clearly seen from each individual graph. As the grid spacing increases the misorientation angle exhibits a continuous decrease for fibre E35C whereas for all other fibres there is an initial decrease followed by a plateau region. Closer inspection shows that the total decrease in the misorientation angle over a distance of 1 *nm*

gradually becomes smaller from fibre E35C (6^0) to the fibre C700 (1^0). In contrast to the short range variations in misorientation angle exhibited by all other fibres, E35C shows longer range variations in misorientation angle. This implies that the lattice fringes of the latter fibre meander considerably.

Table 4-3 shows both the integral breadth (IB) and misorientation angle ϕ obtained respectively from the Fourier transforms and direct local measurement of lattice fringes for MP-based carbon fibres.

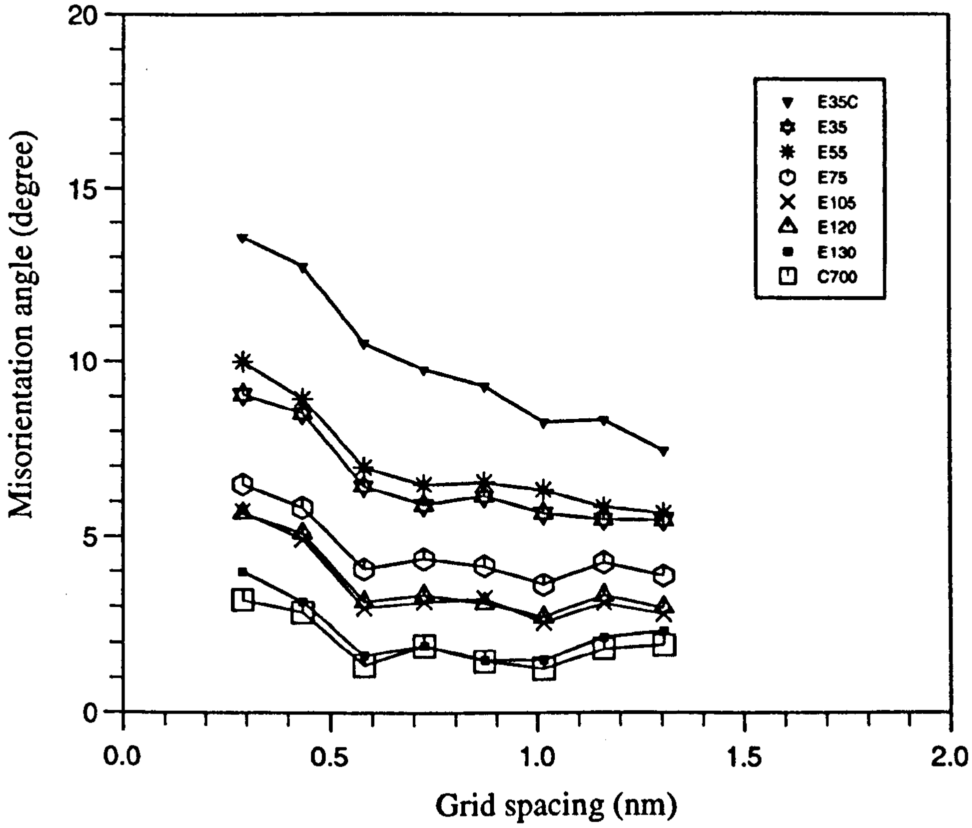

Figure 4-10. The plot of misorientation angle against grid spacing

Both values of integral breadth and misorientation angle show the same tendency, i.e. local orientation improves gradually from E35C (least ordered) to C700 (highly ordered).

Theoretically the integral breadth values should be approximately twice the misorientation angle values (see definitions in sections 4. 2. 3.). In this work it was found that the former will be indeed approximately twice the latter if the misorientation angle ϕ is measured at an appropriate grid spacing. For example, in the cases of fibres E35C, E35, E55 and E75, IB values are approximately twice the ϕ values measured at grid spacing of 0.29 nm; while in the cases of other fibres, the same results will be obtained if it is measured at a larger grid spacing than 0.29 nm. In fact, as explained previously the local misorientation angle varies considerably with changing grid spacing due to the tortuosity of the lattice fringes (as indicated in Figure 4-10 and table 4-3). Generally, in the cases of short range ordered fringes (high tortuosity), a small grid spacing is preferred as the localized information might be concealed by applying the large grid spacing.

Table 4-3. Local orientation measurements of MP-based carbon fibres

Fibres	IB (deg.)	ϕ (deg.) at grid spacing (nm) :							
		0.29	**0.44**	**0.58**	**0.73**	**0.87**	**1.02**	**1.16**	**1.31**
E35C	27.5	13.6	12.7	10.5	9.8	9.3	8.3	8.3	7.4
E35	22.5	9.1	8.5	6.4	5.9	6.1	5.7	5.5	5.5
E55	21.4	10.0	8.9	7.0	6.5	6.5	6.3	5.8	5.6
E75	13.4	6.5	5.8	4.1	4.4	4.2	3.6	4.3	3.9
E105	10.6	5.7	4.9	3.0	3.1	3.2	2.5	3.1	2.8
E120	8.0	5.7	5.1	3.2	3.3	3.1	2.7	3.3	3.0
E130	5.3	4.0	3.2	1.6	1.9	1.5	1.5	2.1	2.3
C700	2.7	3.2	2.9	1.4	1.9	1.5	1.3	1.8	1.9

4. 3. Lattice imperfections in carbon fibres

4. 3. 1. Introduction to lattice defects in carbon fibres

The unit cell of a single graphite crystal is hexagonal, in which a number of carbon layer planes are stacked in a regular ABAB type sequence. The accepted value of the interlayer spacing (d-spacing) for perfect graphite is 0.3354 *nm* [21], however variability in interlayer spacing has been reported [72] in a variety of carbon fibres with values ranging from 0.3354 *nm* to more than 0.3440 *nm* (turbostratic). Such differences have been ascribed to different degrees of disorder. The most significant difference in crystallite structure between graphite and turbostratic carbon is that graphite exhibits complete three-dimensional regularity while turbostratic carbon refers to a random stacking of carbon layer planes (see Figure 1-3).

Disorder in carbon fibre structure can be considered to arise from: (1) disorder between crystallites; (2) lattice imperfections within crystallites. Generally lattice imperfections are sub-divided into three types: (1) imperfections within one layer plane, (2) stacking imperfections between neighbouring layer planes, and (3) dislocations of single and stacked layers [22].

Park [72] has measured the relative degree of inter-crystallite disorder $D_d\%$ in both PAN- and MP-based carbon fibres from the resolved background areas in X-ray diffraction traces, and found that the $D_d(\%)$ provides useful information for comparison purposes between the various type of carbon fibre. However, this parameter represents the degree of disorder only over a limited 2θ range (10^0 -65^0) and cannot be regarded as an absolute value.

The degree of disorder in carbon fibre can also be determined using other techniques such as Raman Spectroscopy [22]. The intensity ratio from Raman Spectra is defined as $R = I_{1360}/I_{1580}$, where I_{1360} is the integrated intensity of the disorder-induced peak and I_{1580} is the intensity of the graphite peak, has been found to be closely related to the in-plane crystallite size L_a [107]. Unfortunately this technique only provides information about the surface structure (depth of 50 *nm*) and is not suitable for the characterization of the bulk structure of carbon fibres.

The degree of turbostratic disorder in carbon fibre can be quantitatively measured from X-ray diffraction studies. Maire and Mering [108] introduced an empirical graphitization index G_p, $G_p = \frac{0.3440 - d_{002}}{0.3440 - 0.3354}$ which depends linearly on the interlayer spacing d_{002} obtained from the (002) X-ray reflections, to represent the degree of disorder. The values 0.3440 and 0.3354 refer to the average values of the interlayer spacings in a turbostratic structure and perfect graphite respectively, and the former value can be adjusted in different cases so as to maintain a positive value for G_p. Similarly Park *et al.* [109] introduced a parameter D_c, where D_c=1-G_p, but replaced 0.3440 by 0.350 to calculate the relative degrees of intra-crystallite disorder for both PAN- and MP-based carbon fibres. They found that the parameter D_c is generally proportional to the relative degree of inter-crystallite disorder D_d(%) obtained from the resolved background areas in X-ray diffraction trace. Shioya and Takaku [110] have also characterized the stacking disorder of pitch-based carbon fibres by X-ray measurement. They suggested that the distribution of the interlayer spacings in a crystallite can be represented by a skewed distribution function having a longer tail at larger spacing, and that the stacking disorder diminishes while the asymmetry of the distribution increases when the mean interlayer spacing approaches that of the graphite single crystal. Other workers have also attempted to relate interlayer spacing from bulk carbons to disorder using models for the interatomic interactions [111] although Ruland [88] has critically reviewed these models.

TEM lattice-fringe images appear to offer a more direct method of estimating lattice imperfections, since the images directly reveal the way in which imperfections disturb the periodicity of a crystal. Indeed the presence of lattice imperfections in carbon fibre structure was qualitatively revealed in lattice-fringe images by both previous workers [33,72] and by the present work. However quantitative measurement and analysis of the lattice imperfections from such images have not previously been attempted. Fortunately image analysis techniques have made it possible to quantify the required information. Specific statistical data can therefore be obtained in this way, which gives direct measurement of the degree of the disorder.

4. 3. 2. Measurement from lattice-fringe images

4. 3. 2. 1. The variation of interlayer spacing

Generally the 002 interlayer spacing determined from X-ray studies is an average value. However, from analysis of TEM lattice-fringe images both the average interlayer spacing and distribution of spacings can be determined.

The measurement of d-spacings was based on grey lattice-fringe images. Using the Quantimet 570, intensity profiles across the images can be obtained directly as shown in Figures 4-11a, hence fringe positions and spacings can be determined. For example the distance between adjacent peaks represents individual d-spacings.

However as shown in Figures 4-11a, due to image noise the profile often appears to be slightly irregular, which results in difficulties associated with precisely defining the

(a)

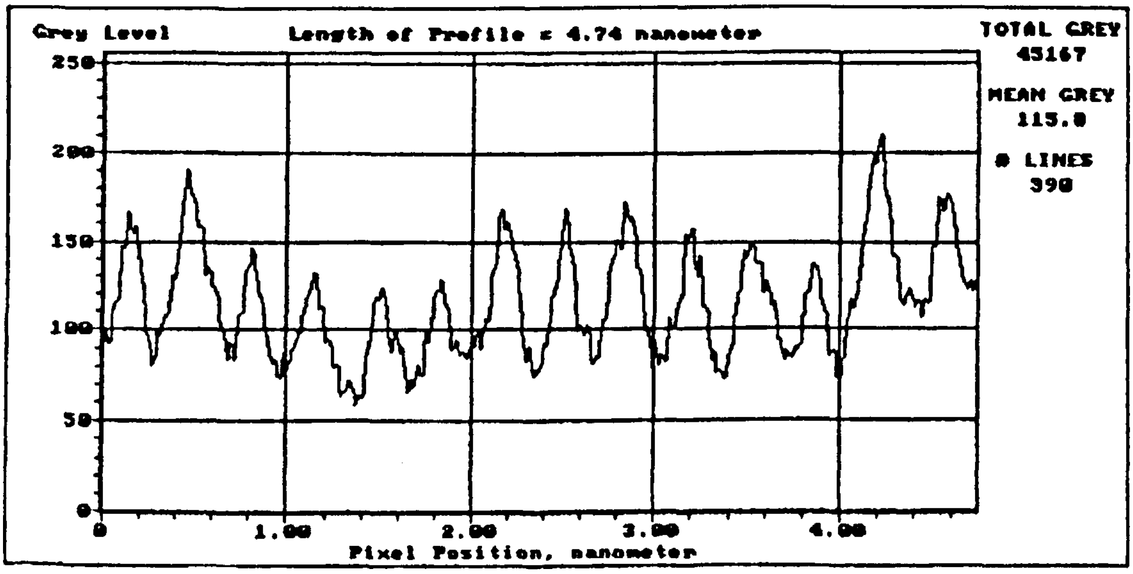

(b)

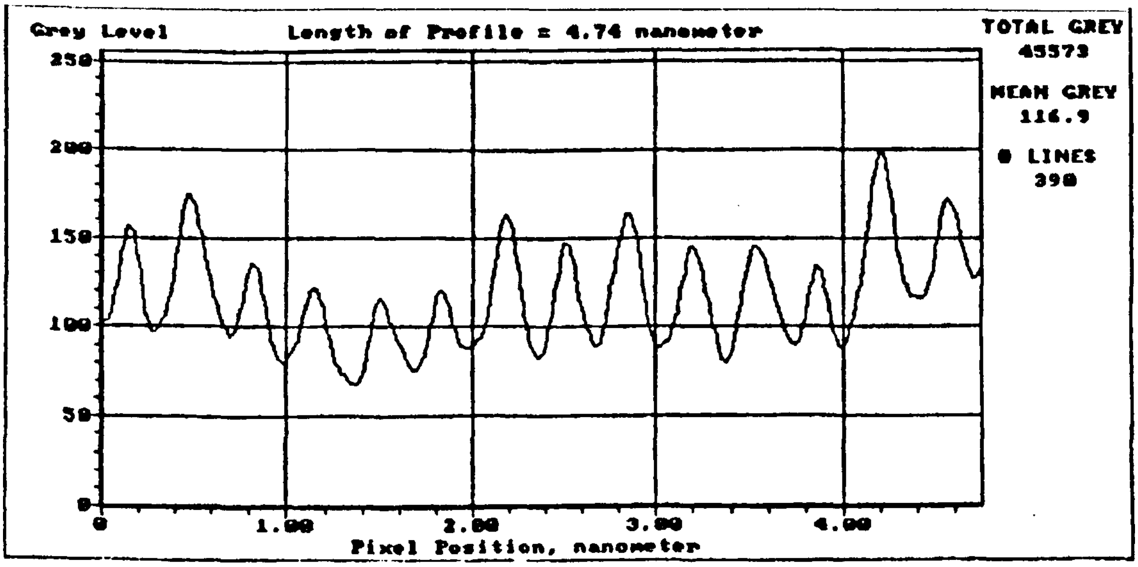

Figures 4-11. Horizontal line scans of the lattice-fringe image in the form of (a) the original grey image, and (b) the averaged grey image

peak maximum. In order to filter out the noise and hence smooth the image, the AVERAGE transform (using a 5×5 matrix as unit kernel) was performed on a stored grey image in the Quantimet. The grey level profile obtained from the smoothed image is shown in Figures 4-11b. It is clear that the peak position can be determined more precisely and easily from this smoothed profile compared with the original one shown in Figures 4-11a.

A computer program for the image analyser was written (see appendix) to calculate the d-spacings from the smoothed lattice-fringe images. Data was collected from 200 individual lattice fringes per image. Histograms of the distribution of d-spacings were generated respectively for each fibre sample, from which the average value and standard deviation of the d-spacing were computed.

Importantly, in order to obtain the accurate interlayer spacing from the lattice-fringe images, the magnification of the image must be known. Unfortunately, the TEM was not accurately calibrated, nevertheless, all lattice-fringe images of the fibre were recorded under the same instrumental optical magnification. In the present work, therefore, a normalization was made on the basis of the X-ray interlayer spacing value for fibre C700. Thus the interlayer (lattice) spacings as determined for other carbon fibres represent the values relative to that of fibre C700.

It should be noted that the error in measurement of the interlayer spacing is ±0.012 *nm*. The average interlayer spacings d_{002} measured from the 002 lattice-fringe images are listed in table 4-4.

It is clear that the most noticeable feature of the interlayer spacing measurement is the gradual increase from a value 0.336 *nm* possessed by the fibre C700 to a value

Table 4-4. Lattice imperfection parameters obtained from lattice-fringe images

Fibres	**TEM average** d_{002} (nm)	**Tortuosity** S (%)
E35C	0.363	14.8 (9.0)
E35	0.353	12.8 (6.7)
E55	0.344	10.8 (5.7)
E75	0.342	7.2 (3.6)
E105	0.343	6.3 (3.4)
E120	0.337	2.2 (2.4)
E130	0.338	1.8 (1.9)
C700	0.336	2.1 (1.7)

0.363 *nm* by the fibre E35C. Apart from E35C and E35 these values are consistent with the results obtained from X-ray diffraction (see Chapter 3). For these two fibre specimens, the discrepancy between the values obtained from TEM measurement and the values from X-ray diffraction might be due to considerably meandering of the layer planes. In the case of very disordered specimens, lattice imperfections may disturb the localised periodicity of layer planes in such a way that the X-ray beam is not scattered at the Bragg angle. Thus the individual spacings between such planes do not contribute to the X-ray average d-spacings from the bulk specimen. Consequently the average d-spacings obtained from X-ray diffraction will exhibit relatively lower values compared with those obtained from the lattice-fringe images in which the spacings between the disturbed layer planes can be measured directly. Indeed in these two specimens the d-spacings are higher than the value normally accepted for turbostratic graphite (0.3440 *nm*). This may suggest that the value of 0.3440 *nm* is too low an estimate for very disordered specimens.

Figure 4-12 shows the distributions of interlayer spacings for all the fibres examined. The narrow distribution profile for the fibre C700 suggests that the variation of interlayer spacing in this fibre is considerably smaller than that in the case of say E35C. This, in turn, implies that the regularity and the uniformity of the layer packing decrease from fibre C700 to fibre E35C.

Theoretically the distribution of interlayer spacing in a turbostratic carbon should be asymmetric and have a longer tail at larger spacing (a skewed distribution) [110], since the average d-spacing generally shows a larger value than that of graphite (0.3354 *nm*). In this work the distributions are indeed asymmetric.

E35C

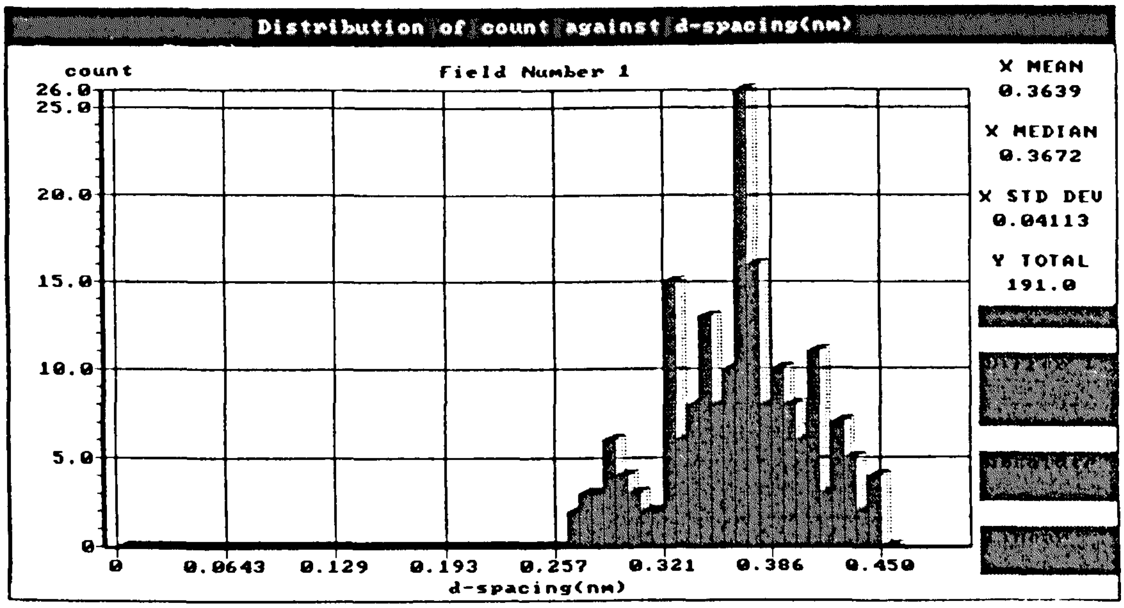

X MEAN
0.3639
X MEDIAN
0.3672
X STD DEV
0.04113
Y TOTAL
191.0

E35

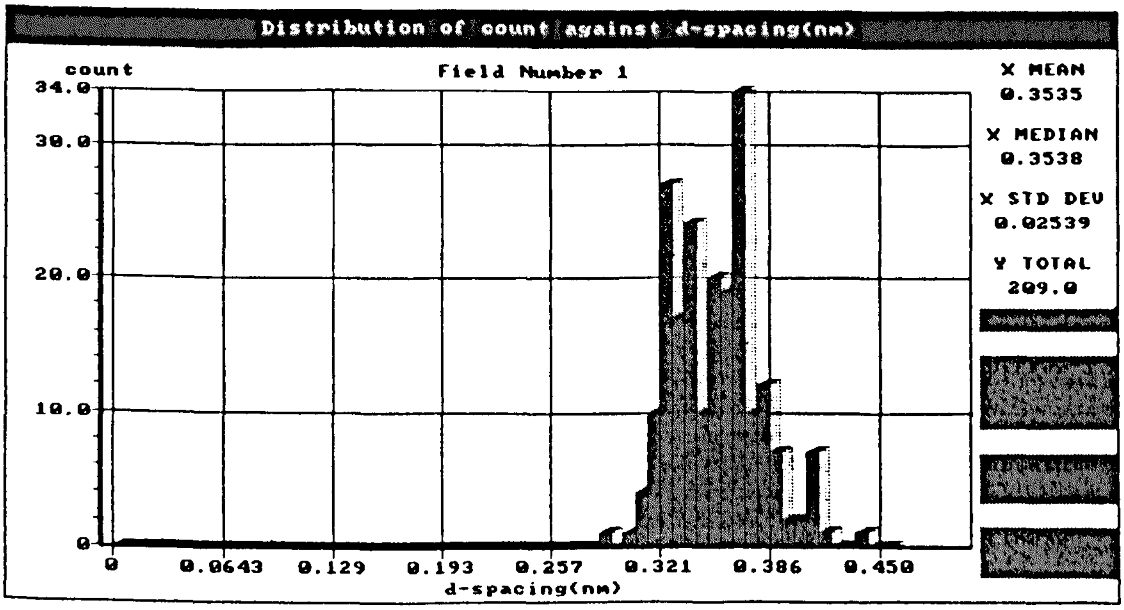

X MEAN
0.3535
X MEDIAN
0.3538
X STD DEV
0.02539
Y TOTAL
209.0

Figure 4-12. The distributions of interlayer spacing for carbon fibres : E35C, E35, E55, E75, E105, E120, E130 and C700

E55

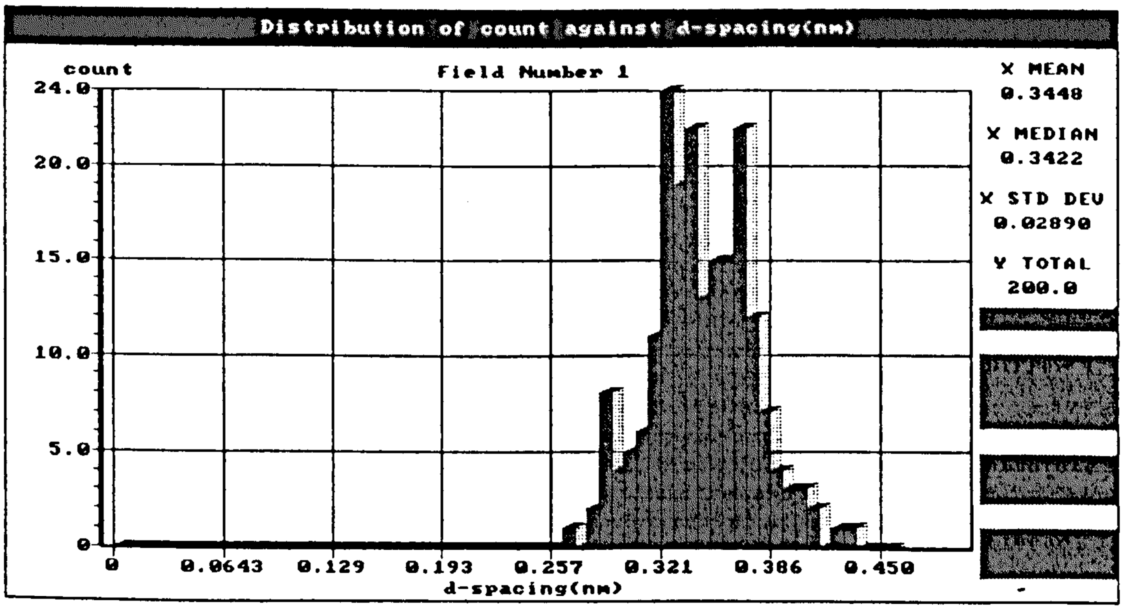

X MEAN
0.3448
X MEDIAN
0.3422
X STD DEV
0.02890
Y TOTAL
200.0

E75

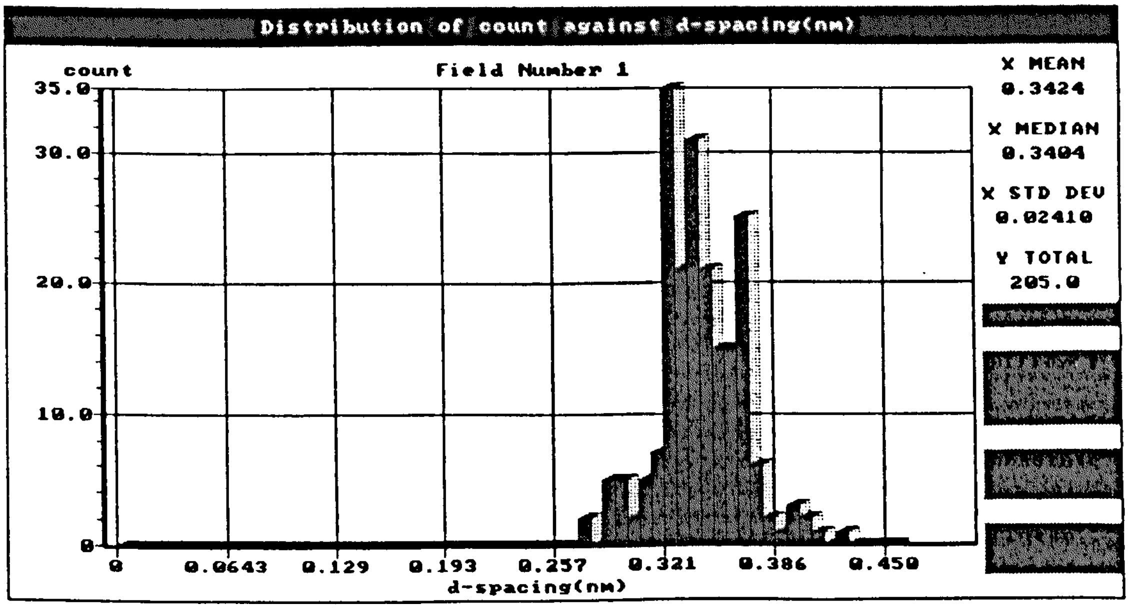

X MEAN
0.3424
X MEDIAN
0.3404
X STD DEV
0.02410
Y TOTAL
205.0

Figure 4-12. The distributions of interlayer spacing for carbon fibres : E35C, E35, E55, E75, E105, E120, E130 and C700

E105

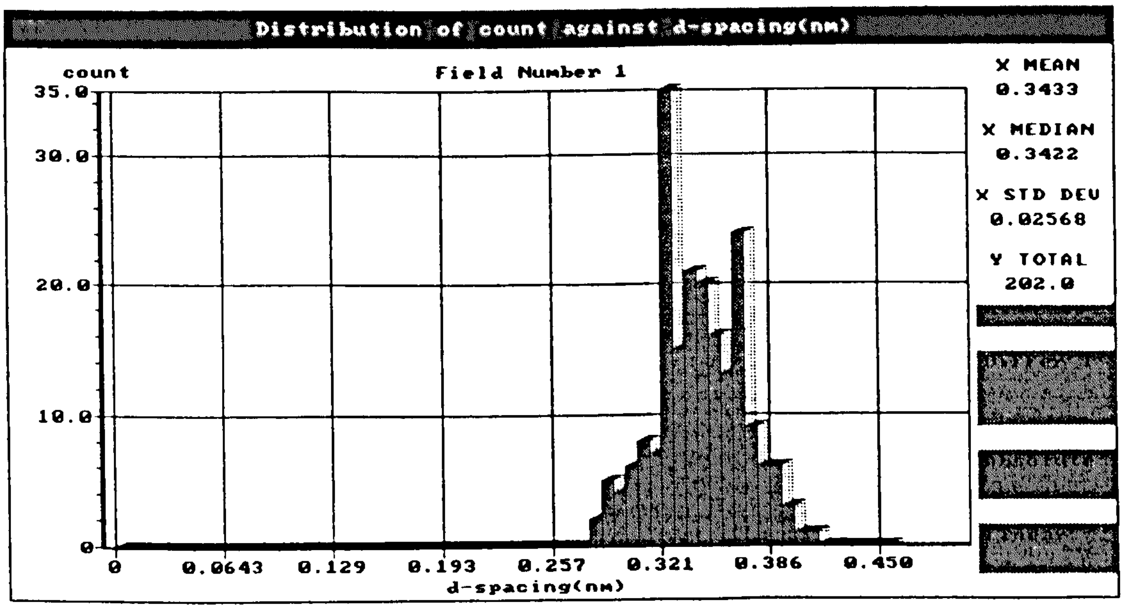

E120

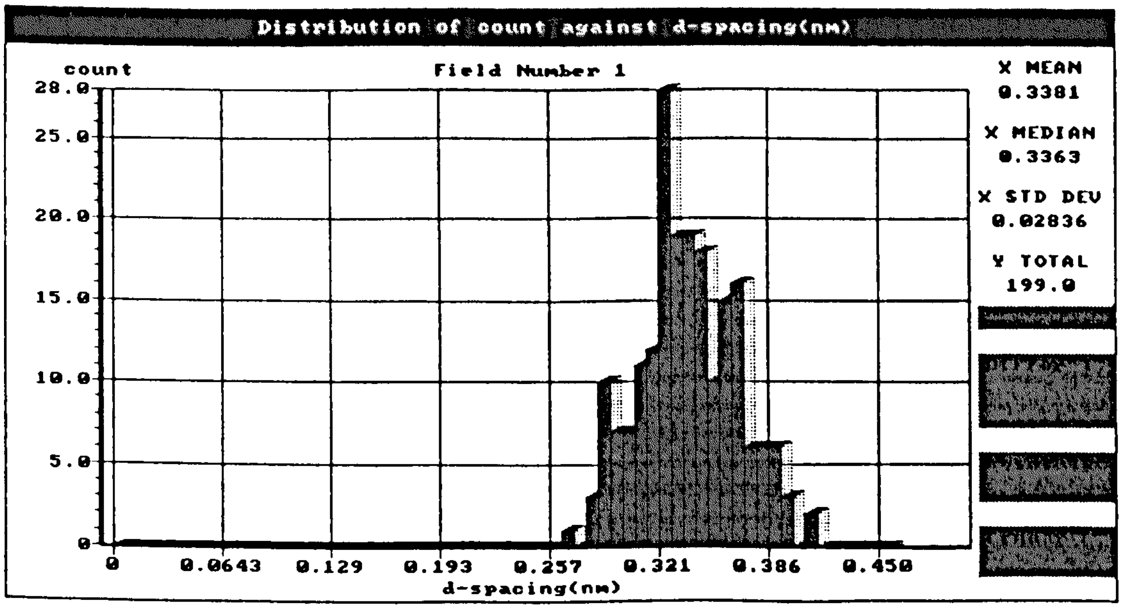

Figure 4-12. The distributions of interlayer spacing for carbon fibres : E35C, E35, E55, E75, E105, E120, E130 and C700

E130

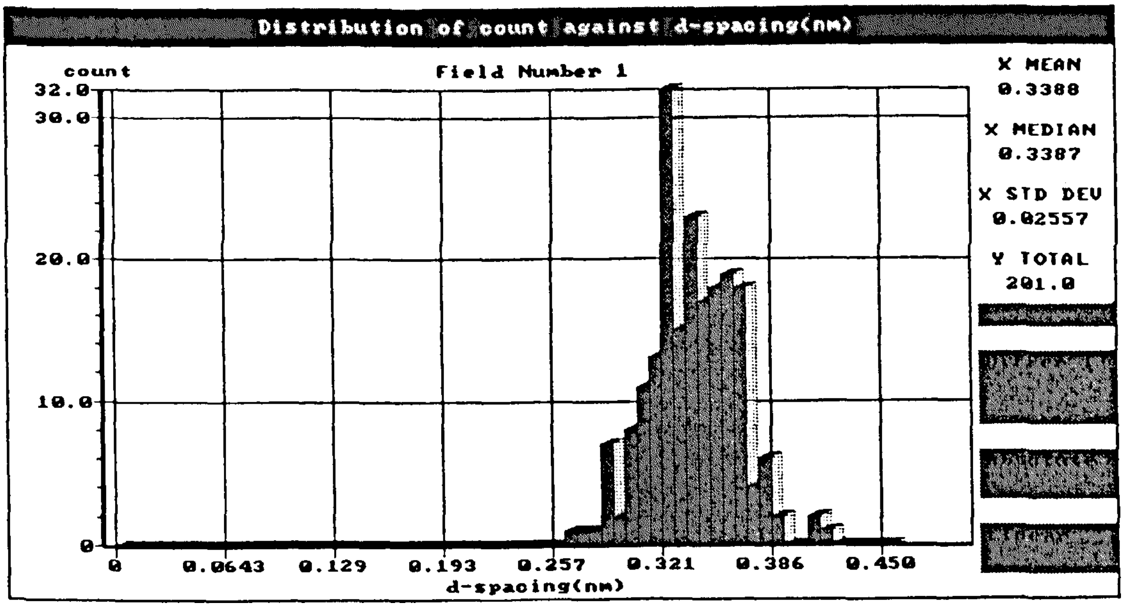

C700

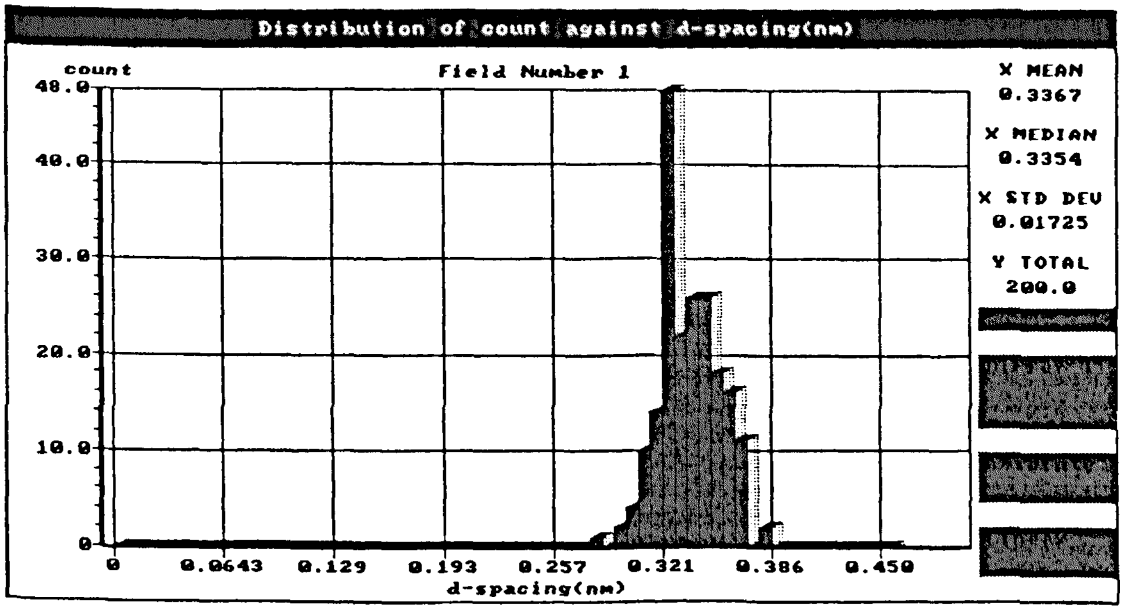

Figure 4-12. The distributions of interlayer spacing for carbon fibres : E35C, E35, E55, E75, E105, E120, E130 and C700

4. 3. 2. 2. Tortuosity of layer planes

Particularly in fibres E35C, E35 and E55, visual inspection of high resolution images showed that the lattice fringes tend to meander considerably, a similar conclusion was reached by analysis of local misorientation data. It was decided therefore to attempt to quantify these effects by expressing the meandering of lattice fringes in term of a tortuosity parameter S(%), which is defined as :

$$S(\%) = \frac{(l_f - l)}{l} \times 100\%$$

where l is the length of individual fringes (the longest Feret), and l_f is the true fringe length being measured following any curvature as shown in Figure 4-13; l_f is determined as follows. Suppose the meandering fringe of area A is straightened so as to form a rectangle of length l_f, breadth b_f. Then the area $A = l_f \text{x} b_f$, and the perimeter $P = 2\text{x}(l_f + b_f)$; l_f can then be expressed as:

$$l_f = \frac{1}{4}\left(P + \sqrt{P^2 - 16A}\right)$$

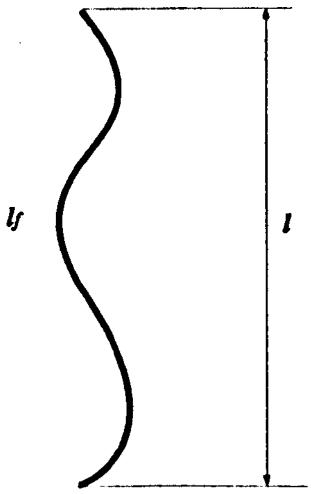

Figure 4-13. Schematic diagram showing the definition of the longest Feret of a fringe l and the true fringe length l_f

The above procedure was applied to samples E35C and E35 where individual fringe lengths were less than the displayed image length. In all other samples where the fringe lengths were larger than the image length, *l* was taken as the image length.

The tortuosity measurements were based on processed lattice-fringe images. The most important steps in the processing are outlined below.

(1) Modification of the original grey image using a computer program 'LATTICE' (developed in this laboratory) to minimise long range contrast changes, a comparison of original image with modified image is shown in Figure 4-14; and (2) use of 'AVERAGE(7×7)' built-in software to smooth fringe outlines. Typical processed lattice-fringe images are shown in Figure 4-15.

The average values of fringe tortuosity S(%) with standard deviations in brackets, measured from the 002 lattice-fringe images, are listed in table 4-4, and the distributions for each specimens are shown in Figures 4-16.

It is clear that the tortuosity values and their standard deviation increase steadily from fibre C700 to E35C. This quantitative data confirms that as the graphitization process develops (Young's modulus increases) the tortuosity of the lattice fringes progressively decreases until the fringes in fibres C700 and E130 are almost linear (i.e. development of lattice perfection).

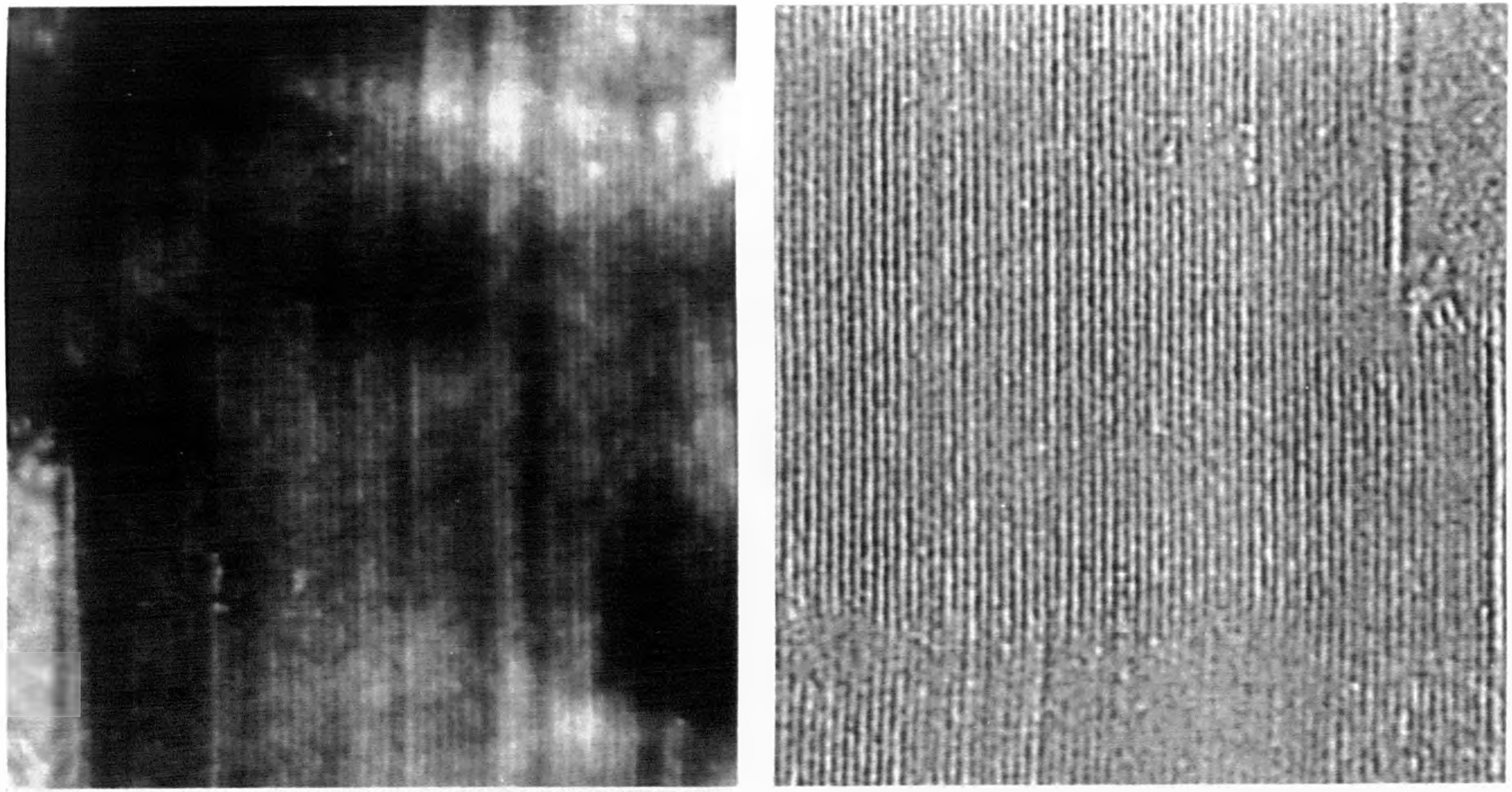

Original image

Processed image

Figure 4-14. A comparison of an original image with a processed image

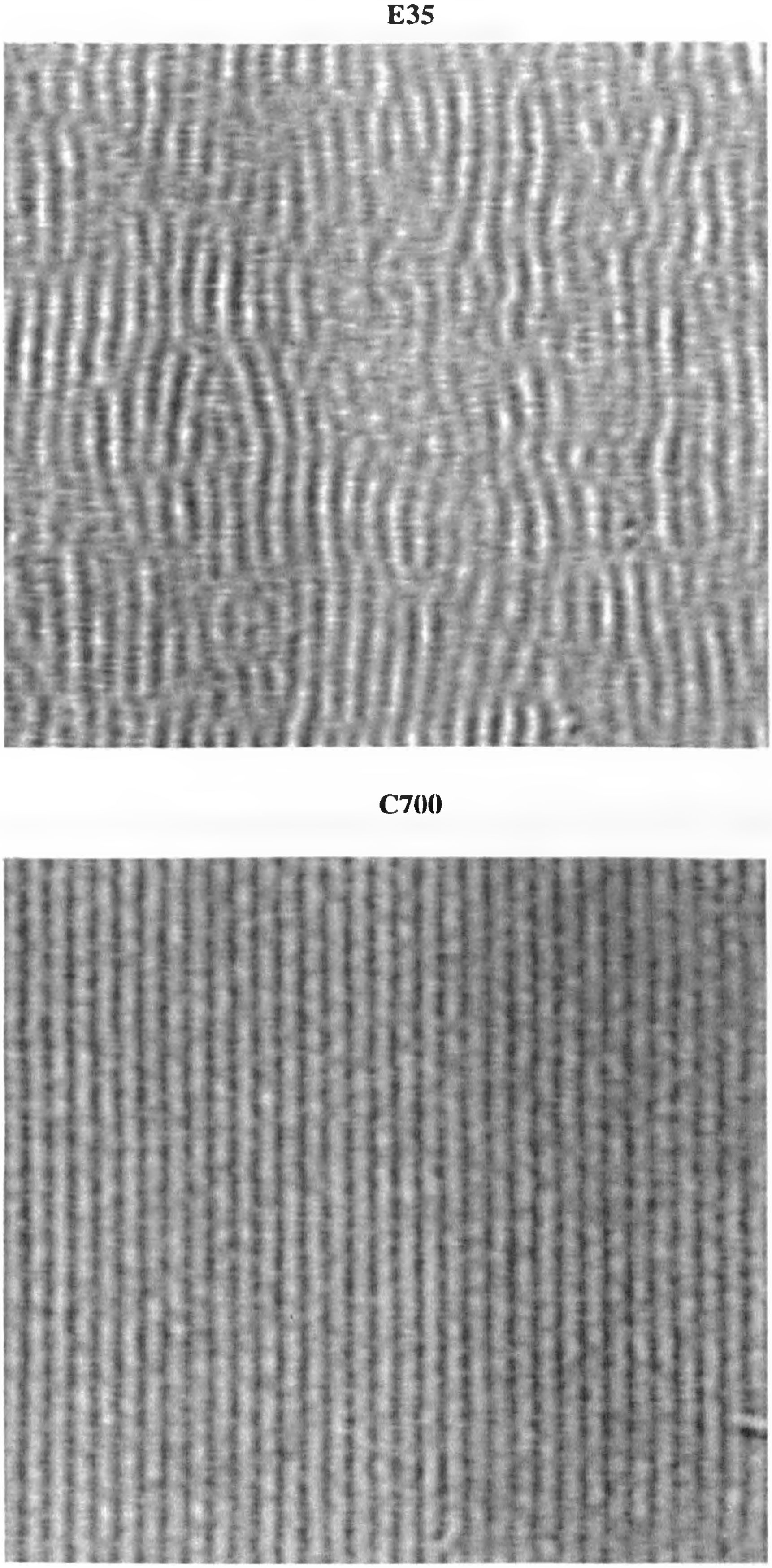

E35

C700

Figure 4-15. Typical processed lattice-fringe images from fibres E35 and C700

4. 3. 3. General discussion of lattice imperfections

As reviewed previously, Park considered that the disorder in carbon fibres consists of both inter- and intra-crystallite disorder, which may be determined from the X-ray data [72]. The present work suggests that the intra-crystallite disorder (referred to as lattice imperfection) can be further characterized by inter-plane imperfections and plane imperfections. The inter-plane imperfections correspond to structural defects between layer planes, and have been quantified by changes in interlayer spacing. On the other hand, the plane imperfections have been quantified in terms of tortuosity (meandering of lattice fringes). Moreover, the local misorientation of layer planes reflects the plane imperfections as the variation of local orientation is due to the meandering of layer planes.

There appears to be continuous structural transitions between lattice imperfection and perfection. Graphitic ordering proceeds by a gradual increase in correlation between layers (decrease of interlayer spacing) and a straightening of the layers (decrease of meandering and local misorientation of layer planes).

E35C

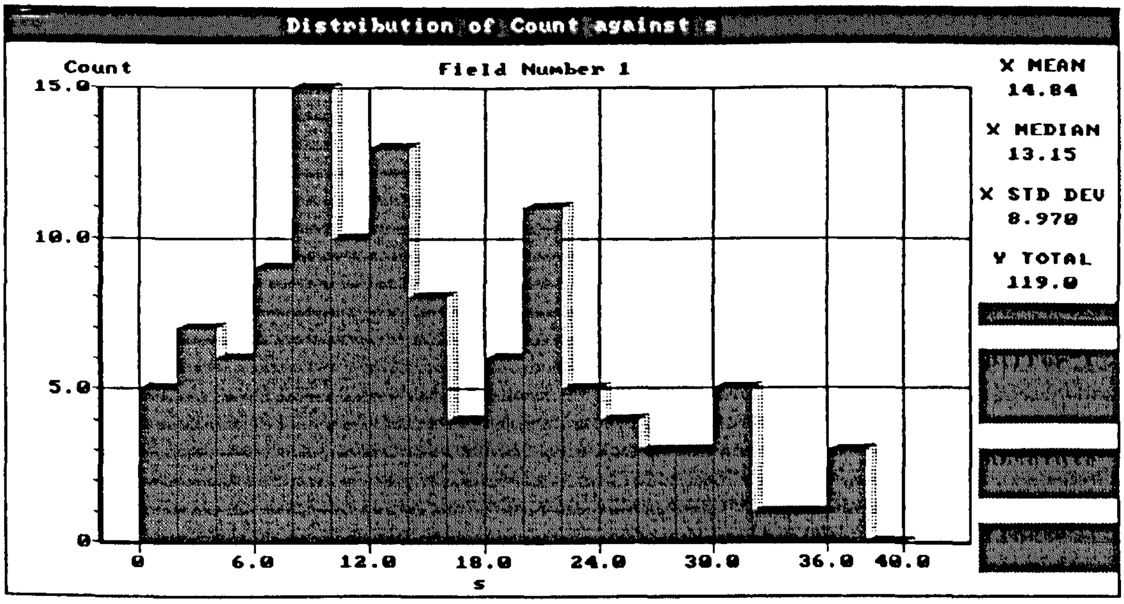

E35

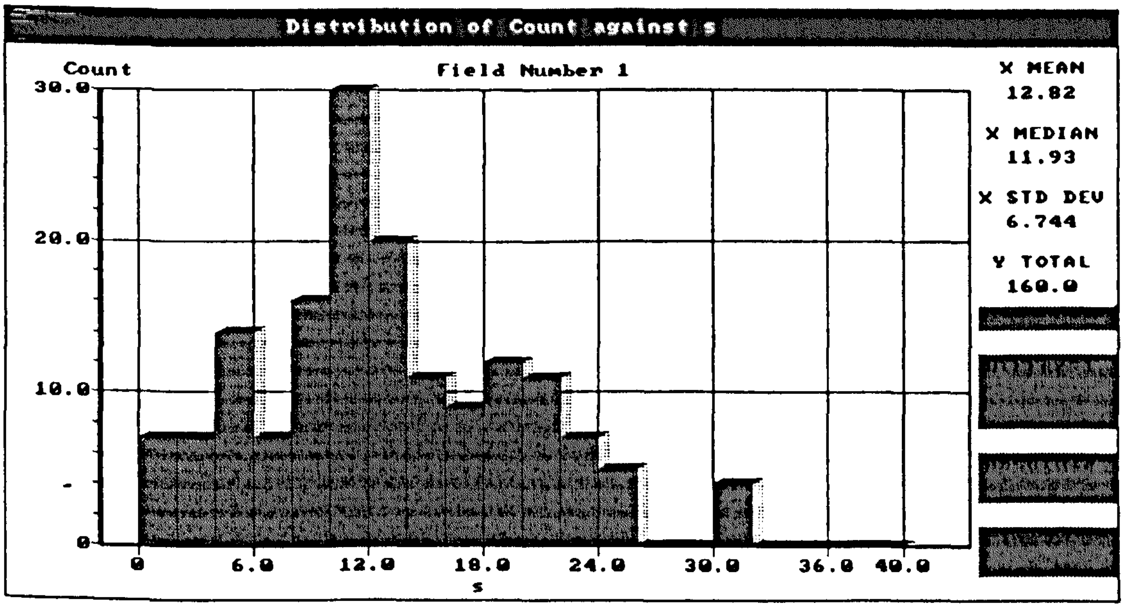

Figure 4-16. The distributions of tortuosity for carbon fibres : E35C, E35, E55, E75, E105, E120, E130 and C700

E55

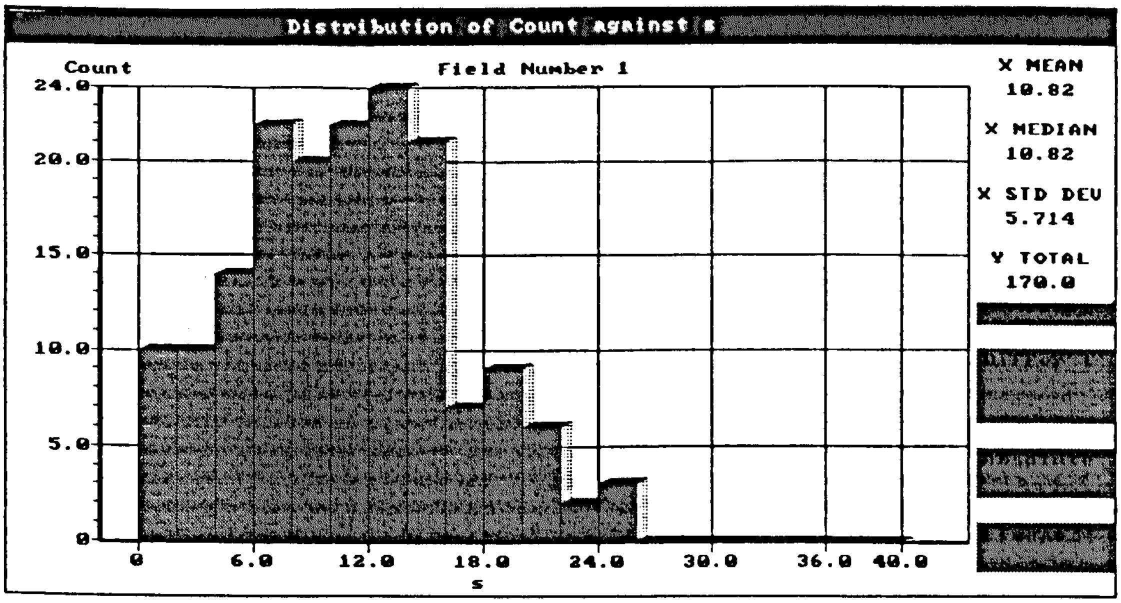

E75

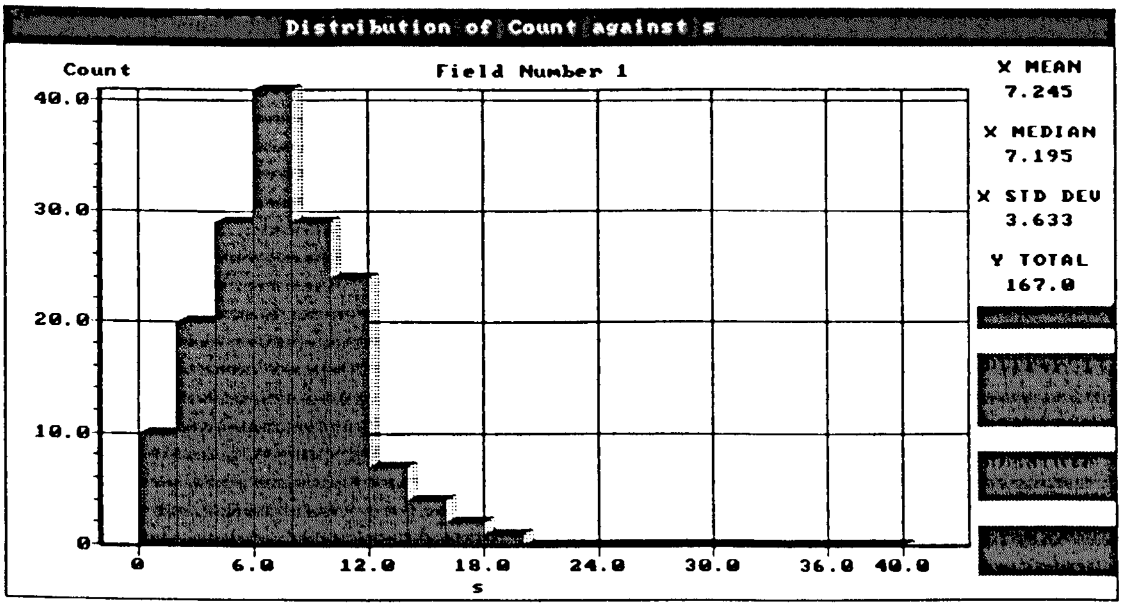

Figure 4-16. The distributions of tortuosity for carbon fibres : E35C, E35, E55, E75, E105, E120, E130 and C700

E105

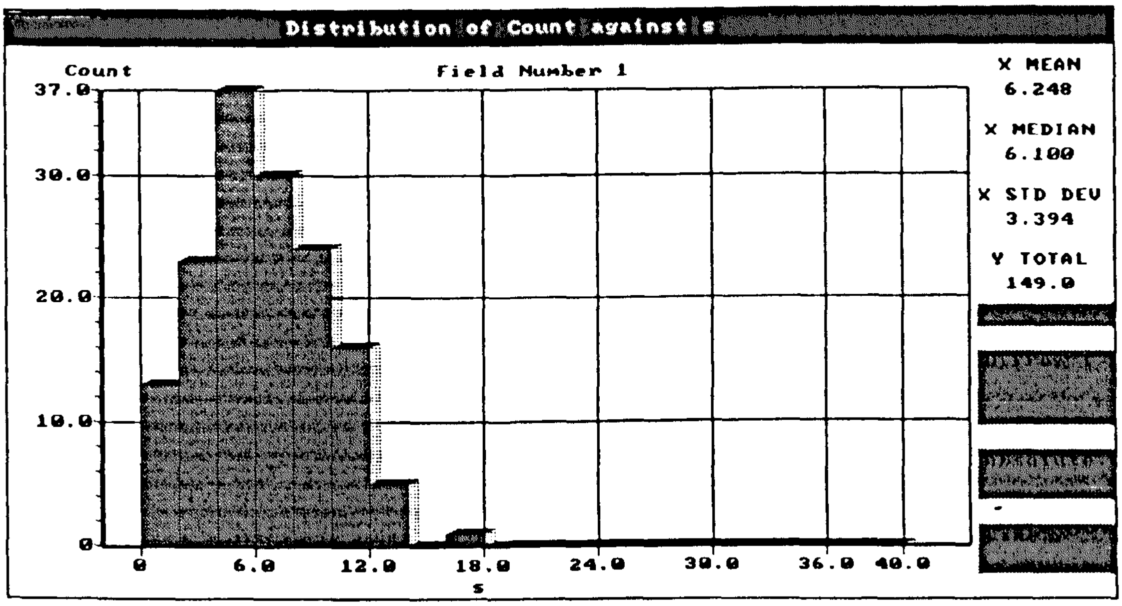

E120

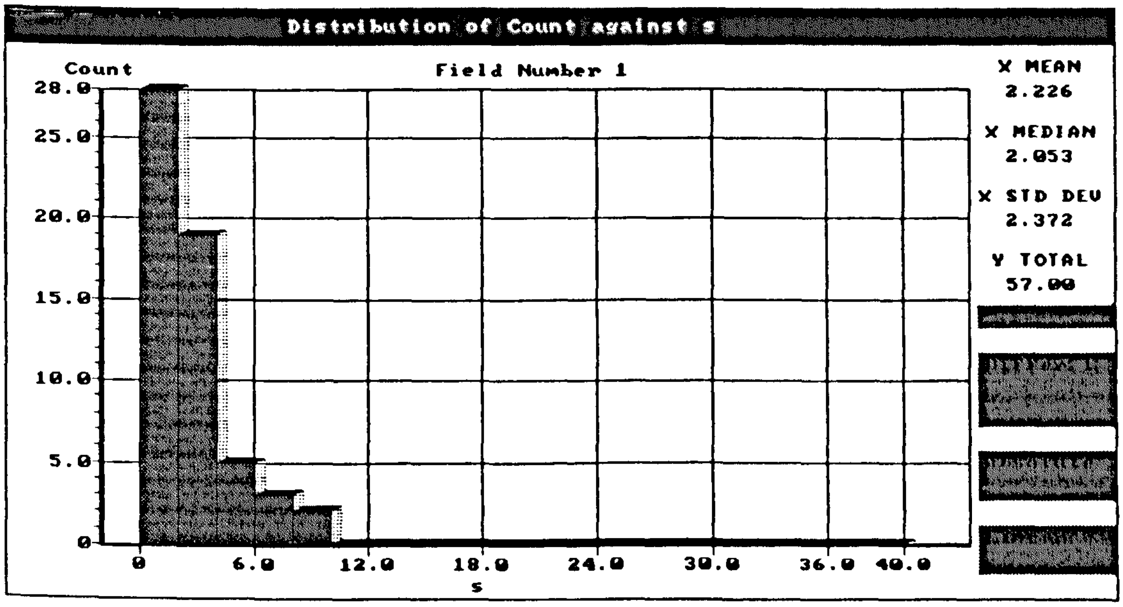

Figure 4-16. The distributions of tortuosity for carbon fibres : E35C, E35, E55, E75, E105, E120, E130 and C700

E130

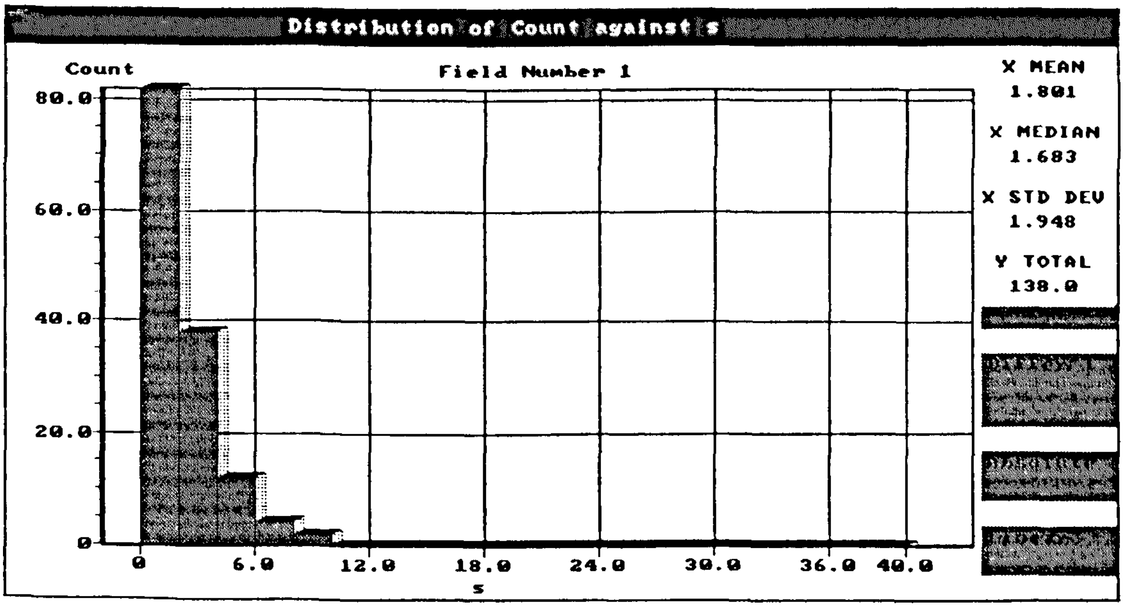

C700

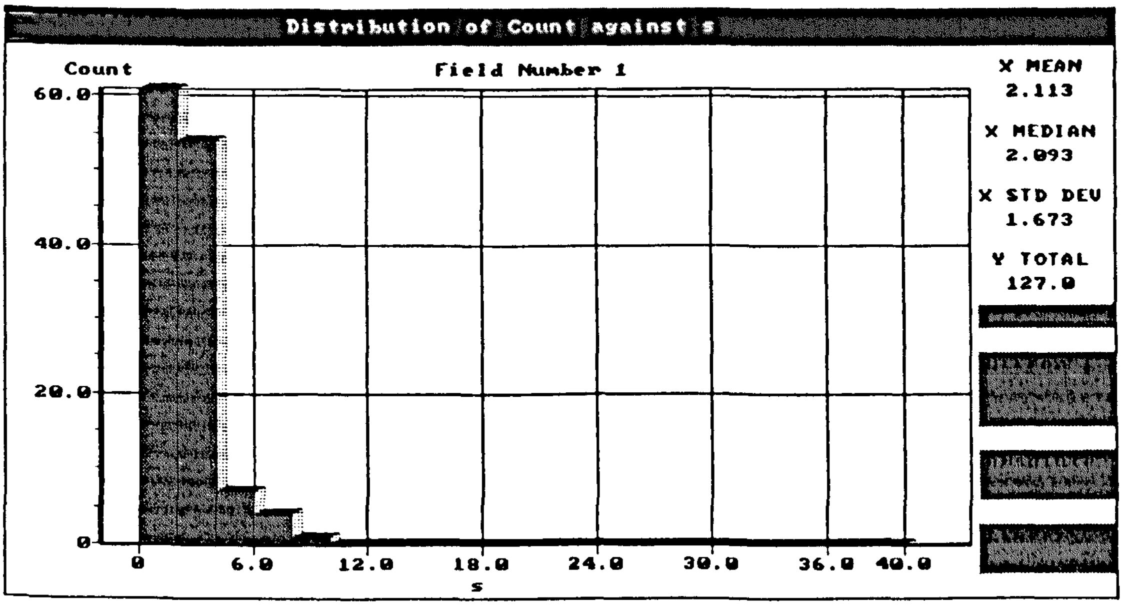

Figure 4-16. The distributions of tortuosity for carbon fibres : E35C, E35, E55, E75, E105, E120, E130 and C700

Chapter 5

Compressive Properties of MP-based Carbon Fibres

5. 1. Introduction

It is well known that the compressive strengths of carbon fibres are significantly lower than their tensile strengths [63]. Moreover, compared with PAN-based carbon fibres the MP-based fibres tend to have a lower compressive strength. Since such relatively poor compressive strength is a major limitation to the wide application of carbon fibre composites, recently a number of studies has been focused on understanding the compressive behaviour of carbon fibres. Such studies have been mainly reviewed in Chapter 1 (see section 1. 5. 2.).

As indicated in Chapter 1, the present work is focused on relating the compressive strengths to the structures of carbon fibres. As reported in Chapter 3 and 4, the structures of a series of Du Pont MP-based carbon fibres have been investigated and a number of structural parameters have been measured. In this Chapter, the compressive strengths and failure characteristics of this series of carbon fibres have been studied. The tensile recoil test [86], which was described in Chapter 2, has been used to measure the compressive strengths of the fibres. After testing, the specimens were observed in a scanning electron microscope (SEM) in an attempt to develop the failure mechanisms.

5. 2. Compressive strength

The compressive breaking stresses (strengths) of a range of MP-based carbon fibres, determined from the probability-plots of the tensile recoil tests (shown in Figure 5-1), are listed in table 5-1, together with fibre diameters, average cross-sectional areas of the fibres and the manufacturers' supplied tensile data. The compressive strength of fibre C700 was not determined since insufficient data was collected owing to their extreme brittleness and resulting fracture when attempting to separate and mount them individually.

As indicated in Chapter 3, the cross sections of fibres E35C are either circular or of the missing sector type. For recoil testing the type of fibre cross section was not determined, consequently the compressive stress has been reported in terms of a range of values according to the areas of both types of section.

Table 5-1. Mechanical properties of MP-based carbon fibres

Fibres	Diameter (μm)	Cross-Sectional Area (μm²)	Compressive Breaking Stress (GPa)	Tensile Modulus (GPa)	Tensile Breaking Stress (GPa)	Tensile Breaking Strain (%)
E35	8.83(0.37)	61.2	0.82	224	2.38	1.02
E55	8.91(1.15)	62.4	0.78	374	3.05	0.74
E75	9.24(0.63)	67.1	0.67	490	2.92	0.58
E105	9.27(0.82)	67.5	0.61	750	3.10	0.48
E120	8.82(0.60)	61.0	0.57	857	3.19	0.44
E130	8.33(0.55)	54.5	0.63	905	3.59	0.48
E35C	----	72.7(9.79) (sectored) 54.8(4.08) (circular)	0.77~1.03	237	2.54	1.02

Notes: The data in the bracket is the standard deviation of corresponding parameter.

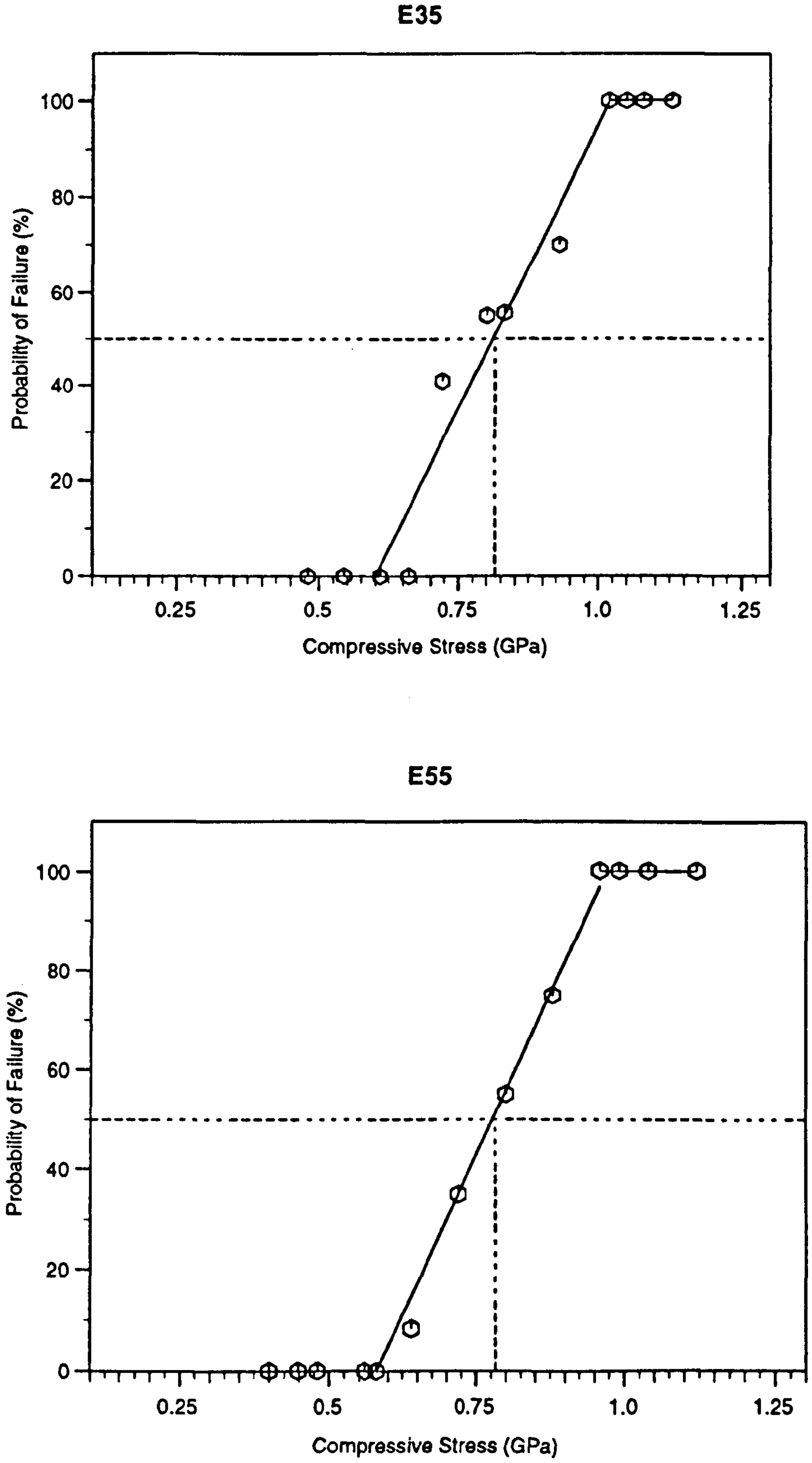

Figure 5-1. The probability-plots of the tensile recoil tests for fibres E35, E55, E75, E105, E120, E130, and E35C.

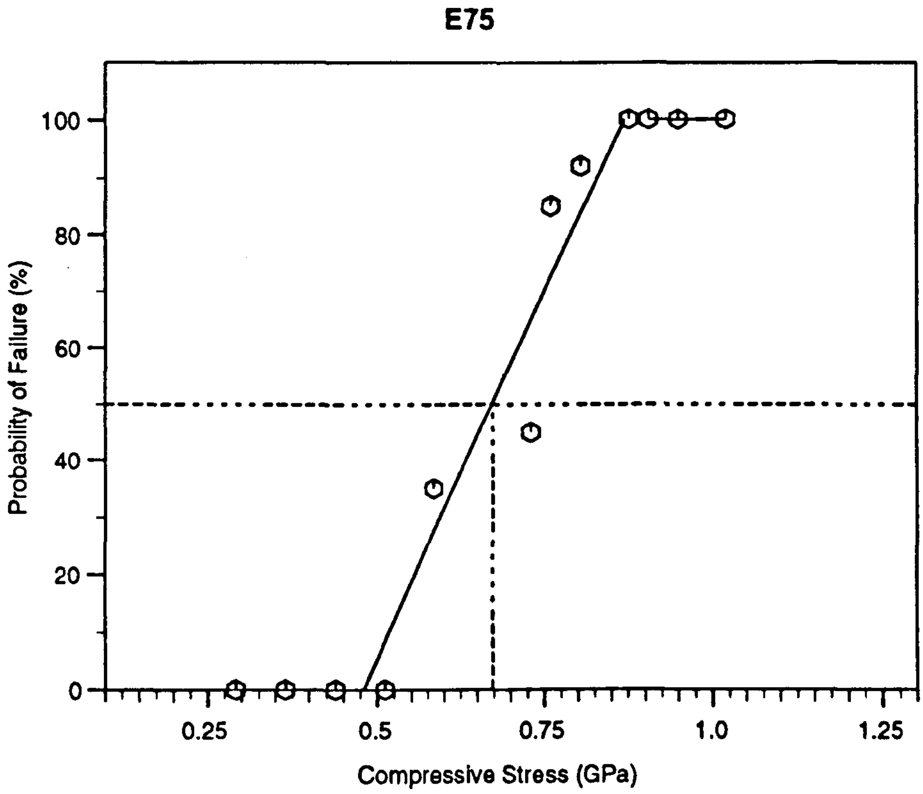

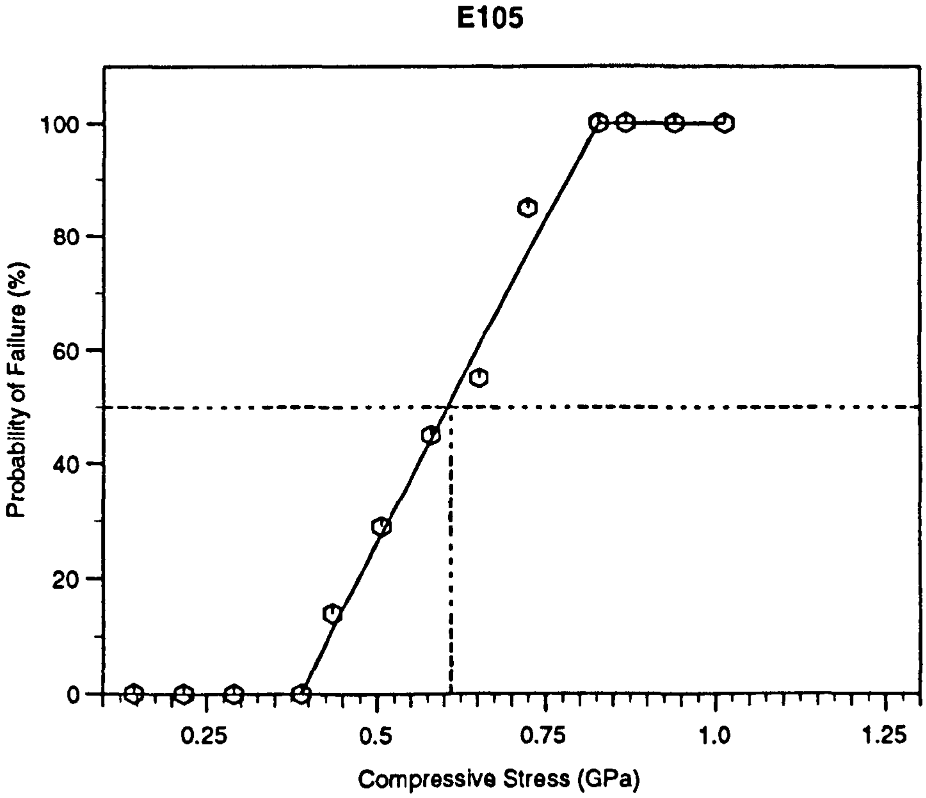

Figure 5-1. The probability-plots of the tensile recoil tests for fibres E35, E55, E75, E105, E120, E130, and E35C.

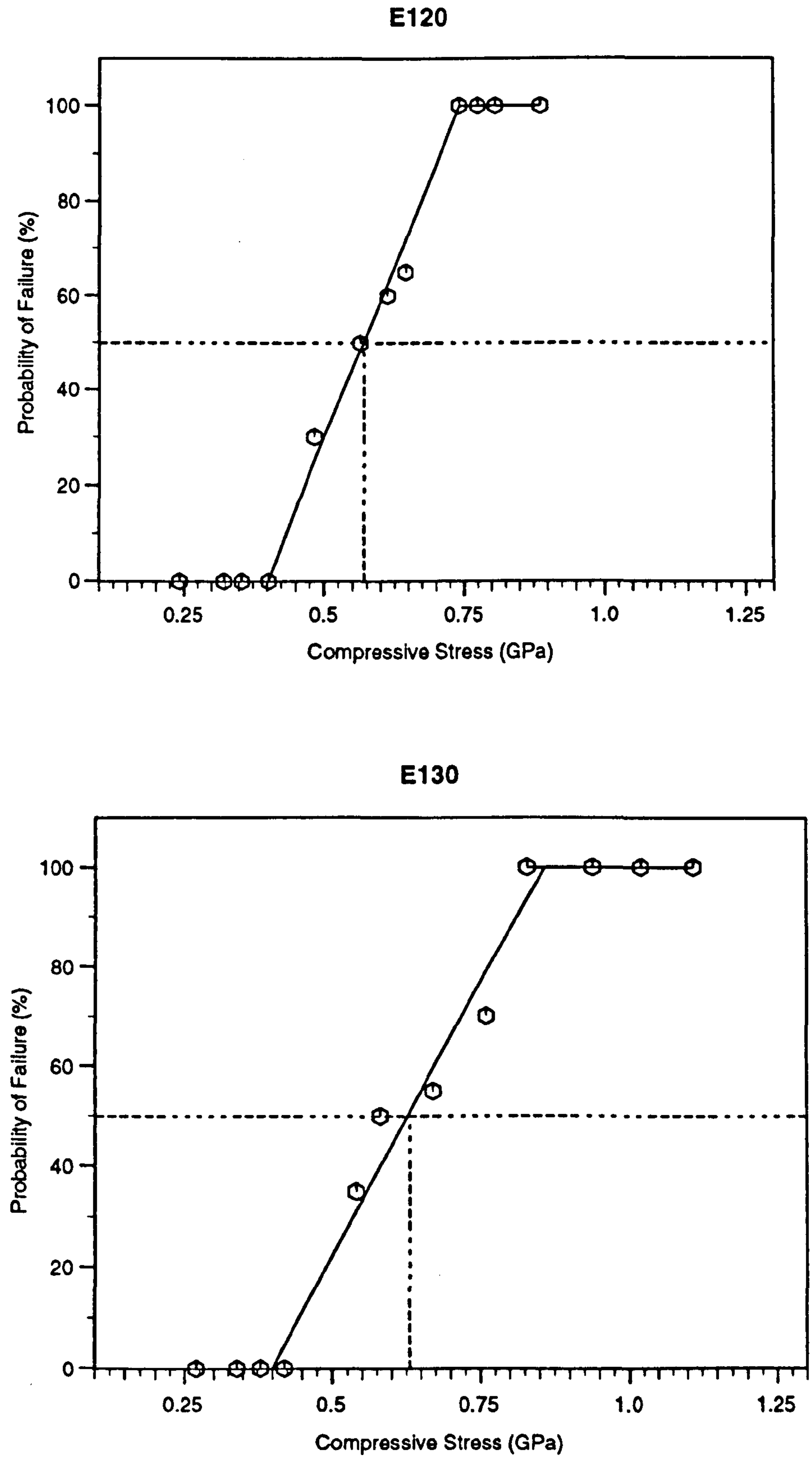

Figure 5-1. The probability-plots of the tensile recoil tests for fibres E35, E55, E75, E105, E120, E130, and E35C.

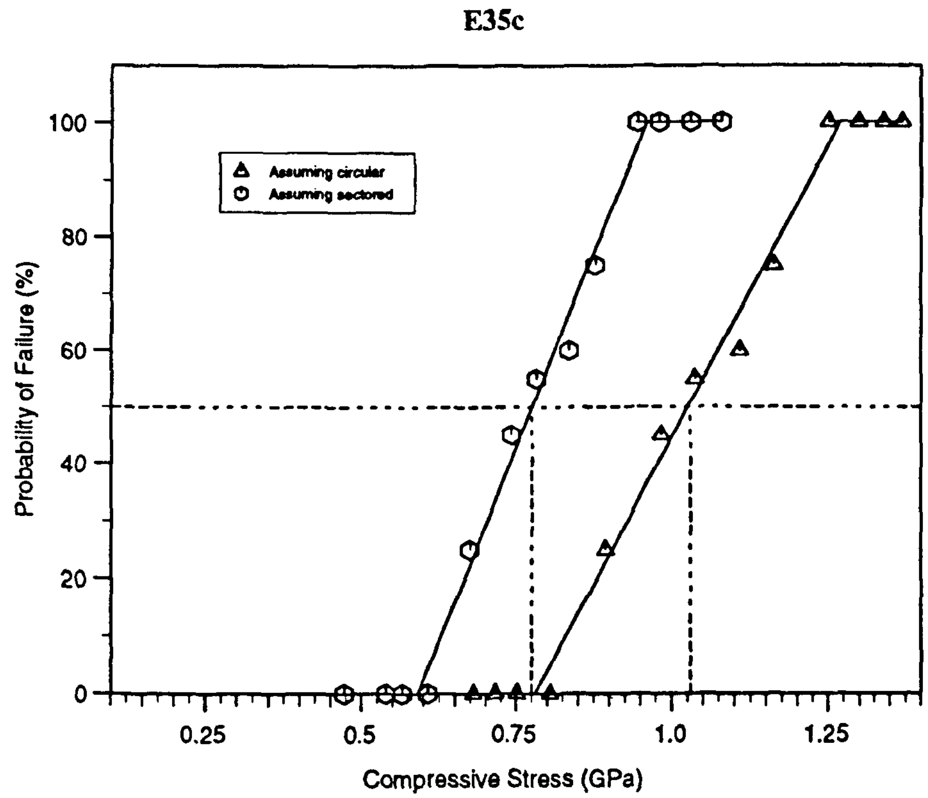

Figure 5-1. The probability-plots of the tensile recoil tests for fibres E35, E55, E75, E105, E120, E130, and E35C.

As shown in Figure 5-2, it is clear that generally there is a tendency for the compressive breaking stress of MP-based carbon fibres to decrease with increasing tensile modulus. As can be seen in Figure 5-3, as tensile breaking strain increases, the compressive breaking stress increases continuously and then tends to level out at approximately 0.75% strain. This overall result is in agreement with the findings of Park [72] who suggested that increasing disorder of carbon layers permits large localized deformation hence higher tensile strain and improved compressive strengths. However this does not account for the observed levelling off of the compressive strength when the tensile strain is greater than about 0.75%.

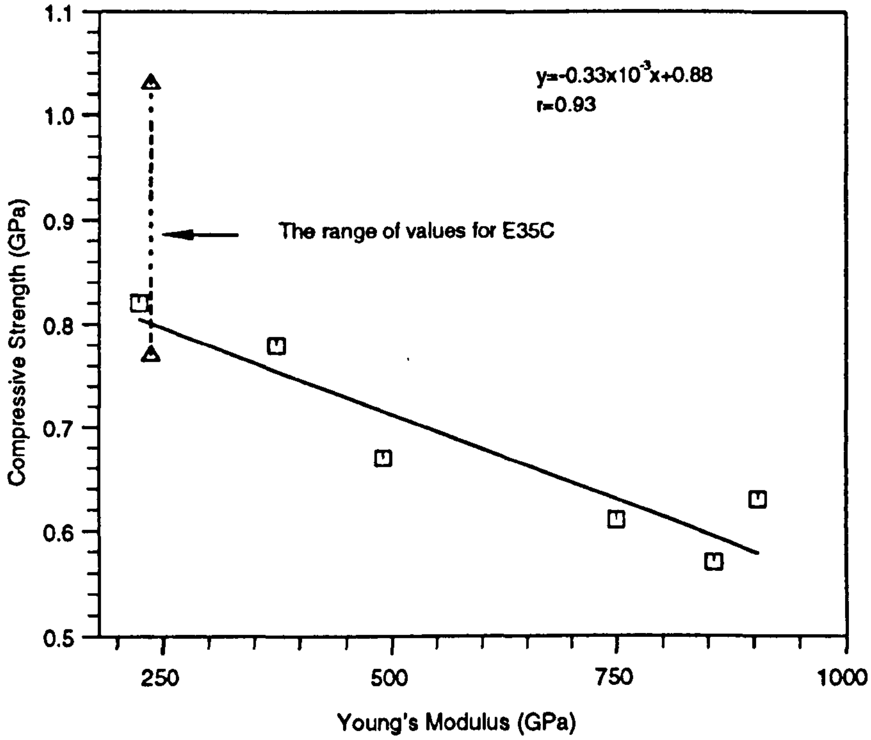

Figure 5-2. Compressive strength as a function of Young's modulus for Du Pont MP-based carbon fibres

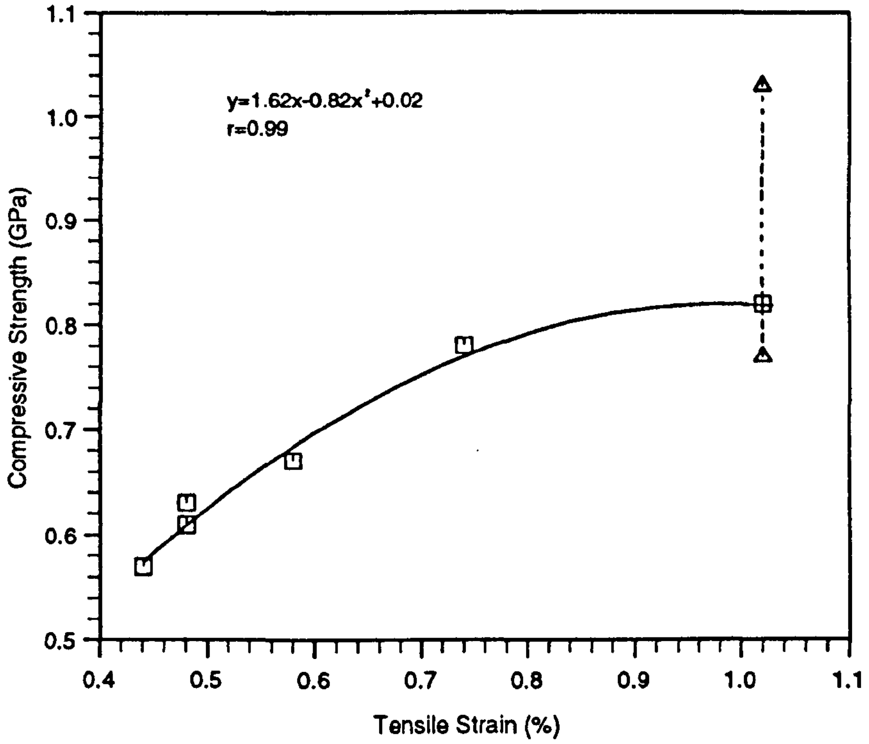

Figure 5-3. Compressive strength as a function of tensile strain for Du Pont MP-based carbon fibres

The compressive strength of fibre E35C lies between 0.77 *GPa* and 1.03 *GPa*. Since SEM observations of the failure surface revealed that most of the tested fibres had a circular cross section, it is tempting to suggest that the true value lies near to 1.03 *GPa*. Thus there is a good possibility that the compressive strength of fibre E35C is superior to that of fibre E35 which has a similar tensile modulus and strain level. The previous structural studies (Chapters 3 and 4) indicated that the degree of disorder for fibre E35C is higher than that for fibre E35. In addition, there is a possibility that the radial layers might be further folded about the fibre axis depending on the interpretation of the distinctive dark-field image of E35C (see section 3.2.1.1). Such structural features could presumably account for the apparent increase in compressive strength.

It was suggested that in the case of MP-based carbon fibres the compressive strength decreases with increasing tensile strength [72]. However, from the present work it is difficult to draw any firm conclusion about such a relationship. This might suggest that the main factors governing the tensile properties differ from those governing the compressive properties. For example the presence of flaws is the main reason for the tensile failure of carbon fibres [57,58] but there is no evidence showing that axial compression fracture is associated with gross fibre flaws in this work or in other previous work.

5. 3. Compressive failure characteristics

After recoil testing, regions of the fibres anchored to the card-holder were observed in the SEM. Typically, the compressive failure mode for Du Pont higher modulus fibres is classical shear at an angle of 45^0 to the fibre axis which supports the findings of Park *et al.* working on the Thornel series. As shown in Figures 5-4a and b, well defined shear bands can be observed evenly distributed along short regions of the fibres adjacent to the anchoring point in the card-holder. On the other hand, however, the failure bands of compressed fibres of moderate modulus (E55 and E75) shown in Figure 5-4c tends to be irregular with no sharply defined shear angle. It was also observed that for the lower modulus fibres E35 and E35C, there were no kink bands appearing in the region anchored to the card-holder. Thus there is a tendency that moderate and lower modulus fibres have a resistance to classical shear failure.

Although the failed regions observed near the anchor points on the card-holder indeed change from irregular to well defined oblique kink bands with increasing tensile modulus of fibres, the recoil-fracture faces (away from the card support) all show similar characteristics. As shown in Figure 5-5, each face consists of two distinct areas namely : (1) a relatively smooth oblique region, and (2) a larger generally transverse but very irregular region. Such features suggest that failure is not due to purely uniaxial compression but to a complex mechanism involving a bending component. In this way the smooth region may originate from the compressed zone (shearing) whilst the more irregular region arises from tensile deformation.

5. 4. Compressive failure mechanism

As indicated previously, under the recoil compressive loading the higher modulus MP-based carbon fibres (E105, E120, E130 and C700) failed in the anchored region typically due to a shear deformation. On the other hand, however, where the fibres were not supported, failure occurred due partly to bending. The possible mechanism is shown in detail in the schematic diagram Figure 5-6.

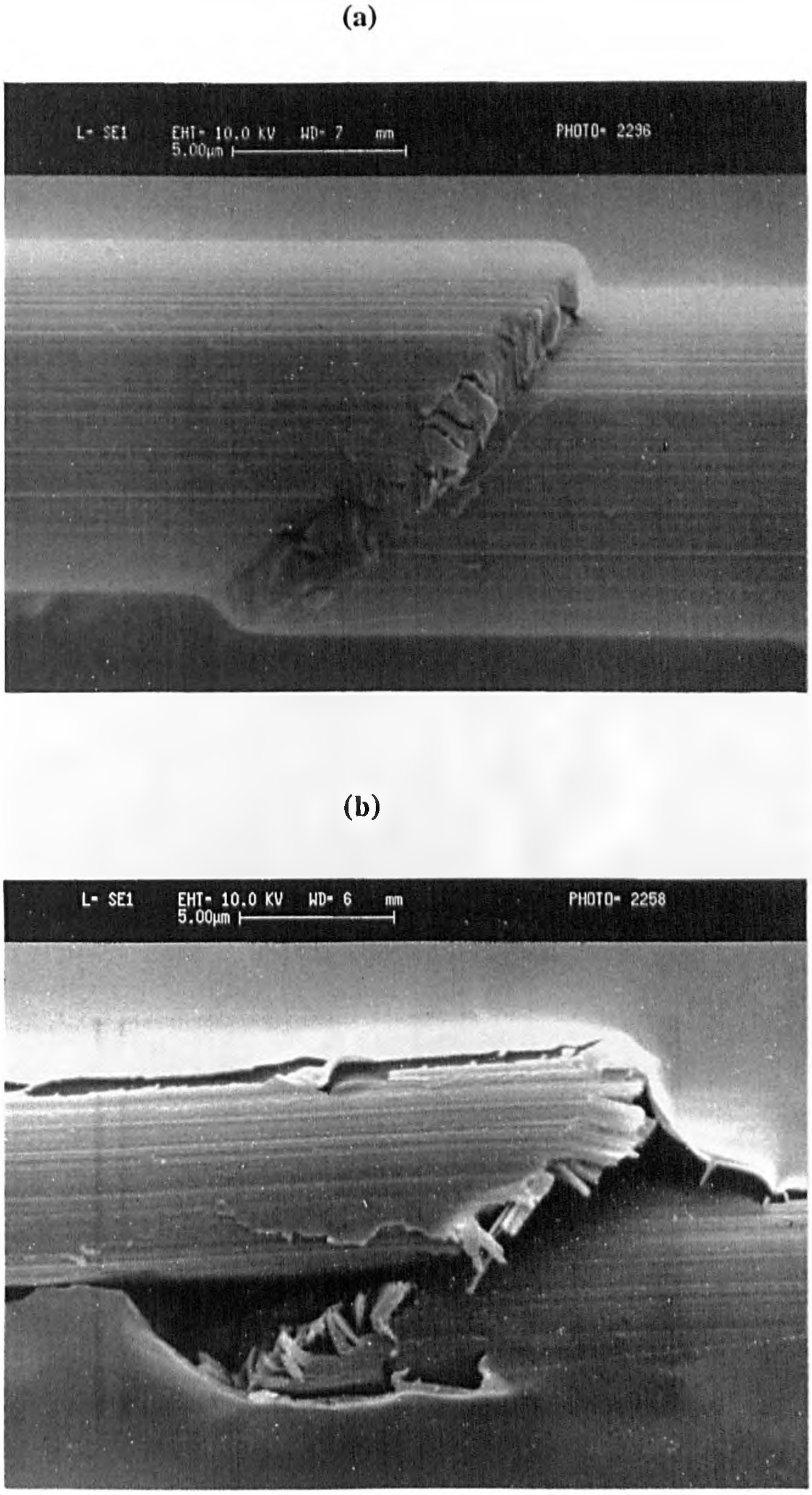

Figure 5-4. Compressive failure modes of supported MP-based fibres, (a,b) well defined kink bands observed for high modulus fibres (>750 *GPa*), (c) irregular fracture faces observed for moderate modulus fibres (300~500 *GPa*).

(c)

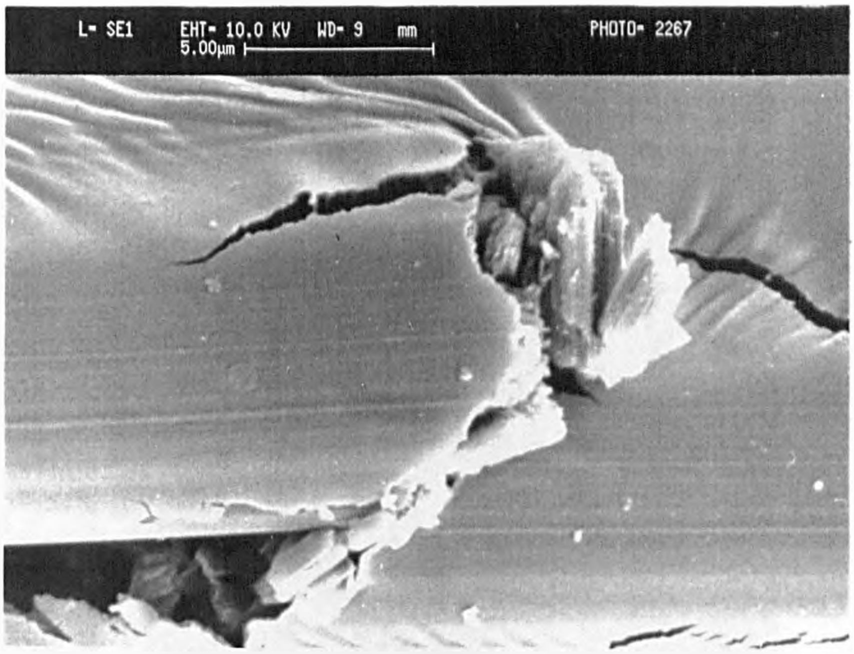

Figure 5-4. Compressive failure modes of supported MP-based fibres, (a,b) well defined kink bands observed for high modulus fibres (>750 *GPa*), (c) irregular fracture faces observed for moderate modulus fibres (300~500 *GPa*).

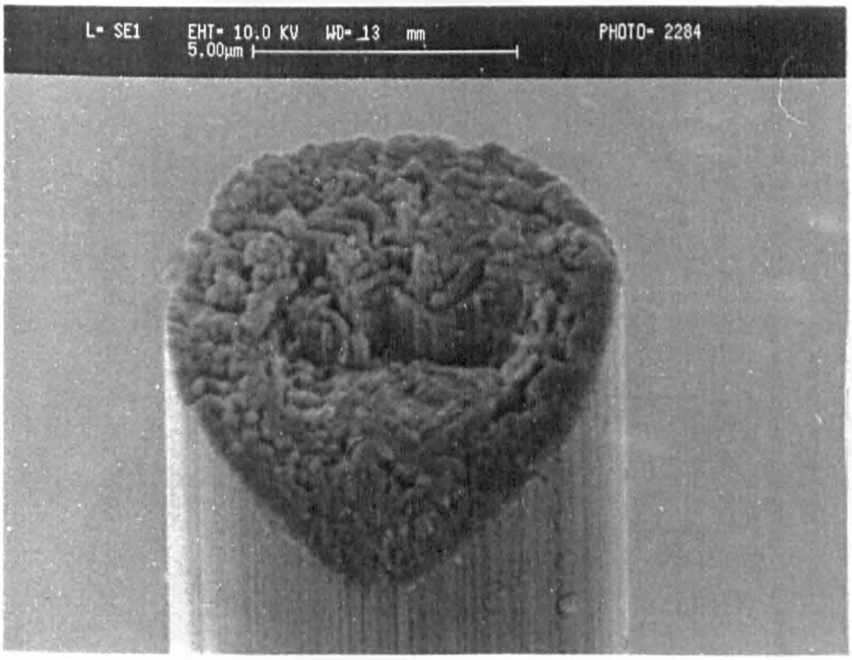

Figure 5-5. A typical recoil-failure face of Du Pont MP-based carbon fibres.

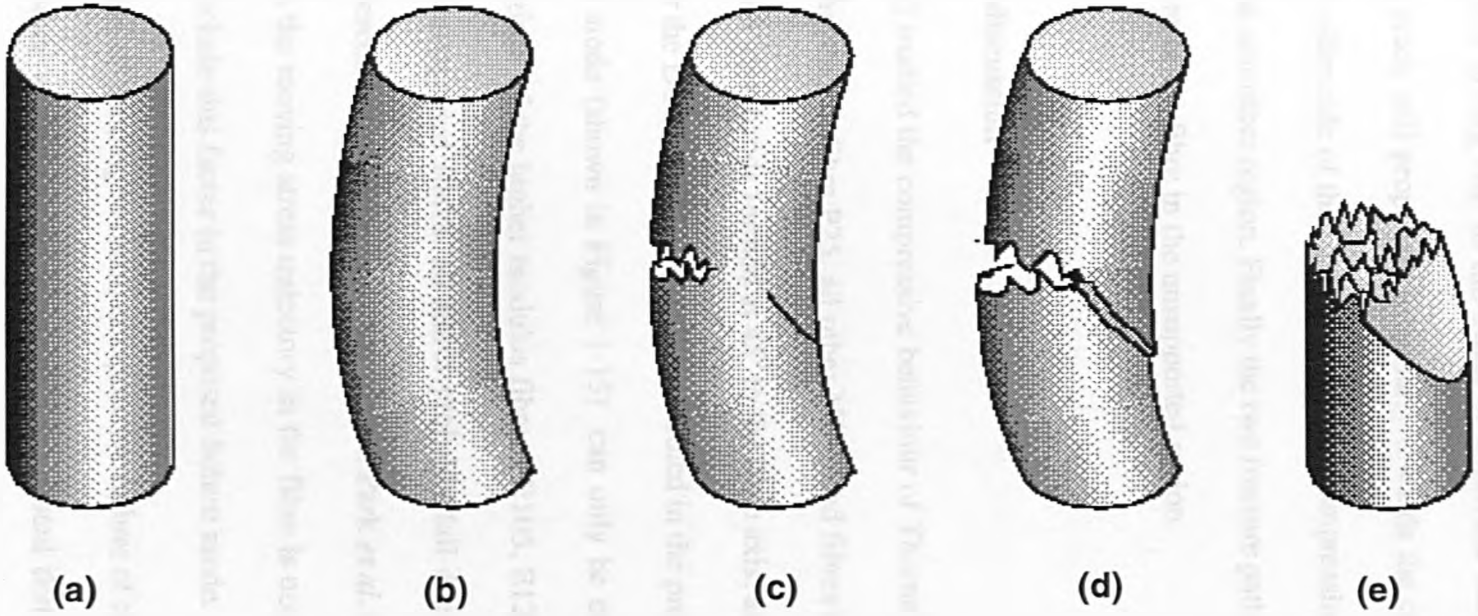

Figure 5-6. Mechanisms of compression failure of MP-based carbon fibres. (a) a fibre under the recoil force, (b) slight bending of the fibre, (c) initial crack in tension surface, with shear stress in compression region, (d) tensile crack propagation and intersection with shear kink band, (e) a recoil-failure face consisting of two distinct areas.

The originally straight fibres, after recoil, bend slightly in an unsupported region. It is proposed that in the outermost region of the extended side, the tensile breaking extension is exceeded giving rise to the onset of a surface crack. As the deformation proceeds, this crack will propagate irregularly towards the centre of the fibre. At the same time, the other side of the fibre will undergo compression leading to shear failure indicated by the smoother region. Finally the two fracture paths will intersect leading to complete failure of the fibre in the unsupported region.

5. 5. General discussion

Park *et al.* [72] studied the compressive behaviour of Thornel MP-based carbon fibres and claimed that except fibre P25, all other MP-based fibres deform by a simple shear mechanism with kink bands formed at 45^0 to the fibre axis, and then fracture along the kink band. For the Du Pont MP-based fibres studied in the present work, it appears that Park's failure mode (shown in Figure 1-15) can only be observed in the supported (anchored) regions of the higher modulus fibres (E105, E120, E130, C700), while in the cases of unsupported fibres, all fibres probably fail due to combined tensile and compressive forces arising from bending. In fact, Park *et al.* also indicated that during the recoil test, the moving stress trajectory in the fibre is not purely uniaxial although they did not include this factor in the proposed failure mode.

The contribution of bending to recoil compressive failure of carbon fibres has also been reported by other workers. Edie *et a*l. [67] suggested that during the recoil test, a macroscopic lateral displacement may result due to the dimensions of the test specimen (Euler bending) and the amplitude of this displacement wave has an inverse relationship with fibre tensile modulus. Therefore they considered that only low-modulus MP-based fibres exhibit a combined tensile and compressive failure mode, while high-modulus fibres exhibit a simple shear failure mode. However, they found that most failed Du Pont fibres (all modulus ranges) exhibited almost transverse flat failure faces. This suggests that both low- and high-modulus Du Pont fibres do not fail by a simple shear deformation in recoil testing. Indeed the present study is in accord with these findings.

Jiang *et al.* [112] measured the compressive strengths of PAN-based carbon fibres at different gauge lengths using tensile recoil testing and found that with increasing gauge length, the observed recoil compressive strength decreased. They believed that the observed decrease is the consequence of higher bending-induced stresses at longer gauge lengths rather than the result of a "weak link" mechanism operating in the case of tensile testing. Therefore it is clear that due to the fibre bending the measured recoil compressive strength might be smaller than the axial compressive strength of those fibres at the corresponding gauge length.

It is very likely that the method used to initiate the recoil process causes variations in the degree of fibre bending, and thus influences the measured compressive strength at the same gauge length. As shown in table 5-2, generally the recoil compressive strengths obtained using the mechanical initiation technique (cutting with scissors) are lower than those obtained using the electrical initiation technique (electrical spark) for the same fibre samples. Presumably, the degree of fibre bending caused by the electrical initiation technique tends to be lower than that caused by the mechanical initiation technique. Therefore, the measured recoil compressive strengths of fibres can only be compared if the measurement is carried out using the same gauge length and

Table 5-2. Comparison of compressive strengths obtained by the mechanical initiation and electrical initiation techniques

Fibres	Compressive Strengths (GPa)		Young's modulus (GPa)
	Mechanical initiation †	Electrical initiation ✣	
Du Pont fibres			
E35	0.82	1.6	224
E55	0.78	1.1	374
E75	0.67	1.1	490
E105	0.61	0.8	750
E120	0.57	0.7	857
E130	0.63	0.5	905
Thornel fibres			
P25	0.9	1.4	140
P55	0.5	0.8	380
P75	0.5	0.8	500
P100	0.4	0.5	690
P120	0.3	--	820

† Recoil compressive strengths of Du Pont fibres (E35~E130) come from the present investigation, and recoil compressive strengths of Thornel fibres (P25~P120) are from Park *et al.* [72].

✣ Recoil compressive strengths of both Du Pont and Thornel fibres come from Edie *et al.* [67].

All Young's modulus data are from manufacturer.

same initiation techniques.

As shown in table 5-2, compared with Thornel fibres, Du Pont MP-based fibres generally have higher compressive strengths at all modulus levels. Moreover, as can be seen from Figure 5-7, the plot of compressive strength vs Young's modulus is less steep for Du Pont pitch-based fibres than for Thornel fibres. For example, when the fibre Young's modulus increases from about 200 *GPa* up to 800 *GPa*, the compressive strength decreases from about 0.8 *GPa* (for both types of fibres) down to 0.3 *GPa* for Thornel fibres (63% loss) and 0.6 *GPa* for Du Pont fibres (25% loss). It is evident therefore that the factors determining high modulus do not necessarily limit the compressive strength. Clearly a comparison of the structures of Thornel and Du Pont fibres should allow elucidation of the matter.

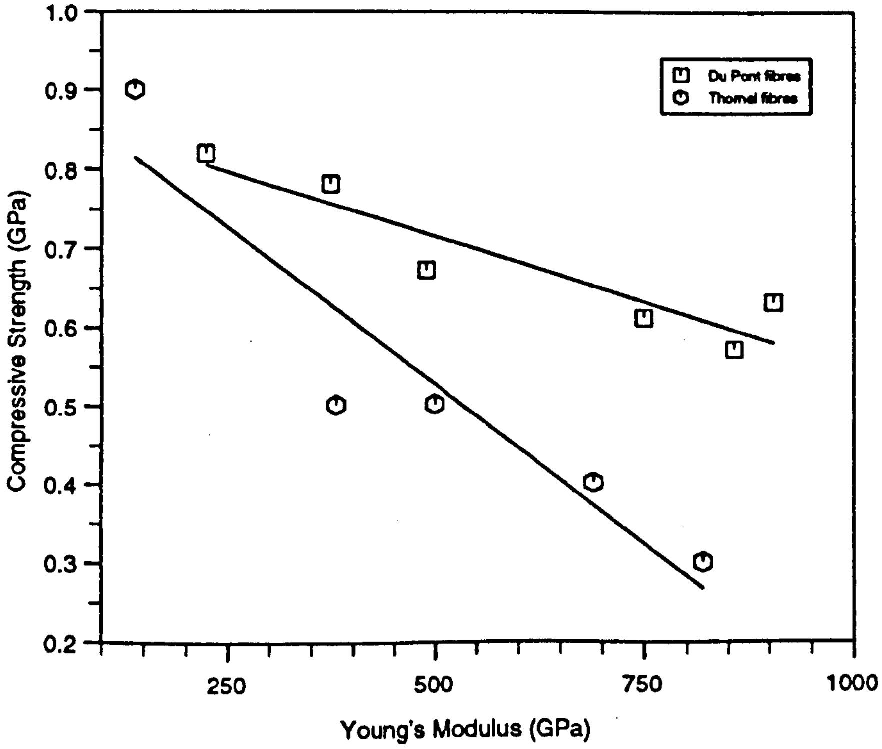

Figure 5-7. Compressive strength as a function of Young's modulus for Du Pont and Thornel MP-based carbon fibres respectively.

In regard to the overall structure difference between Du Pont and Thornel fibres, it is known that Thornel fibres exhibit flat layer textures [72] while Du Pont fibres exhibit folded-radial textures (Chapter 3). It is very likely, as explained below, that the folded-radial texture tends to inhibit shearing of the basal planes and hence gives rise to comparatively higher compressive strengths.

The possible mechanisms accounting for the folded-radial texture inhibiting shear deformation can be explained as follows. Presumably, the highly folded-radial layer planes (lower modulus fibres) tend to reflect a relatively high degree of disorder in the microstructure which would give a high resistance to shear between the basal planes by permitting localized deformation and thus a comparatively high compressive strength. Moreover, it is clear that an initial microcrack would be expected to propagate more slowly across the folded layer planes (i.e. crack deflection) than across well packed flat layer planes. As folding of the layer planes becomes less marked (i.e. less disorder, increasing modulus) there will be a tendency for the compressive strength to decrease. Northolt [68] believed that increased cross-linking between the graphite planes by sp^3-sp^3 bonding causes an increase in shear modulus and hence an increase in compressive strength. Since graphitization will reduce the number of sp^3 bonds considerably, high modulus fibres tend to have a lower compressive strength. The possibility of sp^3 bonds in carbon fibres was postulated early by Jenkins [113] and confirmed late by Fitzer from Raman spectroscopic work [114]. It was reported that a consequence of increased sp^3 bonding is reflected by increased interlayer spacing d_{002} and decreased crystallite size L_c and L_a. Such a situation is compatible with the findings of the present work where disorder and compressive strength appear to be directly related.

It is interesting to notice that of the Thornel fibres, P25 has much the highest compressive failure stress (0.9 *GPa* for mechanical initiation and 1.4 *GPa* for electrical initiation). The structural studies revealed that P25 fibre does not exhibit any flat layer structure, but possesses a randomly organized texture rather like PAN-based fibres. In addition, P25 has the highest amount of disorder (as measured by X-ray studies) of all the Thornel series of fibres. Such structural features are assumed to account for the exceptional high compressive strength of P25 fibre.

Chapter 6

The Relations between Structure and Compressive Strength

The macro- and micro-structures of Du Pont MP-based carbon fibres were studied using SEM, TEM, X-ray diffraction and image analysis techniques, and were discussed in Chapters 3 and 4. Also, the fibre compressive strengths have been measured using the tensile recoil method, and compression failure mechanisms have been proposed in Chapter 5. It is the purpose of this chapter to discuss the relationship between the structure and compressional properties of MP-based carbon fibres, in an attempt to identify the structural factors which govern the compressive strength.

6. 1. Macrostructure and compressive strength

The influence of macrostructure on compressive strength has been studied previously [64, 65]. Generally it was agreed that fibres containing sheet-like, flat-layer structures tend to be less resistant to shear between the basal planes and hence to have a relatively low compressive strength. This effect will become more evident later when fibres with different macrostructure are compared.

Based on the results described in section 3.1, it is known that all Du Pont MP-based fibres are characterized with folded pseudo-radial layer planes. However, according to Park *et al.* [72] most of Thornel fibres exhibit well organized flat layer structure except for fibre P25 (which exhibits an almost random structure similar to that of PAN-based fibres). Subsequently when a comparison is made between these two series of fibres, it is found that the compressive strengths of Du Pont fibres are higher than those of the Thornel fibres (of the same modulus level) and the discrepancy increases gradually with increasing Young's modulus as shown in Figure 5-7. As explained in Chapter 5, the folded layer planes are expected to be more resistant to shear between the basal planes than a flat layer structure, and therefore the fibre compressive strength is increased.

Edie [115] compared the fibres possessing a random macrostructure (Nippon Steel pitch-based fibres) again with Thornel fibres (flat layer structure) and found that the compressive strengths of Nippon Steel fibres are superior as shown in Figure 6-1. Therefore it appears that fibres with both folded and random structures tend to have a higher compressive strength than fibres with a flat layer macrostructure. Furthermore, in comparison with the compressive strength of PAN-based fibres which have an almost random structure, it is considered that MP-based carbon fibres with a random structure may have a higher compressive strength than MP-based carbon fibres with folded layer planes.

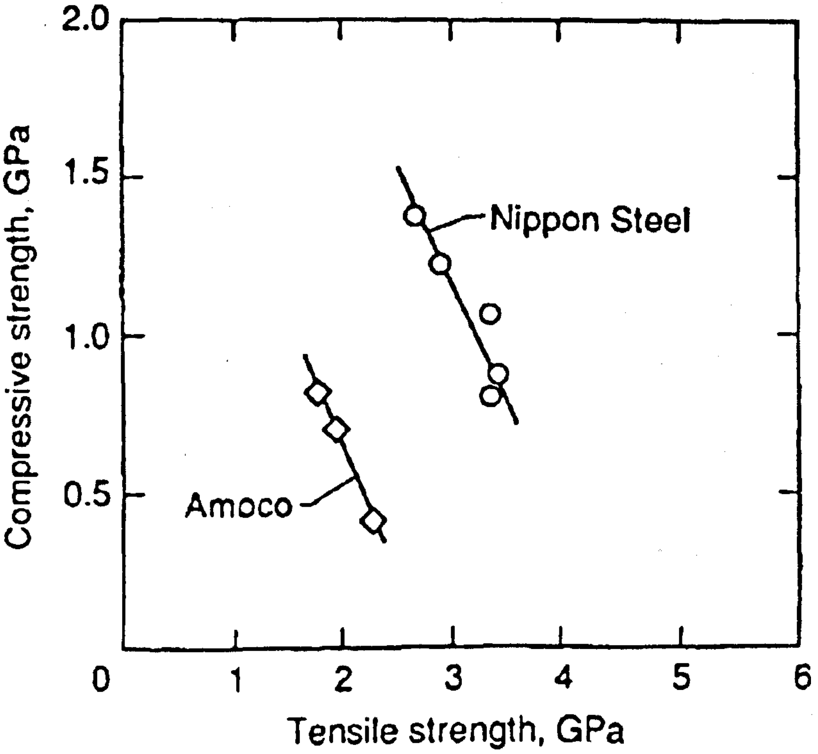

Figure 6-1. Compressive strength as a function of tensile strength for Nippon Steel and Amoco MP-based carbon fibres [115].

Generally, different macrostructures can be produced by disturbing the flow profile of the mesophase prior to extrusion [18]. For example, by stirring the pitch a random or an onion structure can be obtained depending upon the shape of the stirrer; while without stirring a radial structure forms. However, it is important to notice that the random structure across the fibre cross section does not necessarily mean the random arrangement along the fibre axis. In fact, the graphite layer planes are still well oriented parallel to the fibre axis. Thus the fibre Young's modulus can be maintained at a relatively high level.

The organization of layer planes into so called domain structures may also have an influence on the compressive strength. As indicated in Chapter 3, for Du Pont pitch-based fibres, it appears that the domains become more perfect and singular with increasing fibre Young's modulus. For example, the three domains exhibited by fibres E75 and E105 tend to develop into one single domain for fibres E120 and E130 which have the higher moduli in the series. Presumably, the formation of domains may be associated with wedge disclinations as described by White *et al.* [20]. Due to the disclinations, the layer planes tend to rearrange and so the overall direction in which the layer planes are oriented will vary from domain to domain. Consequently, when a crack propagates to the boundary of a domain, it is probable that it will change direction (crack deflection) and hence delay catastrophic failure. This would lead to an improvement in compressive strength.

Mochida *et al.* [49] suggested that the skin-core structure (a mosaic skin and an onion-like core), which can be introduced to MP-based fibres by moderately stabilizing and then carbonizing under strain, may also give a high compressive strength because the mosaic skin may withstand larger elongations than the core. However, they did not report the compressive strength data.

The cross-sectional shape of carbon fibres may have an effect on the fibre compressive strength although such investigations were not carried out in the present study. The works of Niederstadt and Diwan were reviewed recently by Edie [115]. Niederstadt, combining theoretical and experimental studies, claimed that non-circular PAN-based fibres should have a higher compressive strength than circular fibres. Diwan investigated the effect of non-circular pitch-based carbon fibres on the performance of polymeric composites; he found that the compressive strengths of the composites reinforced with the more highly non-circular hexalobal fibres were 16% higher than those reinforced with the trilobal fibres. Therefore, the use of non-circular shapes may results in improved compressive strengths for both PAN- and pitch-based carbon fibres.

Generally, as already observed, no matter how the layer planes are organized across the fibre cross section they are usually well aligned parallel to the fibre axis to maintain a relatively high Young's modulus. However, longitudinal folding of layer planes may also give fibres more resistance to shear between basal planes as in the case of transverse folding, nevertheless this will be at the expense of a lower Young's modulus. Indeed, for the low modulus fibre E35C which shows a very high compressive strength, such longitudinal folding may occur (see Figure 3-5a).

6. 2. Microstructure and compressive strength

The microstructure of carbon fibres is usually studied by X-ray diffraction and/or transmission electron microscopy. X-ray diffraction gives an average value of a structure parameter, such as interlayer spacing, crystallite size and orientation. Unfortunately, the distributions of the parameter value, which are very important for understanding the fibre mechanical properties, are not easily obtained. On the other hand, TEM electron micrographs directly display the microstructure of the fibres and hence the distributions of the structural parameters but in a qualitative manner. In the present work, therefore, image analysis techniques have been used, for the first time, on TEM micrographs in an attempt to quantify the development of microstructure in carbon fibres. Indeed, as reported in Chapter 4, some very interesting results have been achieved. Three main structural parameters have been evaluated, namely, (1) layer stacking sizes including the value L_c from X-ray diffraction and L_c* from dark-field images, (2) crystallite orientations including preferred orientation (IB_x and IB_d values from X-ray diffraction and electron diffraction patterns respectively) and local misorientation (IB_l as well as ϕ values from lattice-fringe images), and (3) lattice imperfections involving the tortuosity of layer planes and the variation of the interlayer spacing. For comparison purposes, all structural parameters obtained for each fibre, together with their corresponding compressive strengths, are listed in table 6-1. In the following section, the various structural parameters are discussed in terms of their influence on compressive strength.

6. 2. 1. Layer stacking sizes and compressive strength

The measurement of layer stacking size L_c from X-ray diffraction was described

Table 6-1. Various structural parameters for Du Pont MP-based carbon fibres

Fibres	Compressive Strength σ_c (*GPa*)	Layer Stacking Size (*nm*)		Crystallite Imperfection I_c (%)	Preferred Orientation (*deg.*)		Local misorientation (*deg.*)		Interlayer Spacing (*nm*)		Lattice Tortuosity S (%)	Stacking Imperfection (%)	
		L_c	L_c^*		IB_x	IB_d	IB_t	ϕ	d_{002}	d_{002}^*		D_c	D_c^*
E35	0.82	3.7	32.2	89	28.4	22.9	22.5	9.1	0.3421	0.353	12.8	25.4	64.3
E55	0.78	8.5	30.8	72	20.1	21.6	21.4	10.0	0.3418	0.344	10.8	24.3	32.1
E75	0.67	12.0	32.9	64	16.3	18.9	13.4	6.5	0.3417	0.342	7.2	23.9	25.0
E105	0.61	16.8	29.6	43	13.8	12.2	10.6	5.7	0.3399	0.343	6.3	17.5	28.6
E120	0.57	19.2	29.6	35	11.4	10.8	8.0	5.7	0.3396	0.337	2.2	16.4	7.1
E130	0.63	23.8	40.0	41	12.5	10.6	5.3	4.0	0.3376	0.338	1.8	9.3	10.7
E35C	0.77~1.03	3.2	31.4	90	28.1	–	27.5	13.6	0.3455	0.363	14.8	37.5	100.0
C700	—	27.9	27.7	0	9.4	9.4	2.7	3.2	0.3360	0.336	2.1	3.6	3.6

previously in Chapter 3. The results indicated that for a series of MP-based fibres the apparent layer stacking size L_c increases gradually with increasing graphitization. Kumar [66] reported stacking sizes L_c of 3.2, 10.3 and 13.8 *nm* for fibres E35, E75 and E105 respectively, which are comparable with the corresponding values found in the present study (3.7, 12.0, 16.8 *nm*). The discrepancy is not particularly significant and probably due to the different instrumental conditions.

The compressive strength vs layer stacking size L_c for Du Pont fibres is shown in Figure 6-2. For comparison purposes a plot for Thornel fibres is also drawn based on the data from Park [72]. Clearly, for both types of pitch-based fibres there is a tendency for the compressive strength to initially decrease with increasing layer stacking size L_c and then level out (18 *nm* for Du Pont fibres and 25 *nm* for Thornel fibres). This may indicate that large crystallites are more susceptible to shearing. Park *et al.* [72] considered that as the stacking size increases the compressive deformation changes from plastic (i.e. failure by a buckling mechanism) to elastic (i.e. failure by classical shear). Further they suggested that the stacking size should be limited below about 5 *nm* in order to achieve the highest compressive strength.

On the other hand, however, it is interesting to find that at the same value of L_c the compressive stress of Du Pont fibres is higher than that of Thornel fibres as seen in Figure 6-2. Moreover, the discrepancy between them becomes more pronounced with increasing stacking size L_c. This may indicate that the fibre compressive strength depends not only on the stacking size but also on other structural factors, for example layer plane type (see section 6.1).

As indicated in Chapter 4, the stacking size values L_c obtained from X-ray diffraction

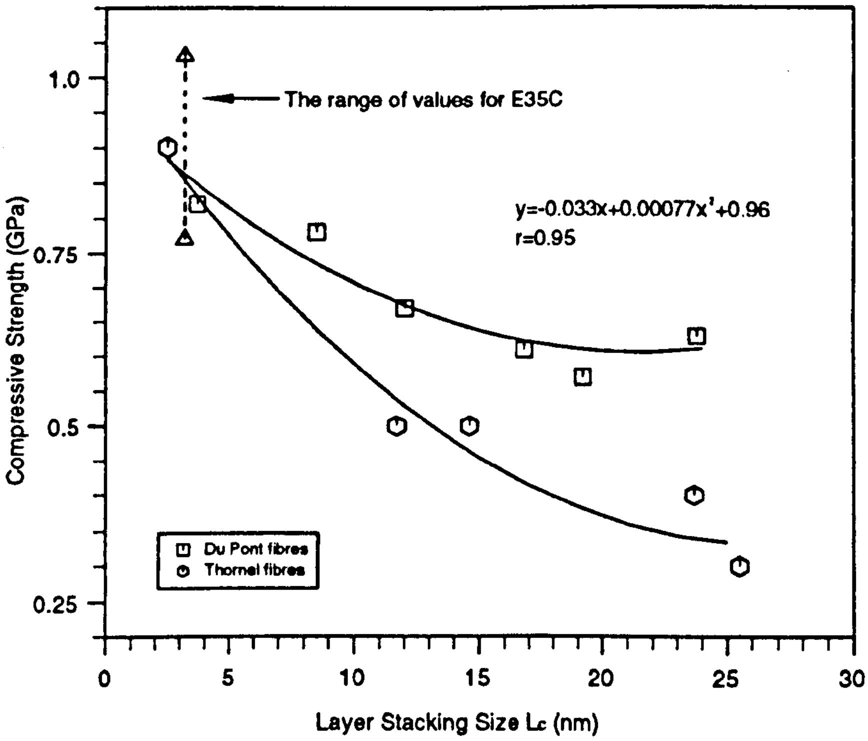

Figure 6-2. Compressive strength as a function of layer stacking size for Du Pont and Thornel MP-based carbon fibres.

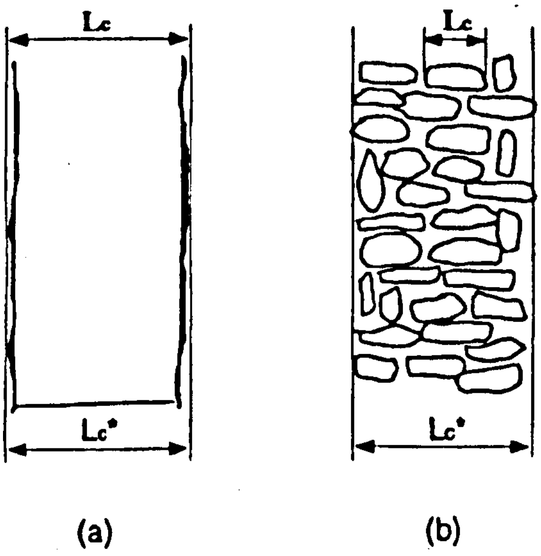

Figure 6-3. Schematic diagram showing the discrepancy between stacking size L_c and L_c* in the two types of crystalline columns: (a) nearly perfect, and (b) imperfect

studies arise from single well-developed crystalline regions, whereas the L_c* values obtained from dark-field images are associated with aggregates of individual crystalline regions as shown in Figure 6-3. Thus the discrepancy between L_c and L_c* is presumably due to localized imperfections within the crystalline column. In other words, besides single perfect crystallites there still exist some small disordered regions within these crystalline columns. Kumar [66] determined the sheet thickness from high resolution scanning electron microscopy (HRSEM) micrographs of MP-based fibres and compared the values with layer stacking size L_c measured from X-ray diffraction. Surprisingly he found that in the case of higher modulus fibre (P100) there is a excellent agreement between the sheet thickness from HRSEM (25 *nm*) and L_c from X-ray (22.7 *nm*), whereas in the case of lower modulus fibre (P25) the sheet thickness from HRSEM (15 *nm*) is significantly larger than L_c from X-ray (2.6 *nm*), which, he also considered, is probably due to the lack of continuity within the sheets. Presumably, the graphitic sheets appear as crystallite columns in the dark-field images. Thus his observations support the findings obtained in the present work.

The relative degree of imperfection in crystalline columns can be estimated from the discrepancy between L_c and L_c* using the relation:

$$I_c = \frac{L_c^* - L_c}{L_c^*} \times 100\%$$

The I_c values for Du Pont MP-based fibres are listed in table 6-1. As can be seen in Figure 6-4, the fibre compressive strength tends to increase linearly with increasing crystallite imperfection factor *(I_c)*. This may imply that, even in the case of large stacking size L_c, the compressive strength can be improved by the incorporation of imperfections distributed within the crystalline column.

It was considered that the distribution of crystallite size may also have an influence on the compressive performance of various carbon fibres and a narrower distribution may correspond with higher compressive strength [72]. However, from the present work, it is difficult to find any firm relationship between compressive strength and the distributions of crystallite size as in all cases there is a similar wide distribution of sizes as shown in Figure 4-2.

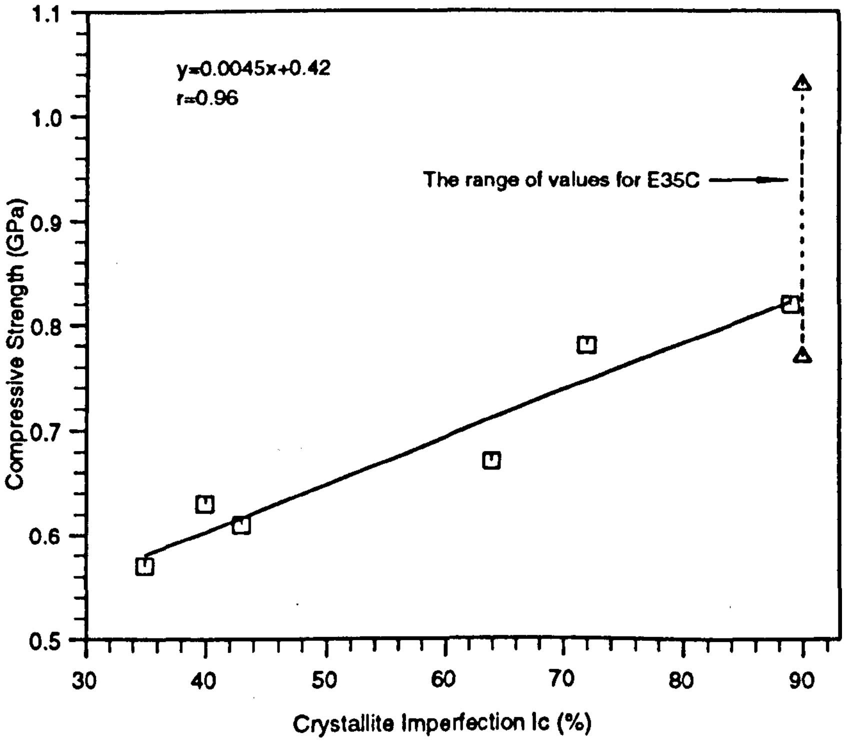

Figure 6-4. Compressive strength as a function of the crystallite imperfection factor for Du Pont MP-based carbon fibres

6. 2. 2. Crystallite orientation and compressive strength

As shown in Figure 6-5, generally the fibre compressive strength increases gradually with decreasing preferred orientation (increase of integral breadth value) and then tends to level out when the IB_x value is larger than about 25 degrees.

As indicated previously in Figure 4-5, the better the orientation, the higher is the fibre Young's modulus. In the case of perfect orientation parallel to fibre axis, the Young's modulus reaches a maximum value of 1060 GPa while the shear modulus drops down to the lowest value of 5 GPa [68]. The large difference between values of the Young's modulus and shear modulus reflects the anisotropy of the structure. Northolt *et al.* [68] established the following relationship:

$$\frac{1}{E} = \frac{1}{e_1} + \frac{\langle cos^2\phi\rangle}{g}$$

Where E is the fibre Young's modulus, g is the shear modulus, $<cos^2\phi>$ is the misorientation and e_1 is the theoretical Young's modulus (=1060 GPa). In the case of perfect orientation parallel to the fibre axis $<\cos^2\phi>=0$. This equation can be applied to estimate the shear modulus for an individual fibre specimen. They found that the shear modulus g is about 5 GPa for perfect graphite, 12 GPa for pitch-based fibres and 15~35 GPa for PAN-based fibres. Furthermore, a strong correlation between the compressive strength σ_c and the shear modulus g was obtained, where $\sigma_c=-0.05+0.10g$. Therefore, the high degree of orientation necessary for promoting Young's modulus tends to give a low shear modulus and hence a low compressive strength.

It is well known that the modulus of the material depends directly on the bonding strength between the atoms. High values of Young's modulus reflect strong sp^2 aniso-

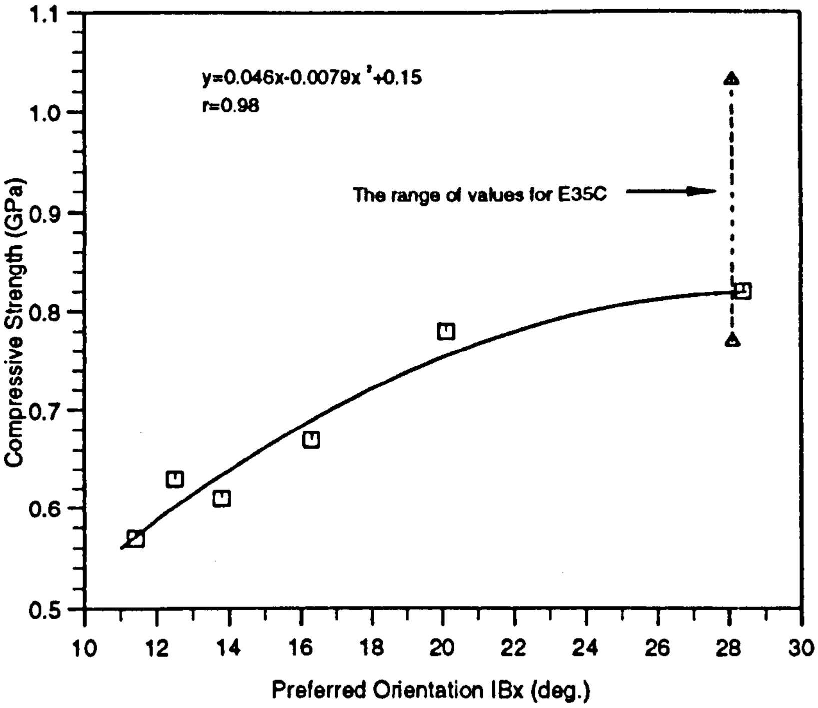

Figure 6-5. Compressive strength as a function of preferred orientation for Du Pont MP-based carbon fibres

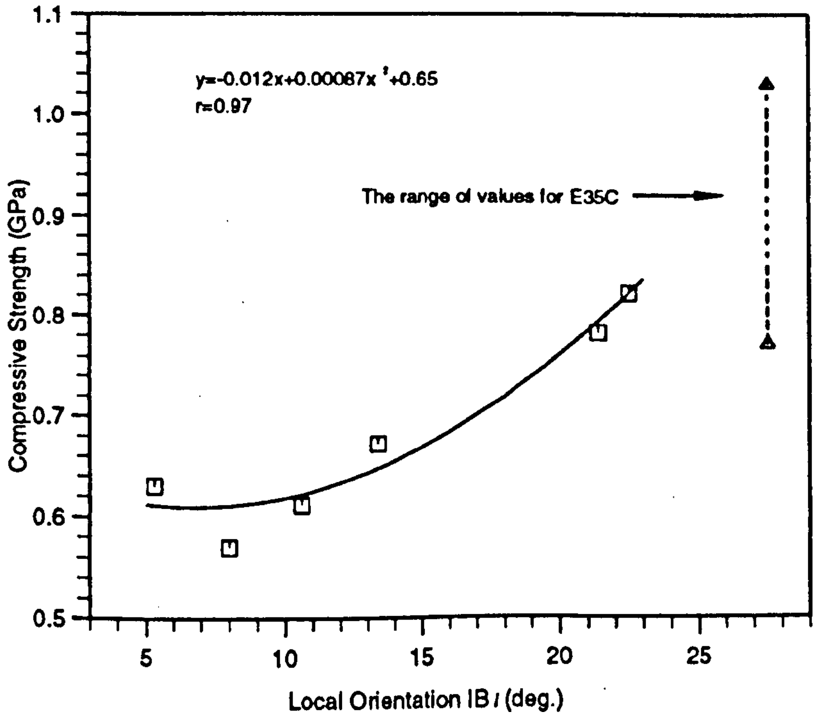

Figure 6-6. Compressive strength as a function of local orientation for Du Pont MP-based carbon fibres

tropic bonds between the carbon atoms within the layer planes, whereas low values of shear modulus reflect weak *Van der Waal* bonds between layer planes. In addition, it is believed that diamond-type sp^3 bonding will cause an increase in shear modulus since this tetrahedral hybridization is presumably located at the edge of the layer planes and hence produces some cross linking between layer planes promoting a high shear modulus.

It seems very likely that the existence of crossing linking between layer planes might restrict the development of layer orientation. In other words, the amount of cross linking between layer planes may be reflected macroscopically by the degree of preferred orientation of layer planes. Indeed, both the number of cross links and the degree of misorientation will be reduced considerably as graphitization proceeds.

It should be noted that the preferred orientation is only one of the factors affecting the compressive strength. The fibre compressive strength as a function of local orientation IB_l is shown in Figure 6-6. It is clear that compressive strength generally increases with increasing local misorientation. It is considered that a polynomial regression curve give a more reasonable fit than a linear regression curve.

By comparing Figure 6-6 with Figure 6-5, it is interesting to find that although compressive strengths increase with increasing both overall and local misorientations, the regression graphs in the two cases are significantly different. The graph of the compressive stress vs preferred orientation appears to have a decreasing slope while the graph of the compressive stress vs local orientation appears to have an increasing slope.

Indeed, the local orientation is very different from the overall preferred orientation which refers to the average alignment of all crystallites relative to the fibre axis. Local orientation, on the other hand, represents the short range alignment of layer planes relative to an individual crystallite axis. Clearly, meandering layer planes tend to have the higher values of local misorientation than straight layer planes. Therefore, the local misorientation is, in fact, a reflection of layer plane imperfection, which will be discussed in the following section.

6. 2. 3. Lattice imperfections and compressive strength

The presence of lattice imperfections in carbon fibre structure can be directly and easily observed in lattice-fringe images. Three main types of lattice imperfections can be identified: (1) the meandering of individual fringes, (2) the variation of fringe spacings, and (3) the termination of a fringe within continuous adjacent fringes (edge

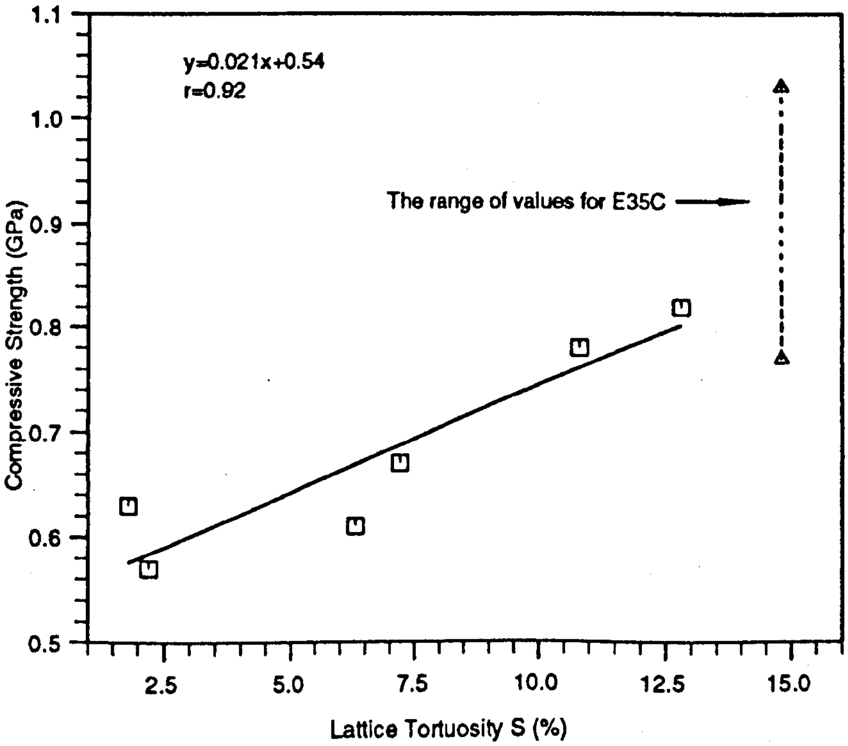

Figure 6-7. Compressive strength as a function of lattice tortuosity for Du Pont MP-based carbon fibres.

dislocation). It would be expected that such imperfections may considerably influence the mechanical behaviour of carbon fibres.

As reported in Chapter 4, lattice fringe meandering was quantified and expressed by a parameter, lattice tortuosity, which is zero in the case of perfect graphite layer planes and increases gradually with increasing degree of meander. As shown in table 6-1, the lattice tortuosity values found in the series of Du Pont pitch-based fibres decrease from about 15% to 2% with increasing graphitization, and quantitatively indicates the gradual removal of in-plane structural defects by annealing.

The fibre compressive strength as a function of the lattice tortuosity is plotted in Figure 6-7 for the MP-based carbon fibres studied. It is found the the compressive failure stress appears to increase linearly with increasing lattice tortuosity. It is tempting to suggest that the bending of the layer planes in carbon fibres inhibits shear between the basal planes and hence promotes the fibre compressive strength. The reason for this may be explained as follows. Suppose a uniaxial compressional force is applied to a stack of layer planes. If the layer planes meander, then the stress will be distributed in different directions due to the complicated configuration. However, if the layer planes are perfectly straight, the stress will be applied along the layer plane direction only and hence facilitate shear deformation.

It is well known that stacking faults between layer planes cause increased layer separation in carbon fibres [22]. With increasing degrees of stacking imperfections, interlayer spacings increase from a value of 0.3354 *nm* for perfect graphite to values of more than 0.344 *nm* for turbostratic carbon. Thus the stacking imperfection can be quantified directly by measuring the average interlayer spacing or by calculating the relative degree of intra-crystallite imperfection D_c as suggested by Park *et al.*[109],

$$Dc = \frac{d_{obs.} - d_{gra.}}{d_{turb.} - d_{gra.}} \times 100\%$$

where $d_{turb.}$, $d_{gra.}$, and $d_{obs.}$, are the interlayer spacings in a turbostratic carbon, perfect graphite, and the actual carbon fibre respectively. In the present work, the interlayer spacings of each fibre were measured from both X-ray diffraction and lattice-fringe images, therefore two ranges of stacking imperfection factors D_c and D_c^* can be obtained corresponding respectively with the interlayer spacing from X-ray diffraction (d_{002}) and lattice-fringe images (d_{002}^*). Values $d_{gra.}$=0.335 *nm* and d_{turb}=0.344 *nm* have been suggested [108]. However, in most cases, the $d_{turb.}$ value needs to be adjusted in order to maintain D_c values less than 100%. For example, Park *et al.* [109] used $d_{turb.}$=0.350 *nm* in their calculation of D_c. In this work, $d_{turb.}$=0.363 *nm* (interlayer spacing value of fibre E35C) and $d_{gra.}$=0.335 *nm* were used, which assumes that the stacking imperfection factor measured from lattice-fringe images for fibre E35C is 100%. As shown in table 6-1, degrees of stacking imperfections for other fibres are relative to the spacing difference between E35C and perfect graphite.

Fibre compressive strengths as a function of the stacking imperfection factors D_c and D_c^* for Du Pont fibres are shown in Figure 6-8. It can be seen, from both ranges of data, that the compressive strength tends to increase with increasing relative degrees of stacking imperfections (larger interlayer spacing) although linear correlation coefficients are not very high. In contrast to these findings, Park [72], working on a series of Thornel MP-based carbon fibres, observed a high linear correlation coefficient (r=0.97) between compressive strength and stacking imperfection factor. This may indicate that other structural factors are probably involved, for example, the macrostructure of fibres.

The general increase of compressive strength with increasing stacking imperfection can be possibly explained by a mechanism of energy absorption arising from increasing localized deformation. In the case of a well-stacked crystallite structure, localized deformation is difficult due to the regularity and "tightness" of the ordered structure, and compressive forces would easily initiate shear between basal planes leading to a low compressive strength.

It is very interesting to note that an approximate extrapolation of the regression plot obtained from the fringe data to the value of D_c=0% (interlayer spacing of 0.335 *nm*) gives a compressive strength value of 0.56 *GPa*. According to the relation between compressive strength σ_c and shear modulus g, $\sigma_c=-0.05+0.10g$, suggested by Northolt *et al.* [68], the corresponding shear modulus is 6.1 *GPa*, which is slightly higher than the value of 5 *GPa* normally accepted for perfect graphite. If the same procedure of extrapolation is applied to the compressive strength vs tortuosity (Figure 6-7) then the compressive strength of perfect graphite is approximately 0.54 *GPa*, which would give a value of 5.9 *GPa* for the shear modulus.

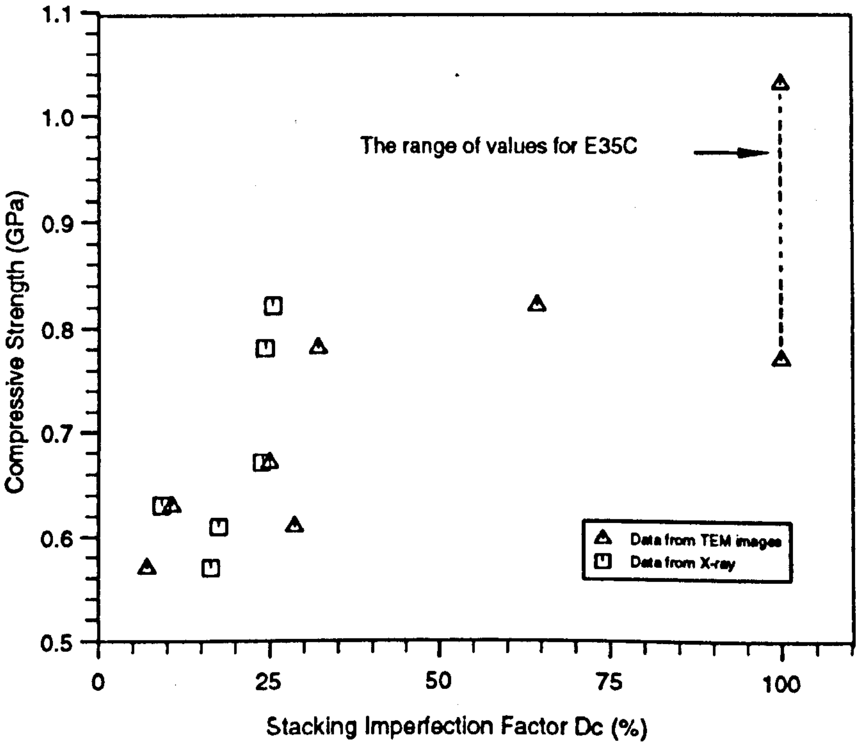

Figure 6-8. Compressive strength as a function of the stacking imperfection factor for Du Pont MP-based carbon fibres.

6. 3. Conclusions

Summarising the general discussion, the following main conclusions can be drawn concerning the compressive behaviour of MP-based carbon fibre and its dependence on macro- and microstructure:

1. It appears that under the recoil compressive loading Du Pont MP-based carbon fibres fail due to a combination of tensile and compressive forces arising from bending.

2. SEM studies indicate that the lateral macrostructure of all Du Pont fibres is of pseudo-radial layers folded tangentially and arranged in domains which become more perfect and singular with increasing fibre Young's modulus. It would appear, in comparison with Thornel pitch-based fibres, that fibres with such a folded layer structure tend to have a higher compressive strength than fibres with a flat layer structure. Moreover, it appears that the presence of domains, which may be associated with disclinations, leads to a relatively high compressive strength.

3. TEM and X-ray diffraction studies reveal that the microstructure of Du Pont fibres ranges from turbostratic to three-dimensional graphitic order with different degrees of imperfection. Significantly, it is shown that by using image analysis techniques various structural parameters can be determined quantitatively from TEM micrographs (dark-field and lattice-fringe images). Three main types of structural parameters were obtained in the present work, namely, (1) layer stacking sizes, (2) crystallite orientations, and (3) lattice imperfections. Such parameters appear to be the main microstructural factors influencing the compressive behaviour of carbon fibres.

4. Compressive strength tends to decrease with increasing layer stacking size L_c. On the other hand, however, it was found that even in the case of large stacking size, the

compressive strength can be improved by the incorporation of imperfections distributed within the crystalline columns.

5. Lattice imperfections influence the compressive strength in several ways. In-plane imperfections, which may be expressed by lattice tortuosity, tend to promote fibre compressive strength by distributing the stress in different directions following the meandering of layer planes. Stacking imperfection, such as variability in interlayer spacings, improves the compressive strength by allowing a higher localized deformation.

6. The high degree of preferred orientation necessary for achieving high Young's modulus tends to cause a decrease in shear modulus between basal planes and hence imparts a low compressive strength.

6. 4. Future work

Current research indicates that the compressive strength of mesophase pitch-based carbon fibres can be significantly improved by the incorporation of lattice imperfections, particularly the localized imperfections. Future research should concentrate on the development of MP-based fibres with new structures which can possibly incorporate large local imperfections and so increase the compressive strength without significantly reducing the fibre tensile modulus.

With regard to the image analysis technique introduced in this work, it is considered that continued effort is needed to expand its application to other carbon materials. In addition, this contemporary technique will be particularly valuable in the analysis of heterogenous materials, such as skin-core structures which exist in some carbon fibres.

References

1. R. Bacon : In *Chemistry and Physics of Carbon*, Vol. **9**, P.L. Walker, Jr., and P.A. Thrower, eds., Marcel Dekker, Inc., p1 (1973)
2. A. Shindo, *Osaka Kogyo Gijitsu Shikenjo Koho* **12**, 110 (1961)
3. S. Otani, *Carbon* **3**, 31 (1965)
4. W.N. Mair, and E.H. Mansfield, *'William Watt 1912-1985', Biographical Memoirs of Fellows of the Royal Society*, **33**, 643 (1987)
5. W. Watt, L.N. Phillips and W. Johnson, *Engineer*, **222**, 815 (1966)
6. L.S. Singer, *Carbon* **16**, 409 (1970)
7. H. Fujimaki, F. Kodama, K. Okuda, Y. Sakaguchi, and S. Otani, *Tanso* No.**80**, 3 (1975)
8. G.P. Daumit, *Carbon* **27**, 759 (1989)
9. W. Watt : In *Handbook of Composites*, Vol.**1**--*Strong Fibres*, W. Watt and B.V. Perov, eds., Elsevier Science Publishers B.V., North Holland, p327 (1985)
10. D.J. Thorne : In *Handbook of Composites*, Vol.**1**--*Strong Fibres*, W. Watt and B.V. Perov, eds., Elsevier Science Publishers B.V., North Holland, p475 (1985)
11. G.P. Daumit, and Yoon S. Ko : In *High Tech--The way into the Nineties*, Klaus Brunsch, Hans-dieter Göldeu, and Claus-Michael Herkert, eds., Elsevier Science Publishers Co., Inc., p 201 (1986)
12. S. Otani, *Carbon* **3**, 213 (1965)
13. B. Rand : In *Handbook of Composites*, Vol.**1**--*Strong Fibres*, W. Watt and B.V. Perov, eds., Elsevier Science Publishers B.V., North Holland, p495 (1985)
14. D.D. Edie : In *Carbon Fibres, Filaments and Composites*, J.Figueiredo, C.A. Bernardo, R.T.K. Baker, and K.J. Hüttenger, eds., Kluwer Academic Publ., p647 (1990)
15. L.S. Singer, *U.S. Patent*, 4,005,183 (1977)
16. R.J. Diefendorf, and D.M. Riggs, *U.S. Patent*, 4,208,267 (1980)

17. J.B. Barr, S. Chwastiak, R.Didchenko, I.C. Lewis, R.T. Lewis and L.S. Singer, *Appl. Polymer Symp.* **29**, 161 (1976)

18. T. Hamada, Nishida, Y. Sajiki, M. Matsumdo, and M. Endo, *J. Mater. Res.* **2**, 850 (1987)

19. A.A. Bright, L.S. Singer, *Carbon* **17**, 59 (1979)

20. J.L. White and M. Buechler : In *Petroleum-Derived Carbons*, J.D. Bacha, J.W. Newman and J.L. White, eds., *American Chemical Society Symposium Series* **303**, p62 (1986)

21. B.T. Kelly, *Physics of Graphite*, Applied Science, London (1981)

22. M.S. Dresselhaus, G. Dresselhaus, K. Sugihara, I.L. Spain, H.A. Goldberg, *Graphite Fibres and Filaments*, Springer-Verlag Berlin Heidelberg (1988)

23. J.C. Bokros : In *Chemistry and Physics of Carbon*, Vol. 5, P.L. Walker, Jr., and P.A. Thrower, eds., Marcel Dekker, Inc., p1 (1969)

24. A. Fourdeux, R. Perret, and W. Ruland : In *Carbon Fibres--Their Composites and Applications*, The Plastics Institute, London, p57 (1971)

25. A. Fourdeux, R. Perret and W. Ruland, *J. Appl. Cryst.* **1**, 252 (1968)

26. T. Perret, and W. Ruland : In *Summary of papers of 9th Biennial Conf. on Carbon*, Boston, Mass., p158 (1969)

27. A. Fourdeux, R. Perret and W. Ruland, *C. R. Acad. Sci. Paris, Series* **C271**, 1495 (1970)

28. A. Fourdeux, R. Perret and W. Ruland, *C. R. Acad. Sci. Paris, Series* C269,1597 (1969)

29. D.J. Johnson and C.N. Tyson, *Brit.J. Appl. Phys.* (*J. Phys. D*), **D2**, 787 (1969)

30. D. Crawford, *Ph.D. thesis*, University of Leeds, England (1972)

31. D.J. Johnson, D. Crawford, and C. Oates, *10th Biennial Carbon Conference*, Bethlehem, Penn., p29 (1971)

32. S.C. Bennett and D.J. Johnson, *Carbon* **17**, 25 (1979)

33. M. Guigon, A. Oberlin and G. Desarmot, *Fibre Science and Technology*, **20**, 55 (1984)

34. M. Guigon, A. Oberlin and G. Desarmot, *Fibre Science and Technology*, **20**, 177 (1984)

35. A. Oberlin : In *Chemistry and Physics of Carbon*, Vol. **22**, P.L. Walker, Jr., and P.A. Thrower, eds., Marcel Dekker, Inc., p1 (1989)

36. M. Endo, *J. Mater. Sci.*, **23**, 598 (1988)

37. M. Guigon and A. Oberlin, *Compos. Sci. Tech.* **25**, 231 (1986)

38. E.J. Roche, J.G. Lavin, and R.G. Parrish, *Carbon* **26**, 911 (1988)

39. E.J. Roche, J.G. Lavin, and R.G. Parrish, *Carbon* **26**, 389 (1988)

40. E.J. Roche, *J. Mater. Sci.* **25**, 2149-2158 (1990)

41. X. Bourrat, E.J. Roche, J.G. Lavin, *Carbon* **28**, 236 (1990)

42. X. Bourrat, E.J. Roche, J.G. Lavin, *Carbon* **28**, 435 (1990)

43. J.D. Fitz Gerald, G.M. Pennock, and G.H. Taylor, *Carbon* **29** 139 (1991)

44. G.M. Pennock, G.H. Taylor, and J.D. Fitz Gerald, *Carbon* **31**, 591 (1993)

45. L.S. Singer, *Carbon* **16**, 408 (1978)

46. T. Matsumoto, *Pure & Appl. Chem.* **57**, 1553 (1985)

47. D.D. Edie, N.K. Fox and B.C. Baruet, *Carbon* **24**, 481 (1986)

48. I. Mochida, Sh. Yoon, Y. Korai, *J. Mater. Sci.*, **28**, 2331 (1993)

49. I. Mochida, S.M. Zeng, Y. Korai, T. Hino, and H. Toshima, *J. Mater. Sci.*, **27**, 1960 (1992)

50. R. Bacon, *J. Appl. Phys.* **31**, 283 (1960)

51. J.W. Johnson, J.K. Marjoram, and P.G. Rose, *Nature* **221**, 357 (1969)

52. S. Allen, G.A. Cooper, D.J. Johnson, and R.M. Mayer : In *Proc. Third London Int. Conf. Carbon and Graphite*, Soc. of Chemical Industry, London. p456 (1970)

53. B.J. Wicks, *J. Nucl. Mater.* 56, 287 (1975)

54. D.J. Johnson : In *Carbon Fibres, Filaments and Composites*, J.Figueiredo, C.A. Bernardo, R.T.K. Baker, and K.J. Hüttenger, eds., Kluwer Academic Publ., p118 (1990)

55. D.J. Johnson : In *Chemistry and Physics of Carbon*, Vol. **20**, P.A. Thrower, ed., Marcel Dekker, Inc., p1 (1987)

56. N.H. Macmillan, *J. Mater. Sci.* **7**, 239 (1972)

57. R. Moreton, and W. Watt, *Nature* **247**, 360 (1974)

58. J.B. Jones, J.B. Barr, and R.E. Smith, *J. Mater. Sci.*, **15**, 2455 (1980)

59. S.C. Bennett, D.J. Johnson, and W. Johnson, *J. Mater. Sci.* **18**, 3337 (1983)

60. W.N. Reynolds, J.V. Sharp, *Carbon* **12**, 103 (1974)

61. J.H. Greenwood and P.G. Rose, *J. Mater. Sci.* **9**, 1809 (1974)

62. H.M. Hawthorne and E. Teghtsoonian, *J. Mater. Sci.* **10**, 41 (1975)

63. S. Kumar and T. E. Helminiak : In *Materials Research Society Symposium Proceedings*, Vol. **134**--*The Materials Science and Engineering of Rigid-Rod Polymer*, W.W. Adams, R.K. Eby and D.E. McLemore, eds., MRS. Pittsburgh, Pennsylvania, p363 (1989)

64. J.L.G. DaSilva and D.J. Johnson, *J. Mater. Sci.* **19**, 3201 (1984)

65. M.G. Dobb, D.J. Johnson and C.R. Park, *J. Mater. Sci.* **25**, 829 (1990)

66. S. Kumar, *J. Mater. Sci.* **28**, 423 (1993)

67. G.J. Hayes, D.D. Edie, J.M. Kennedy, *J. Mater. Sci.* **28**, 3247 (1993)

68. M.G. Northolt, L.H. Veldhuizen and H. Jansen, *Carbon* **29**, 1267 (1991)

69. M.G. Northolt, *J. Mater. Sci.* **16**, 2025 (1981)

70. L.C. Sawyer, and D.T. Grubb, '*Polymer Microscopy*', Chapman and Hall (1987)

71. D.B. Williams, A.R. Pelton, R. Gronsky, '*Images of Materials*', Oxford University Press (1991)

72. C.R. Park, *Ph.D. Thesis*, University of Leeds (1990)

73. P.B. Hirsch, '*Electron Microscopy of Thin Crystals*', Butterworths, London (1971)

74. A.W. Agar, R.H. Alderson, D. Chescoe, '*Principles and Practice of Electron Microscope Operation*', North-Holland Publishing Company (1991)

75. '*Jeol 100CX Instruction Manual*', Jeol Ltd., Tokyo, Japan

76. I. Karacan, *Ph.D. Thesis*, University of Leeds (1986)

77. L.E. Alexander, '*X-ray Diffraction Methods in Polymer Science*', John Wiley and Sons, New York (1969)

78. A.M. Hindeleh, D.J. Johnson and P.E. Montague : In *Fibre Diffraction Methods* (*ACS symposium Series 141*), A.D. French, K.H. Gardner, eds., American Chemical Society, Washington, D.C., p149 (1980)

79. '*Quantimet 570 Operators Manual*', Leica Cambridge Ltd. (1991)

80. D.L. Misell, '*Image Analysis, Enhancement and Interpretation*', North-Holland Publishing Company (1978)

81. E.O. Brigham, '*The Fast Fourier Transform and its Application*', Prentice-Hall international, Inc. (1988)

82. '*Image Analysis : Principles and Practice*', Joyce-Loebl (1989)

83. D. Sinclair, *J. Appl. Phys.* **21**, 380 (1950)

84. S.J. Deteresa, S.R. Allen, R.J. Farris and R.S. Porter, *ibid.* **19**, 57 (1984)

85. T. Ohsawa, M. Miwa, M. Kawade and E. Tsushima, *J. Appl. Polym. Sci.* **39**, 1733 (1990)

86. S.R. Allen, *J. Mater. Sci.* **22**, 853 (1987)

87. W. Johnson : In *Handbook of Composites*, Vol.1--*Strong Fibres*, W. Watt and B.V. Perov, eds., Elsevier Science Publishers B.V., North Holland, p389 (1985)

88. W. Ruland : In *Chemistry and Physics of Carbon*, Vol. **4**, P.L. Walker, Jr., and P.A. Thrower, eds., Marcel Dekker, Inc., p1 (1968)

89. A.M. Hindeleh and D.J. Johnson, *Polymer*, **21**, 929 (1980)

90. B.E. Warren, P. Bodenstein, *Acta Crystallogr.* **20**, 602 (1966)

91. W. Ruland, H. Tompa, *Acta Crystallogr.* **A24**, 93 (1968)

92. C.R. Houska, B.E. Warren, *J. Appl. Phys.* **25**, 1503 (1954)

93. D.J. Johnson, *Phil. Trans. R. Soc. London* **A294**, 443 (1980)

94. A. Shindo, *Report* No. **317**, Govt. Ind. Res. Institute, Osaka (1961)

95. T. Stamatoff, H.A. Goldberg, I.L. Kalnin : In *Proceedings of the Symposium on Intercalated Graphite*, Vol. **20**, M.S. Dresselhaus, G. Dresselhaus, J.E. Fischer, M.J. Maran, eds., North-Holland, New York, p51 (1983)

96. H.M. Hawthorne : In *Carbon Fibres--Their Composites and Applications*, The Plastics Institute, London, p81 (1971)

97. W. Watt, and W. Johnson, *Appl. Polymer Symposium* No. **9**, 215 (1969)

98. W. Ruland : In *Conf. on Fibres for Composites* (IPPI), Brighton (1969)

99. R. Perret and W. Ruland, *J. Appl. Cryst.* **3**, 525 (1970)

100. D.J. Johnson : In *Carbon Fibres--Their Composites and Applications*, The Plastics Institute, London, p52 (1971)

101. W. Ruland, *Appl. Polymer Symp.*, **9**, 293 (1969)

102. R. Bacon and M.M. Tang, *Carbon* **2**, 221 (1964)

103. W. Ruland, *J. Appl. Phys.*, **38**, 3585 (1967)

104. R. Bacon and W.A. Schalaman, *Appl. Polymer Symp.*, **9**, 285 (1969)

105. R.J. Price and J.C. Bokros, *J. Appl. Phys.*, **36**, 1897 (1965)

106. H. Gasparoux, A. Pacault and E. Poqaet, *Carbon*, **3**, 65 (1965)

107. F. Tuinstra and J.L. Koenig, *J. Chem. Phys.*, **53**, 1126 (1970)

108. J. Maire and J. Mering, *Proc. First Conference of the Society of Chemical Ind.-- Conf. on Carbon and Graphite*, London, 204 (1958)

109. D.J. Johnson and C.R. Park, *20th Biennial Conference on Carbon*, University of California, Sauta Barbara, p224 (1991)

110. M. Shioya and A. Takaku, *Carbon*, **28**, 165 (1990)

111. J.M. Hutcheon : In *Modern Aspects of Graphite Technology*, L.C.F. Blackman, ed., Academic, New York, p1 (1970)

112. H. Jiang, A.S. Abhiraman and K. Tsui, *Carbon*, **31**, 887 (1993)

113. G.M. Jenkins, In *Chemistry and Physics of Carbon*, Vol. **11**, P.L. Walker, Jr., and P.A. Thrower, eds., Marcel Dekker, Inc., p189 (1973)

114. E. Fitzer, *Carbon* **27**, 621 (1989)

115. D.D. Edie : In *Carbon-Carbon Materials and Composites*, J.D. Buckley and D.D. Edie, eds., NASA Reference Publication **1254**, p41 (1992)

Appendix

A typical program written for the image analyser

```
10 REM ** CALCULATE D-SPACINGS FROM A LATTICE FRINGE IMAGE **
20 REM FILE G2.QBA
30 dim gval(900), dgval(600), t(20), xp(100)
40 dim limits(65), d(100), D0(500), ads(100)
50 qmenu "image_setup"
60 qmenu "calibrate"
70 riasettings "cal_value",cal
80 pausetext 1,"ACQUIRE IN IMAGE 0"
90 qmenu "acquire"
100 pausetext 1, "PERFORM AN AVERAGE TRANSFORM FROM IMAGE
    0 TO 1 GREY PLANE"
110 qmenu "transform"
120 h=1 : sno=0: c=0
130 REM TO PERFORM "K" TIMES LINE SCAN IN GREY IMAGE 1
140 for k=1 to 50
150 pausetext 1, "set blue scan line "
160 pausetext 2, "Record x, y, and w of blue scan line"
170 qmenu "frames"
180 print, "Input values of x, y, and w ?"
190 input x, y, w
200 pausetext 1, "View line scan in image 1"
210 pausetext 2, "                    "
220 qmenu "measure_grey"
230 print, " Are you happy with this trace? Y or N"
240 input d$
250 if d$="N" then 150
260 REM TO FIND THE PEAK POSITION FOR EACH PROFILE OF FRINGE
270 for i=x to (x+w)
280 rpix 1, i, y, gval(i)
290 next i
300 n=0 : pn=0 : ps=0
310 for i=(x+1) to (x+w-1)
```

```
320 dgval(i)=(gval(i+1) -gval(i))
330 dgval(i-1)=(gval(i)-gval(i-1))
340 if (dgval(i) * dgval(i-1)) >0 goto 380
350 pn=pn+1 :ps=ps+i
360 t(pn)=dgval(i-1)
370 goto 440
380 if (ps=0) goto 440
390 if t(1) < 0 goto 430
400 n=n+1
410 xp(n)=ps/pn
420 print, ;"xp("n")=";xp(n)
430 pn=0 : ps=0
440 next i
450 REM TO CALCULATE D-SPACINGS FOR EACH LINE SCAN
460 m=0
470 for i=1 to (n-1)
480 dsp=(xp(i+1)-xp(i))
490 if dsp < 22 goto 530
500 if dsp > 37 goto 530
510 m=m+1
520 d(m)=dsp*cal
525 print, ;"d("m")=";d(m)
530 next i
540 REM TO READ ALL D-SPACINGS INTO ONE ARRAY AND DISPLAY
    IN ONE HISTOGRAM
550 for j=1 to m
560 sno=sno+1
570 D0(sno)=d(j)
580 next j
590 print, "total num.=";sno
600 ads(k+1)=m
610 c=c+1
```

```
620 print, "Do you want to do another line scan? Y or N"
630 input a$
640 if a$="N" then 660
650 next k
660 for i=1 to 65
670 q=(i-1)/140
680 limits(i)=q
690 next i
700 histoclear 0
710 histouser 0 D0(1), sno, limits(1), 64
720 histodisp 0 0 0 0 0 "count" "d-spacing(nm)" 0
730 histofile 0 0 0 0 0 "count" "d-spacing(nm)" b$e35
740 histoprint 0 0 0 0 0  "count" "d-spacing(nm)"
750 REM TO READ D-SPACINGS DATA FOR EACH LINE SCAN AND
    DISPLAY THEM ONE BY ONE
760 st=0 : ed=0 : ads(1)=1
770 for  i=1 to c
780 st=st+ads(i) : ed=ed+ads(i+1)
790 nd=0
800 for j=st to ed
810 nd=nd+1 : d(nd)=D0(j)
820 next j
830 histoclear 1
840 histouser 1 d(1), nd, limits(1), 64
850 histodisp 1 0 0 0 0 "count" "d-spacing(nm)" 0
860 next i
870 end
```